Effect of Radiation on Cardiovascular Function

by

Muath Bishawi

Department of Biomedical Engineering
Duke University

Date:_____

Approved:

_____
George A. Truskey, Advisor

_____
Dawn E. Bowles

_____
Mark W. Dewhirst

_____
Bruce Klitzman

_____
Carmelo A Milano

_____
Allan D. Kirk

Dissertation submitted in partial fulfillment of
the requirements for the degree of Doctor
of Philosophy in the Department of
Biomedical Engineering in the Graduate School
of Duke University

2020

ABSTRACT

Effect of Radiation on Cardiovascular Function

by

Muath Bishawi

Department of Biomedical Engineering
Duke University

Date:_____

Approved:

_____
George A. Truskey, Advisor

_____
Dawn E. Bowles

_____
Mark W. Dewhirst

_____
Bruce Klitzman

_____
Carmelo A Milano

_____
Allan D. Kirk

An abstract of a dissertation submitted in partial fulfillment of the requirements for the degree of Doctor of Philosophy in the Department of Biomedical Engineering in the Graduate School of Duke University

2020

Abstract

There is a scarcity of knowledge regarding the cardiovascular effects of low dose ionizing radiation (IR) such as the one experienced during medical tests, radiation therapy or space travel. This is becoming more of a pressing problem given the enormous increase in radiation exposure by the average American today, and the renewed interest in deep space travel. Multiple epidemiologic studies suggest a higher rate of delayed cardiovascular related morbidity and mortality after low dose acute radiation exposure. These studies are significantly limited by a number of confounders such as cancer comorbidity, poor follow up, and largely estimated radiation doses that might not be accurate. These limitations are also seen in studies on the effect of space radiation on long term cardiovascular mortality and accelerated atherosclerosis. Animal studies have been used to simulate the effect of terrestrial and space radiation scenarios on cardiac function. These studies have led to conflicting conclusions, and had important challenges related to methods of assessment of cardiac injury. Furthermore, available studies to date had limited follow up times, and no study has evaluated the effects of more complex radiation scenarios that are likely to be experienced in space such as Galactic Cosmic Rays (GCRs). Our overall hypothesis is that IR is associated with early damage to healthy cardiomyocytes and vascular cells that eventually leads to long term cardiovascular dysfunction.

In the first part of this work, we hypothesize that IR is associated with a delayed cardiovascular derangement phenotype late after initial exposure. To test this hypothesis, we use a mouse animal model to study the effect of different radiation scenarios on cardiovascular function. Animals were exposed to one of the following (a) Gamma Rays (50-200 cGy), (b) ^{56}Fe (15-50 cGy), (c) ^{16}O (15-50cGy) heavy ions, and (d) 150cGy Galactic Cosmic Rays all using the particle accelerator at Brookhaven National Labs (BNL). The mice were then followed up for 9-12 months, and underwent cardiac MRI, pressure volume loop assessments, transthoracic echocardiograms and other histological evaluations. These studies revealed that GCR exposed animals had a clinically meaningful decline in their cardiac function, with a significant change in their arterial elastance. These findings were further confirmed on histology with their aortas demonstrating elastic fiber destruction and disorganization.

These animal studies however could not fully differentiate between a primary cardiac injury or a secondary cardiac response to a primary vascular injury to the aorta. Our hypothesis for the second part of this work, was that IR is associated with a unique and differentiated injury to cardiomyocytes that contributes to the previously seen cardiovascular phenotype. We therefore conducted additional experiments on isolated rat ventricular cardiomyocyte in collaboration with the Bursac lab. These studies used both 2D cultured cells, as well as a novel cardiac patch system exposed to gamma rays and X-rays (0.1-2 Gy). These cells underwent proteomics analysis, as well as a number of

different biological and functional assays. While the acute functional effect of these radiation doses on cardiomyocytes was small, these irradiated cells produced a significant amount of reactive oxygen species and exhibited a large effect of radiation on mitochondrial related proteins, including elements of oxidative phosphorylation. We also noted a number of different pathways involved at different doses of radiation. This was an important finding, given that despite no changes in early cell death, the effect of these important proteomics changes on long term cardiac function maybe important.

Finally, for the last part of this dissertation, our hypothesis was that IR uniquely affects endothelial cells (ECs) and smooth muscle cells (SMCs) by inducing early senescence that is primarily due to over production of mitochondrial specific reactive oxygen species. To test this hypothesis, we use primary coronary artery endothelial cells, primary human aortic endothelial cells and primary coronary artery smooth muscle cells. These relevant cell types were then examined for their response to a single dose of radiation exposure. Given the previous findings of important mitochondria involvement even at low radiation doses, we used a novel mitochondrial specific ROS scavenger, that blocks the release of mitochondrial reactive oxygen species (mROS), mito-TEMPO. Cells treated with mito-TEMPO had a significant decrease in observed cellular senescence an important hallmark of cellular dysfunction. Blockage of mROS might have a potential therapeutic role in the prolonged cardiovascular effects of radiation exposure.

In summary, data generated in this dissertation supports the overall hypothesis that IR is associated with long term cardiovascular dysfunction that can be explained by early injury to cardiac, endothelial and smooth muscle cells. Galactic Cosmic Rays appear to significantly effect long term cardiovascular function, which has important implications on deep space travel. This effect is likely multifactorial, involving a number of organs, including the aorta. Cardiomyocytes, despite being resilient to death from radiation as compared to other cells types, appear to undergo a number of proteomics alterations after low dose radiation exposure, with significant involvement of the mitochondrial machinery. Finally, human vascular ECs and SMCs are highly sensitive to radiation exposure, and strategies that target mitochondrial specific ROS production might play an important role in mitigating the long-term vascular effects after radiation exposure.

Dedication

To my grandmother Khadejah, for teaching me everything important I needed to know about life using a lemon tree.

Mom and dad, Maysoun and Mousa. Your interminable courage to move a family with 5 young kids to the United States, gave us all the opportunity at a better, more fulfilling life. You somehow managed to always have food on the table and a roof over our head. For that we are forever grateful.

To my siblings, Maram, Mohammad, Mira and Mumen- for all your love and support throughout my endless training.

To all my teachers and mentors throughout the years. For finding something worth supporting in me, I thank you. You have helped my dreams come true.

Finally, to all my patients- past, present and future. Perhaps the greatest privilege of all, is getting to help someone when they need it most. You have been and will always be my motivation as a physician scientist.

Contents

List of Tables

List of Figures

Acknowledgements

First, I would like to acknowledge and thank my thesis advisor, Dr Truskey. His incredible mentorship has been the most important part of my learning during my PhD. He is always supportive of my many interests, and helped nurture my love for science and discovery. I have learned so much from him about how to run a successful lab.

I would also like to sincerely thank Dr Bowles. She has introduced me to the field of space radiation, and everything NASA. Her style of giving me ownership over my projects has allowed me to grow tremendously as a scientist.

I would also like to thank my PhD Committee, they have always been supportive, provided really valuable feedback and helped advise me and teach me. They are all very busy, but always managed to make time for me.

I would like to thank my lab mates, who have made my research time really enjoyable. I have learned a lot from you, and enjoyed our many discussions. From the Truskey lab (Xu, Nadia, Cristina, Leigh, Ellen, Megan, Qiao, Anandita, Cathrine, Ellery, Diego, Dillon, and Alex). From the Bowles Lab (Zach, Franklin, Mike, Ryan, Dillon, and Chunbo). I want to specifically thank Diego for all his help with image processing.

For the mouse radiation studies, I want to specifically acknowledge many of the individuals that made these complex studies possible, including NASA radiation science laboratories Peter Guida, Adam Rusek, and Debbie Snyder. We would also like to acknowledge Duke DLAR and all the individuals that help to care for our animals over

the long study period. The animals studies would not have been possible without all the work done by members of the Duke CVRC, including Dennis Abraham, Lan Mao, and Howard Rockman. Carolyn Glass for all the help with the histological evaluation of the tissue, and Stephanie Blocker and Al Johnson for help with the cardiac MRIs.

For the proteomics studies, we would like to thank Bryan Feger, Abbi Helfer, and Nenad Bursac. We would also like to acknowledge the Duke Proteomics Core, including Will Thompson and Arthur Moseley.

Finally, for the pathway analysis work, we would like to thank Robert Lefkowitz, Ahn Seung, and Todd Brennan.

Finally, I want to sincerely thank the Departments of Surgery and Biomedical Engineering, for giving me the time during my residency to pursue this PhD. I am thankful for the incredible support from Dr Kirk, Smith, D'Amico and Milano. I want to also thank the Office of Physician Scientist Development for being the voice for physician scientists at Duke, and nationally, and all the support both financially they provided to my research. Specifically I want to thank Sallie Permar, Scott Palmer, and David Harpole

1. Introduction

1.1 Background and Significance

The National Council on Radiation Protection and measurement highlights a significant increase in the amount of Ionizing Radiation (IR) the average person is exposed to today as compared to only a few decades ago[1]. Most of this increase is secondary to a surge in the use of IR in medical imaging and diagnostic studies[2]. However, despite this increase, there is a scarcity of evidence related to the consequence of this abrupt increase in the context of human health and disease. This is also true when it comes to the renewed interest in space travel, and exposure to the complex space radiation enviroment[3]. Therefore, there is an imperative need to better define the long-term consequences of these different types of radiation exposure.

1.2 Radiation Exposure and Cardiovascular Disease

1.2.1 Radiation common terminology

There is a common radiation terminology that will be used through this work. For virtually all experiments, we will use the absorbed dose in gray (Gy) as the accepted international system of units. One Gy equals 1 J of radiation energy per kilogram. In a few of the sections, where the dose equivalent in sievert (SV) maybe provided if also available, with the same units as Gy, J/kg. The two are related in the 1 sv=WTGy where WT is a weighting factor relating the two quantities. WT depends on the type of radiation and the absorbing properties of the irradiated material organism. The SV will

be mainly used in the discussion of biological effect reported in the literature and background studies.

1.2.2 High vs Low Linear Energy Transfer (LET)

Linear energy transfer (LET) refers to the energy that is deposited from a radiation source as it travels through tissue/cells. LET is proportional to the charge of the particle, and inversely proportional to the kinetic energy[4]. Therefore, heavy, slow traveling particles generally have high LET[5]. Examples of high LET radiation include alpha-particles, protons, and neutrons. Their energy ranges from 3-200 KeV/um. Low LET on the other hand includes electrons, positrons, gamma and x-rays, with energies estimated around 0.2-3 keV/um[5]. Given differences in their charge, size and speed, these different sources of IR have different penetrating properties across different materials and shielding as illustrated in Figure 1.

There are major differences in the biological effect, and cellular sensitivity to high vs low linear energy transfer (LET)[6–9]. Much of this knowledge has been developed in the radiotherapy field, with an increasing level of understanding of the differential cellular and tissue level damage caused by both[10]. For instance, controlling for the dose, high LET radiation is associated with significantly more early cell death, decrease in proliferation and induction of senescence than low LET radiation[10].

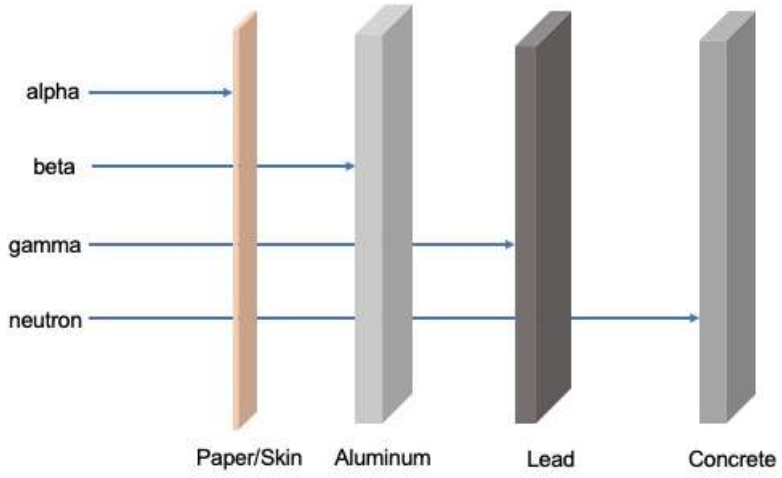

Figure 1: Differences in penetrating power of gamma rays compared to charged particles

This discussion of low vs high LET radiation is of particular interest to space exploration[11]. There are a number of unique radiation scenarios that come into play during space flight, and deep space exploration. These radiation scenarios include exposure to high charge and high energy particles (HZE)[12]. One of the major sources of radiation exposure during deep space exploration are Galactic Cosmic Rays (GCR).

1.2.3 Galactic Cosmic Rays (GCR) radiation

While there are other radiation sources during space travel such as solar energetic particles, and trapped radiation, Galactic Cosmic Rays (GCR) are thought of as the major contributor to space radiation exposure. The make-up of GCR is variable, however, it is generally accepted that it consists of 1% electrons, 80% or more protons, 10-13% helium ions, and the remainder 1-2% being HZEs[13]. GCRs have peak energies 0.1 to 1 GeV/n (gigaelectron volt per nucleus)[11,14]. Importantly, GCR nuclei can penetrate a

substantial thickness of materials (100s of centimeters of water or aluminum)[12]. It is therefore the current thinking that for space missions, it is not possible to provide shielding to fully absorb all GCR exposures in space[15]. This is further complicated by the fact that the LET of each nucleus also changes as it loses energy and its speed decreases inside the tissue being penetrated[16].

1.2.4 The differential biological effect of high vs low LET

High vs low LET radiation have profound differences in their biological effects on cellular organelles, particularly the nucleus and DNA. Clustered DNA lesions are often formed, defined as two or more sites of DNA damage within 20 base paris[17]. Figure 2 is an illustration of a low vs high LET track through cells and the subsequent ionization events and clustered damage sites[18].

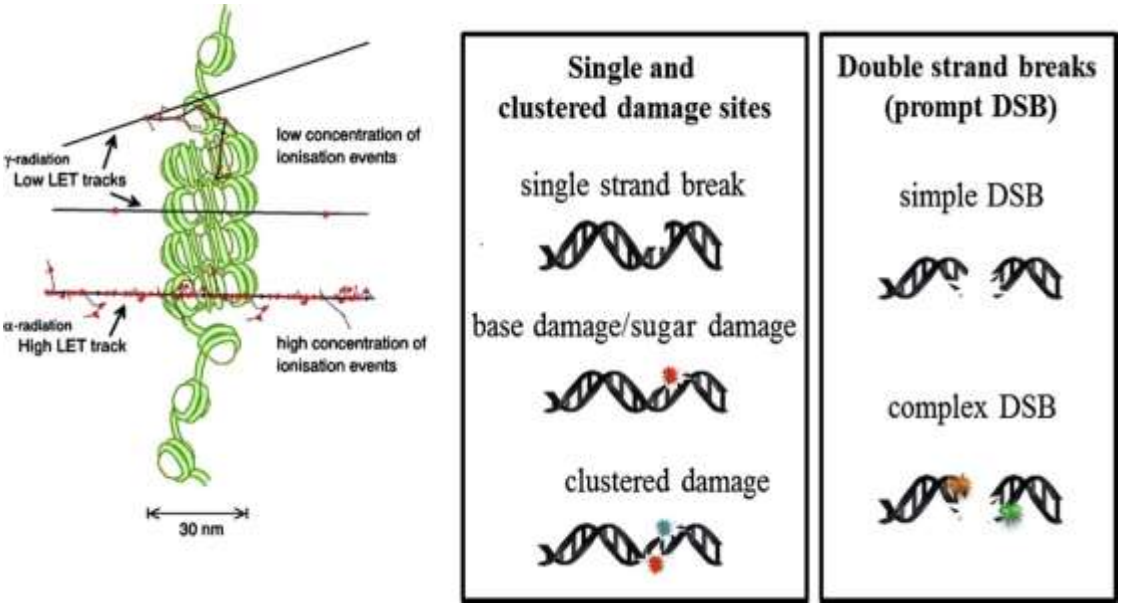

Figure 2: Simple and complex DNA damage sites caused by low vs high LET. (used with permission[18]).

With increasing LET, the complexity and number of clustered DNA damage sites increases[19]. These complex DNA damage clusters are often difficult for the cell to fully repair[20]. Furthermore, they can cause both double-stranded breaks (DSBs) or Oxidatively-induced Clustered DNA Lesions (OCDLs)[17], which have differing repair pathways with different repair fidelities. The repair of these can either be through nonhomologous end joining (NHEJ) or homologous recombination (HR). However, given the close proximity of the areas of DNA damage for these formed clusters, incorrect, or inaccurate repair can occur, especially given that multiple damage areas can occur within a repair replication fork[17].

Double strand Breaks (DSB) are often much more difficult to repair (discussed later), and are often thought of as the main driver of IR induced cellular damage and death[21]. The degree of double stranded breaks is highly dependent on (a) the IR energy, (b) the dose, and (c) how transcriptionally active a certain segment of the DNA[22]. The transcriptionally activity of certain segments of the DNA is rapidly changing depending on the cell cycle, which is the main reason why the consequence of radiation damage is cell cycle dependent[22–24].

High LET exposure is associated with prolonged DNA repair times, compared to a similar dose low LET exposure[25]. Furthermore, these more complex double stranded breaks seen with high LET, often lead to the activation of unique repair pathway

elements not seen with low LET based breaks[26–29]. A full in depth discussion of the DNA repair elements forming the repair complex are outside the scope of this work, however, a few key molecules must be mentioned.

Central to the DNA repair pathways after IR exposure is H2A.X and its phosphorylation by ataxia telangiectasia mutated protein (ATM)[21,25,30–33]. Following IR induced double stranded breaks, the kinase activity of ATM is activated after it "senses" these breaks, leading to the activation of a number of downstream targets including H2A.X, p53, p21 a number of cell cycle checkpoint inhibitors, and BRCA1[32,34], Figure 3[35].

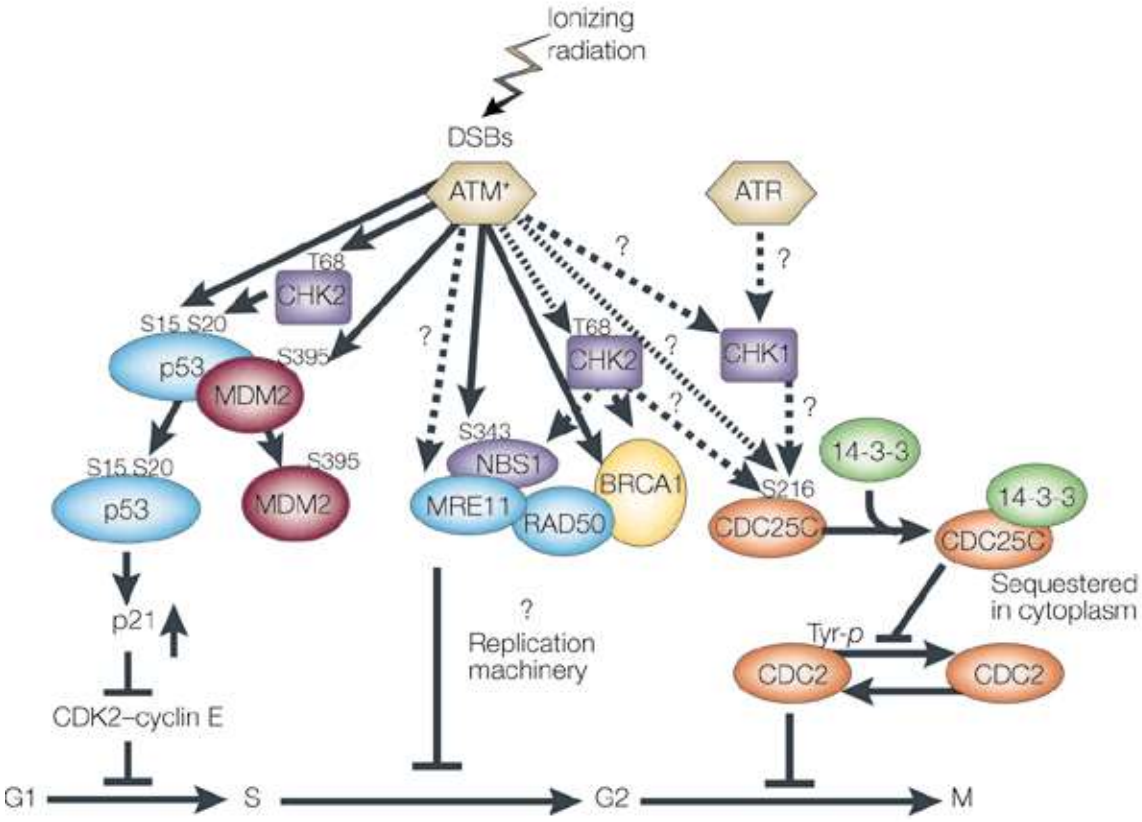

Figure 3: Role of ATM in sensing DNA breaks and activation of the downstream response (used with permission[35])

While most of the work done to elucidate the elements of this pathway has been focused in the cancer biology and radiation therapy fields, this highly conserved pathway in response to IR induced DSB is likely to also play an important role in cardiovascular dysfunction after IR.

1.3 Studies on radiation exposure and cardiovascular disease

Biologically, our cells have developed mechanisms to deal with natural background levels of radiation such as radon, however a dramatic increase of low dose

radiation secondary to increased medical imaging, radiation treatments and space travel scenarios are for the most part unprecedented. In a previous study that I co-authored, we studied the average radiation exposure during imaging follow up of patients with Thoracic Aortic aneurysms. On average, patients received an estimated 34Sv/patient or the equivalent of 11 years of background radiation, just for aortic aneurysm surveillance[36]. The first large scale study to suggest a risk of increased long-term cardiac mortality after radiation exposure was conducted by Tukenova et al. They evaluated 4,122 children who have received cancer related radiation to the heart. At an average follow up of 27 years, there was over an 8-fold increase in mortality compared to the general population, with a 5-fold increase in the estimated cardiovascular related mortality (CI, 3.3-fold to 6.7-fold)[37]. The study did not report on the average doses received to be able to calculate a minimal tolerated biological dose.

These studies, and others suggesting a long term cardiovascular effect from whole body radiation exposure have suffered from important limitations that, in some cases, invalidates their main conclusions[38–40]. Many of these studies are observational in design, where long term cardiovascular event rates in cancer patients receiving radiation therapy, were compared to age matched controls. However, given the strong inflammatory component of cardiovascular disease[41], and the inevitable intensified inflammation seen in cancer[42], the confounding effects is difficult to control. Prolonged

inflammatory activation seen in different cancers, as well as inflammatory suppression seen with treatments, can both influence cardiovascular events[43].

These studies also suffer from poor follow up, the dependence on administrative type databases to define cardiovascular events, and importantly, the largely estimated rather than measured radiation dose. These limitations are also seen in studies on the effect of space based radiation on long term cardiovascular mortality and accelerated atherosclerosis[44,45]. While one report suggested increased cardiovascular mortality for Apollo Lunar Astronauts[44], a different study using the same cohort failed to show an association after a different data analysis approach[46].

Animal studies have been used to simulate the effect of terrestrial and space radiation scenarios on cardiac function[15,16,47]. To study the space radiation environment, particle accelerators can generate single ion beams at fixed energies similar to what is expected in space. However, space radiation is much more complex, with a mixture of different ion species and energies. Recently, Galactic cosmic rays (GCR) simulation became possible at NASA's space radiation laboratory (NSRL)[12]. Animal studies so far, have led to conflicting conclusions, and had important challenges related to methods of assessment of cardiac injury[15]. All current studies for example used echo, analyzed by a single reader as the primary modality of assessment of cardiac function. Furthermore, available studies had limited follow up times, and no study has evaluated the effects of

more complex radiation scenarios that are likely to be experienced in space such as Galactic Cosmic Rays (GCRs)[12].

A more comprehensive discussion of radiation and cardiovascular disease can be found in chapter 2.

1.4 IR and reactive oxygen species production (ROS)

Central to cellular response to IR is the production of reactive oxygen species (ROS)[48–55]. Sources of ROS generation after IR are multiple, these include (a) radiolysis of cellular H_2O to electrons, charged Hydrogen atoms, OH^-, H_2, and H_2O_2 [56], (b) Mitochondrial ROS (mROS)[57], and (c) in response to the increased energy demand due to DNA repair[58,59]. Of those sources, mROS are the key contributors to the overall cellular ROS levels[60]. This is especially true given the ROS induced ROS pathways, where a positive feedback loop of mROS leads to a propagation of mROS release from nearby mitochondria[50,61,62]. This is made possible by ROS induced mitochondrial permeability transition pores (MPTP), and has been shown elegantly in cardiomyocytes, where mROS release occurs along long strands of adjacent mitochondria in a coordinated fashion[63].

Normally, different ROS species can be converted back to non harmful molecules as part of the cellular hemostasis. For instance, O_2^- is converted back to H_2O_2 (catalyzed by superoxide dismutase), and then H_2O_2 converted to H_2O and O_2 (catalyzed by catalases and peroxidases)[64]. As the levels of ROS within a cell increase, the electron

transport chain within the mitochondria are disrupted, and the increasing levels of ROS overwhelm the antioxidant system. These free radicals can create an oxidative stress environment reacting with lipids, proteins, and importantly with cellular and mitochondrial DNA, causing oxidative DNA damage[53,65–68].

One important area of investigation is the relationship between nuclear DNA damage after IR and subsequent mitochondrial ROS production. If such relationship exists, its mitigation might play an important therapeutic role in decreasing delayed cellular injury following acute IR exposure.

1.5 ROS, the vasculature and endothelial dysfunction

While ROS levels have deleterious effects in most cell type, increases in ROS in endothelial cells have unique consequences on endothelial cellular function[48,69,78–81,70–77]. Given that the endothelium lines the vasculature, changes in endothelial properties have important effects on all organs and the overall health of the organism. Therefore, no discussion of the long term cardiovascular consequences of IR exposure is complete a discussion of changes in the endothelium after IR[82,83,54]. Vascular endothelium plays key roles in maintaining normal blood vessel function, including regulating permeability, vascular tone and immune cell adhesion and transmigration into tissues[82]. The effects of radiation damage to the endothelium maybe either (a) direct, causing damage to the DNA or different organelles, or (b) indirect, leading to reactive oxygen species (ROS) that cause downstream organelle injury, DNA breaks, and cellular dysfunction[72]. One of

the important organelles directly implicated after high dose IR is the mitochondria[49] and increased mitochondrial release of ROS[84,55]. Both mitochondrial damage as well as increased cellular levels of ROS leads to endothelial senescence[75,85], however, that process remains to be fully uncovered for low to medium dose IR. Our central hypothesis is that low to medium dose IR causes cellular senescence indirectly through mitochondrial damage, and release of mitochondrial ROS (mROS) that negatively impacts cellular function and health.

1.6 Hypothesis and specific aims of the dissertation

The overall hypothesis of this dissertation is that Ionizing Radiation (IR) is associated with early subtle vascular and cardiac damage that has important implications for long term cardiovascular dysfunction. In the first part of this work, we test the hypothesis that low LET (gamma rays) and high LET (charged heavy ions, GCR) radiation are associated with long term changes in cardiovascular function.

In the second and third part of this proposal, we test the hypothesis that IR has an effect on both cardiomyocytes and vascular cells (endothelial and smooth muscle cells) early after radiation the drives long term functional derangement.

To test these hypotheses, we will use an animal model to study the effect of whole-body single dose radiation on long term cardiovascular function. Radiation types studied will include both high LET and low LET IR, which include gamma rays, single dose ^{56}Fe and ^{16}O heavy ions, as well as GCR. We will complement these studies with 2D

cells work investigating a number of the pathways involved in cardiovascular injury post radiation, as well as the use of unique microphysiological systems (MPS) to better replicate *in vivo* organ function. Therefore, the aims of this dissertation are as follow:

Specific Aim 1: Test the hypothesis that low dose (≤2Gy) whole body radiation (Gamma, ^{56}Fe, ^{16}O and GCR) leads to long term (9-12 month) cardiovascular functional changes. This will be done using a mouse model of whole-body radiation with follow up echocardiogram assessments, pressure volume loop assessment and cardiac MRI.

Specific Aim 2: Test the hypothesis that low dose radiation causes early changes in cardiomyocyte cellular function and proteomics signature. This was done using proteomics analysis of radiated cardiomyocytes 24 h post radiation, as well as the use of a functional cardiac patch system.

Specific Aim 3: Test the hypothesis that vascular cellular senescence (endothelial and smooth muscle cells) post radiation damage can be mitigated by using strategies to disrupting the ROS induced ROS feedback loop. Further, I investigated the relationship between DNA break sensing via ATM and secondary vascular cellular senescence. I compared the sensitivity of the vasculature as compared to cardiomyocytes post radiation exposure, to help provide a mechanistic understanding of the cell types involved in delayed cardiovascular dysfunction.

This research helped elucidate the role of radiation in delayed cardiovascular dysfunction, including providing some insight of the differential effect on

cardiomyocytes and vascular cells. It establishes a number of model system (in vivo and MPS) that can be used for additional screening of potential therapeutics including a number of robust endpoints for outcome measurements.

1.7 Significance and Innovation of the proposed aims

There is an important gap in our understand of the consequence of radiation exposure on short- and long-term cardiovascular function. Therefore, there is an imperative need to better define the long-term consequences of these different types of radiation exposure. Importantly, in this proposal we will develop two model systems (mouse model of long-term cardiovascular function after radiation and an MPS model of short/medium term effects on the heart and vasculature) to help further interrogate the cardiovascular phenotypic changes encountered after varying doses low and high LET radiation scenarios. Our proposed approach using 2D cells, MPS and in vivo experiments will serve as an important platform to further investigate causative mechanisms associated with radiation injury, as well as a screening tool for possible therapeutic mitigators. To demonstrate the utility of these systems, I investigated the role of mitochondrial-specific reactive oxygen species production after low to medium dose exposure to IR.

There are 3 main innovations in this dissertation, (a) the whole-body radiation animal model with a comprehensive multimodality method of assessing cardiac function, (b) the unique simulation of galactic cosmic ray radiation which has not been tested before

in the setting of the cardiovascular system and (c) the use of the humanized microphysiological systems to bridge the gap between cell work and in vivo observations. In this dissertation, an animal model was developed where different types of radiation scenarios can be tested and cardiac function evaluated long term. While a number of previous groups have used a particle accelerator to generate single ion radiation exposures, we added to that the use of GCR, made only possible recently due to recent advances in beam switching technologies[12]. GCR simulation allows for the most germane radiation environment to deep space radiation[15]. Methods of assessment of mouse cardiac function have been also limited, and largely dependent on single reader reviews of echocardiograms. Furthermore, echo might lack the sensitivity required to detect more subtle functional changes given the high error rate and user to user variability in acquiring imaging and assessment[86]. Finally, most current studies have relied on anesthetized animals during the echo exam[15,47,87], which is known to cause depression of cardiac function[88,89]. If expected functional changes are subtle, blunting cardiac function in the radiated and control mice secondary to anesthetic usage during the echo exam might be problematic. In our proposal, all mice echoes are performed on conscious animals by an experienced mouse echocardiographer (Appendix A). All echo analyses are completed by two independent reviewers, and are averaged. Furthermore, Pressure Volume Loops are performed on animals, as the gold standard method to evaluate cardiac function. Finally, MRI is used as a third independent functional

assessment tool to develop a comprehensive set of tools to interrogate cardiac structure and function.

In Aim 2 and 3, I focused on better understanding the differential contribution of the cardiac vs vascular system to long term cardiovascular dysfunction after IR. We carried out a set of experiments in cardiomyocytes and in relevant vascular cells (ECs and SMCs) to better understand the effect of radiation in those specific cells. Using a cardiac patch system, we evaluated changes in cardiac mechanical and electrical properties at 24 hr after IR. We also performed a proteomics analysis of cardiomyocytes to evaluate important changes in the proteome and different cellular process that are involved.

Finally, I carried out radiation experiments in ECs and SMCs, to better understand changes in cellular senescence after different radiation scenarios that may have important implications to future vascular health. These changes were further interrogated by the use of therapeutics that help shed light on the involvement of the DNA repair pathway and mitochondrial ROS production through their mechanisms of action. Combined, these studies help define the differential response of cardiomyocytes vs that of vascular ECs and SMCs in the development of radiation injury to the cardiovascular system.

2. Long term cardiovascular dysfunction resulting from galactic cosmic ray exposure

Space exploration is associated with higher doses and different types of radiation than what is experienced by an average person on earth. Epidemiologic studies suggest an increased risk of delayed cardiovascular events when background radiation levels are increased. In this study, we used a mouse model of whole-body radiation at the NASA Space Radiation Laboratory (NSRL). Mice were exposed to escalating doses of Gamma rays, Single Heavy Ions, and Galactic Cosmic Radiation (GCR). We found that GCR treated mice, in comparison to controls, Gama rays and single heavy ions, have a significant impairment in cardiac function. GCR also increases arterial elastance likely due to elastic fiber disruption. Our data suggest that a single exposure to 150 cGy of GCR is associated with clinically meaningful deterioration of cardiac function that becomes apparent long after exposure, a finding that has implications to space exploration.

2.1 Background and introduction

Planned missions to the moon and Mars have rekindled an interest in human space travel. Space travel raises a number of biological risks, most importantly the risk of human exposure to space radiation [90]. Unlike the natural radiation encountered on earth, humans traveling to space may be exposed to both high energy heavy ion radiation and galactic cosmic rays (GCR)[15]. Data from NASA's Curiosity Mars rover

estimates that a human Mars mission will be associated with a 120cGy of radiation exposure, a dose that is nearly 200-fold higher to what an average person on earth is exposed to in one year[15]. Even at low doses, acute radiation exposure on Earth has been associated with a higher rate of delayed cardiovascular related morbidity and mortality [38–40]. However, previous studies have suffered from confounders such as cancer comorbidity, poor follow up, and limited understanding of estimated radiation exposure, thereby softening their impact for estimating the risk of human space travel.

Studies specifically examining on the effect of space radiation on long term cardiovascular mortality and accelerated atherosclerosis have yielded conflicting results [44,45]. In the same cohort of Apollo lunar astronauts, one report suggests increased cardiovascular mortality as a consequence of space radiation[44], while another study does not show this relationship [46]. Recent studies have pointed to distinct injury patterns associated with space travel that may enhance cardiovascular risk. A NASA twin study demonstrated that, in comparison to control, a twin traveling at low earth orbit on the international space station (ISS) for 1 year developed both genetic modifications (altered telomere length and DNA methylation) and markers of increased cardiovascular risk (carotid intima-media thickening and increase in the APOB/APOA1 ratio)[91]. However, it is unclear whether these constellation of molecular and biochemical changes are due to radiation exposure. Thus, gaps in our understanding of the magnitude and biology of

space radiation on cardiovascular function are a significant barrier to safe human space travel.

Six-month old C57BL/6 mouse males exposed to distinct forms of terrestrial and extra-terrestrial radiation at NASA's Space Radiation Laboratory (NSRL) and performed longitudinal cardiac phenotyping. Phenotyping strategies included transthoracic echocardiography (TTE), cardiac MRI (cMRI) and terminal pressure volume loop assessment (PVL). We hypothesized that exposure to radiation that mimics space radiation would cause deterioration of cardiac function. We found clinically significant deterioration of cardiovascular function one year after a single exposure to GCR whole body radiation.

2.2 Methods

2.2.1 Study design and radiation scenarios

Five month old C57BL/6 male mice were purchased from Jackson Laboratories and shipped to Duke university. They underwent baseline echocardiograms, and were then shipped to BNL for radiation experiments. They were allowed an acclamation period of two days prior to any radiation exposure. Radiation experiments were conducted at Brookhaven National Labs (BNL), NASA Space Radiation Laboratories. Gamma exposure animals were also exposed to their Gamma doses during those same days. Finally, control animals were placed in similar radiation holders, for the same amounts of times during the same radiation days. Post radiation, animals were allowed

a few days to recover, and then were shipped back to Duke University animal facilities where they underwent their follow up exams.

Table 1: Number of animals evaluated for each exposure group

Exposure Type	Pre radiation Echo	9M post radiation Echo	9-12M post radiation PVL loop
Ctrl	48	39	10
15cGy Fe	20	20	
25cGy Fe	20	20	
50cGy Fe	25	20	10
50cGy Ga	20	19	
100cGy Ga	20	19	
200cGy Ga	25	19	8
15cGy ^{16}O	19	19	
25cGy ^{16}O	19	19	
50cGy ^{16}O	20	20	10
GCR Ctrl	24	21	10
GCR	35	34	10

The radiation types and doses were chosen with the guidance of NASA's radiation biology leadership to be representative of those experienced during a Mars mission (Table 1). Radiation exposures were (a) single dose of 15cGy, 25cGy, or 50cGy Fe^{56}, (b) escalating doses of 15cGy, 25cGy, or 50cGy Ox^{16}, (c) escalating doses of 50cGy, 100cGy, or 200cGy Gamma rays, and (d) one 150cGy dose of Galactic Cosmic Rays (GCR). After radiation, the exposed mice and age matched travel control mice were

shipped back to Duke University where they were followed over time. At 1-year post radiation, all animals underwent transthoracic echo, and a subset had cardiac MRI and Pressure-Volume loop assessment (Figure 4). (A). One year post radiation, assessments of cardiac function included awake echocardiography (B), cardiac MRI (c), Pressure volume loop assessment (d), and cardiac/aortic histology (e).

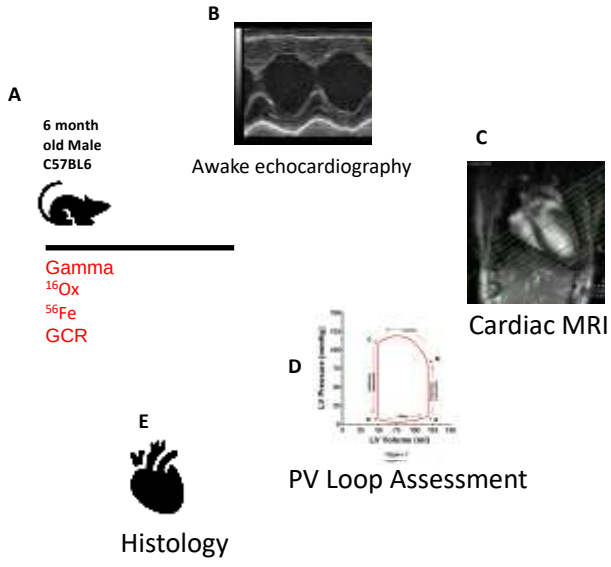

Figure 4: Experimental setup for the mouse radiation experiments. 6 month old mice are exposed to different radiation scenarios and undergo a number of cardiac assessments including echocardiography, cardiac MRI and PV loop assessment and histology. 2.2.2 Changes in cardiac function measured using echocardiography

Cardiac functional assessments in mice rely heavily on transthoracic echocardiograms [16,87,88]. Animal studies that examine the effect of radiation on cardiac function using echocardiograms have led evidence of a possible cardiac functional deterioration after heavy ion exposure, however the data was inconsistent with some

radiation scenarios showing functional improvements [15]. This is likely due to a number of factors including (a) most studies used healthy wild type mice and sedated echocardiography as the primary method of cardiac assessment, which could miss small subtle changes resulting from sedation, (b) all prior studies used only one reader, with unclear prior internal validation of reads, which is problematic given the large variability in mice echocardiograms [86].

For this study, all echocardiograms were performed at our center's echocardiography animal core laboratory. Animals were pre conditioned (by being held in the same manner as the echo) and shaved the day before to decrease stress during the procedure. Animals underwent awake echo by an experienced echo technologist. All echo images were blinded to the animal radiation assignment and were uploaded to a centralized server. The echos were independently analyzed by two independent cardiovascular clinicians (MB and DA), who both have read over 500 mouse echos prior to the performance of this study. After all the echos were analyzed in a blinded fashion the reads were compared and the difference between each mouse reads were calculated for fractional shortening (FS). The average difference across all mice was calculated with the standard deviation (SD). Reads that were more than 2SD away from the mean, were re read by both readers together, and all three reads for those animals were compared. On average, the reads differences were normally distributed, with less than 10% of reads

falling outsides of 2SD (Figure 5). For the remainder of the mice, both reads were averaged for all animals.

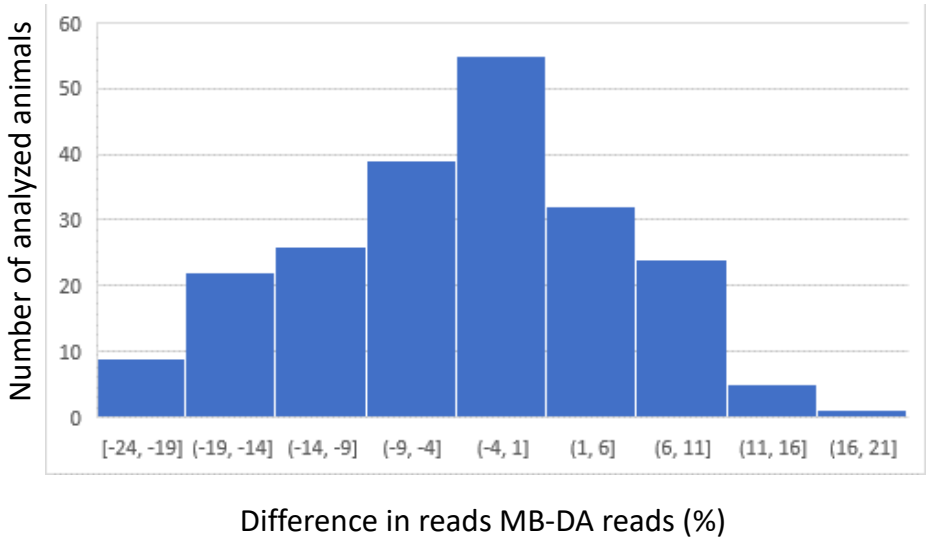

Figure 5: Distribution of reader error for mouse echocardiograms. Differences in reads for fractional shortening between the 2 independent readers follow a standard curve, with no systematic error noted

A number of parameters were measured on echo including wall thicknesses in systole and diastole, ventricular volumes, measures of systolic function including Fractional Shortening (FS) and Ejection Fractions (EF), Heart Rate, and measures of diastolic function such as Isovolumetric Relaxation Time (IVRT), passive LV filling (E'), and ratio of early to late filing of mitral inflow (E/A). Given the known of effect of anesthesia on cardiac function, we performed conscious echocardiograms on mice, which were then analyzed by two independent clinicians blinded to exposure conditions.

2.3. Results

2.3.1 Changes in cardiac function measured using Trans Thoracic Echo (TTE)

Using TTE, small differences in heart rate (Figure 6A) and systolic function (Figure 6B, 6C) between age-matched control mice to animals receiving GCR radiation were detected. Diastolic function was no different between groups (Figure 6D-F).

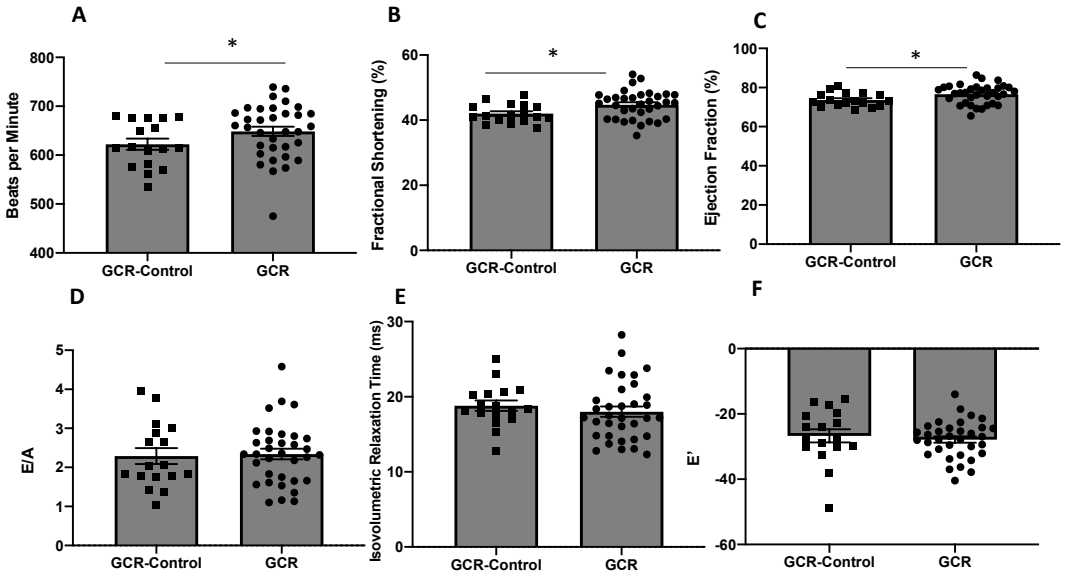

Figure 6: Echocardiographic changes one year post GCR radiation. There is no clinically meaningful change in heart rate, FS, EF, E/A, IVRT, or E' between the control and GCR radiated animals.

While some of the changes seen were statistically significant (FS, EF and HR), the total effect size difference between the GCR treatment and GCR controls were negligible and reached statistical significance due to the large sample size used. For instance, the median difference in percent fractional shortening between GCR and GCR-controls was

-2.8 with 95% Confidence interval of -5.4 to -0.36). (N= 17 for controls, and 34 for GCR animals. Statistics, Nonparametric Mann Whitney test, 2 sided)

The same was true for EF, with a median difference of -3.4 (95% CI -6.1 to -0.30) There was no difference in Heart Rate (HR) and systolic functional assessments between age control animals (N=39), and those exposed to single ion Fe^{56} (N=19-20) 15cGY, 25cGy, and 50cGy, Ox^{16} (N=19-20) 15cGy, 25cGy, and 50cGy, or Gamma (N=19) 50cGy, 100cGy, and 200cGy one year after radiation (Figure 7, 8, 9 panels A-C). This was also true for measures of diastolic function (Figure 6, 7, 8 panels 2D-F)

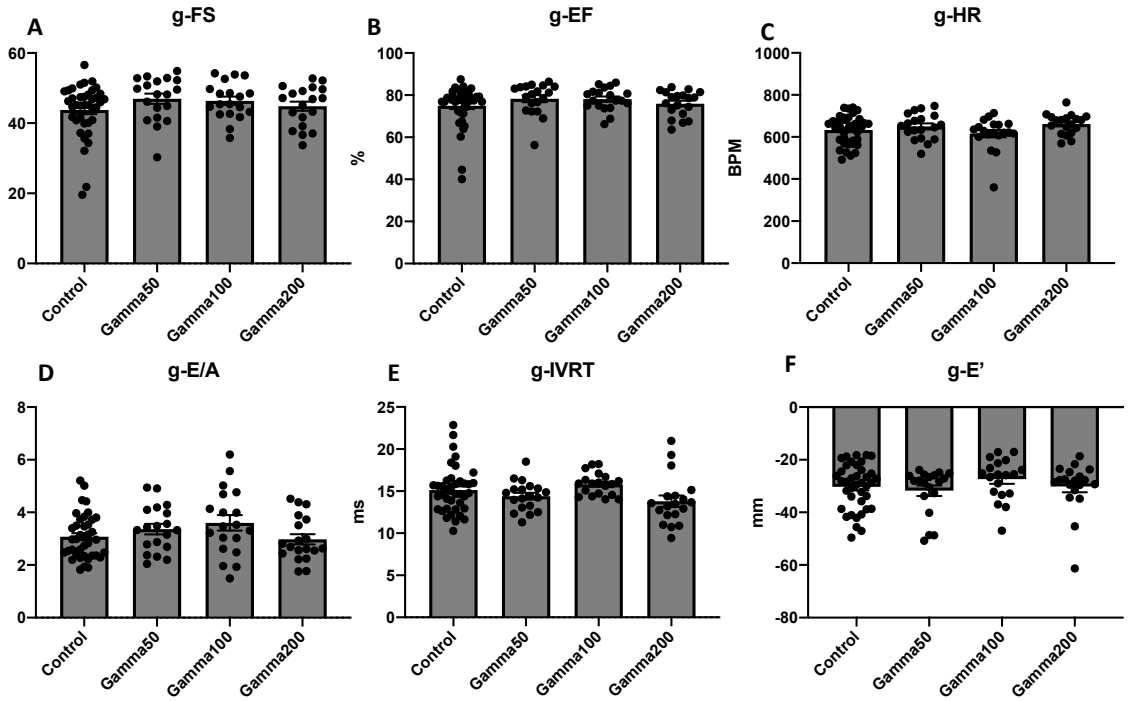

Figure 7: Echocardiographic changes one year post Gamma radiation. There is no clinically meaningful change in heart rate, FS, EF, E/A, IVRT, or E' between the control and gamma radiated animals.

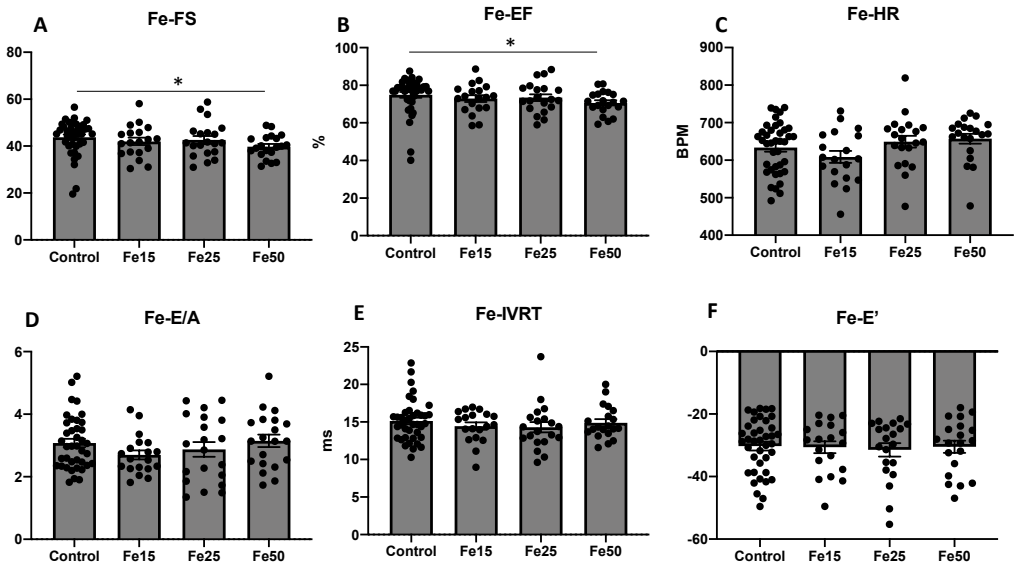

Figure 8: Echocardiographic changes one year post Fe radiation. There is no clinically meaningful change in heart rate, FS, EF, E/A, IVRT, or E' between the control and Fe radiated animals.

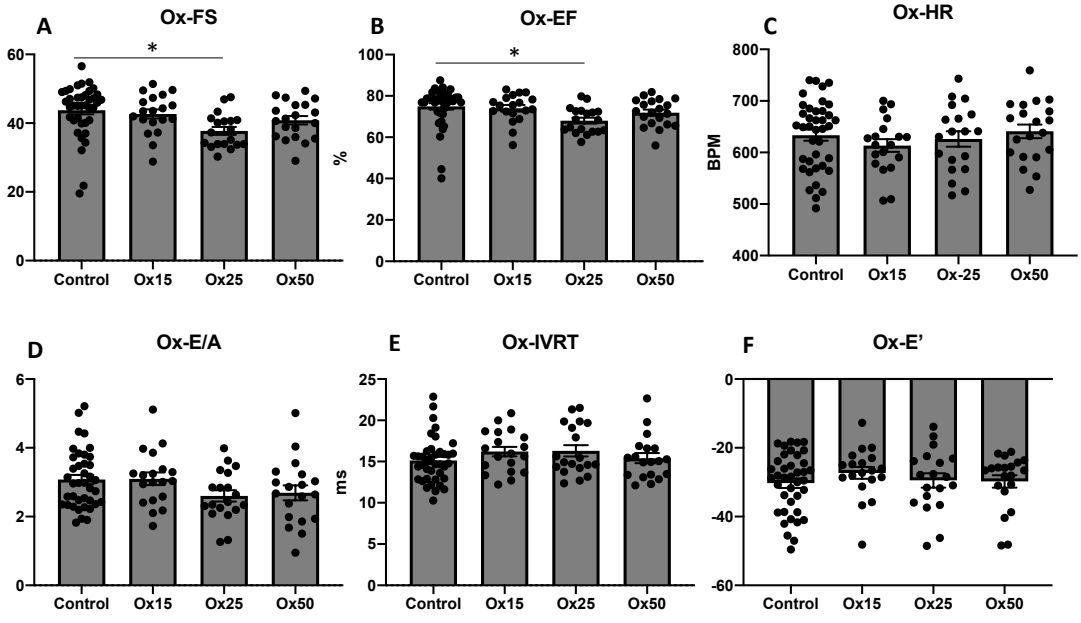

Figure 9: Echocardiographic changes one year post Ox radiation. There is no clinically meaningful change in heart rate, FS, EF, E/A, IVRT, or E' between the control and Ox radiated animals. 2.3.2 Changes in cardiac and vascular function measured using Pressure volume loop assessment

A subset of animals underwent Pressure Volume Loop (PVL) assessment prior to euthanasia. All PVL procedures and analyses were performed at our center's cardiovascular physiology core by an experienced microsurgeon[92–94]. Parallel conductance (Vp) was determined by 10 μl injection of 15% saline into the right jugular vein to establish the Vp of the blood pool. The derived Vp was used to correct the pressure-volume loop data. Data were recorded digitally at 1,000 Hz and analyzed with pressure-volume analysis software (PVAN data analysis software version 3.3; Millar Instruments). Mice that died after receiving anesthesia or became hypotensive during the course of the protocol, suggesting a surgical complication (LV rupture, bleeding, arrythemias), were excluded. Next, a small laparotomy was performed, and the inferior vena cava occluded to decrease preload to the heart in order to measure load independent parameters. After completion of the PVL measurements, the animals were euthanized and tissue isolated and bio preserved.

Pressure volume loop (PVL) testing is considered the gold standard for the evaluation of preload dependent and independent cardiac function measurement [95]. At one-year post radiation, a randomly selected subset of animals underwent PVL testing. There were no meaningful differences in Stroke Work (SW), Stroke Volume (SV), Cardiac Output (CO), Ejection Fraction (EF), dP/dTmax, Preload recruitable Stroke Work (PRSW), Tau, or Arterial Elastance (Ea) for 50cGy Fe, 50cGy Ox, and 200cGy Gamma as compared to age matched controls (Figure 9).

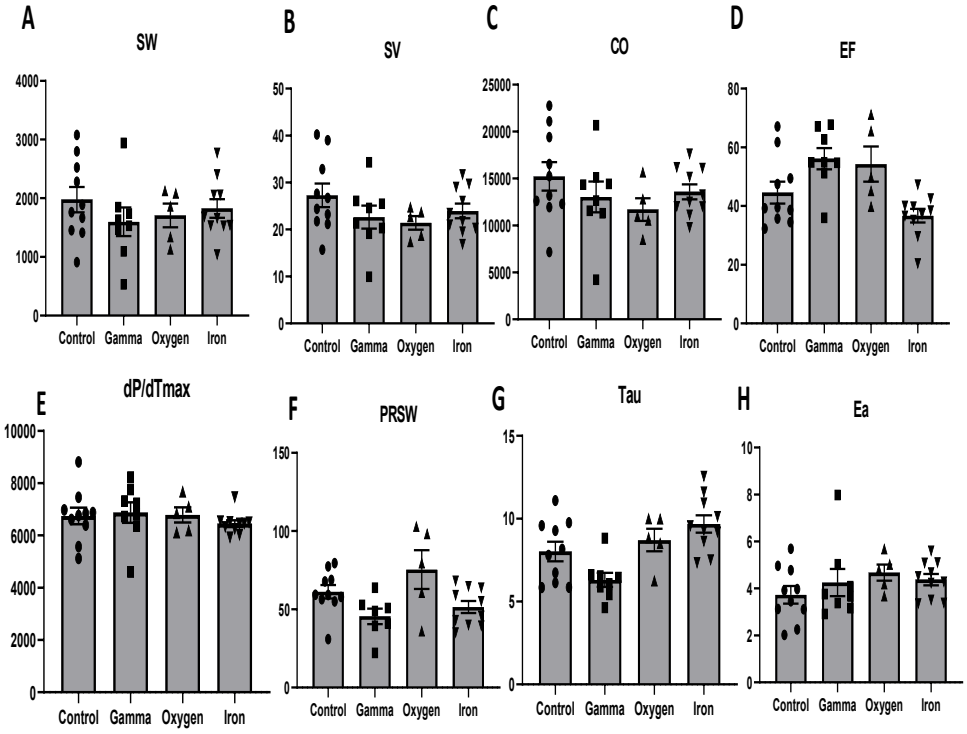

Figure 10: Changes in pressure volume loop assessment for single ions one year post radiation. There is no difference in stroke work, stroke volume, cardiac output, ejection fraction, change of pressure over time, preload recruitable stroke work, Tau or arterial elastance for 200cGy Gamma, 50cGy Ox, or 50cGy Fe compared to control

Mice that underwent 150cGy of GCR radiation were noted to have important and clinically meaningful drops in load dependent measures of cardiac function including Stroke Work (SW), Stroke Volume (SV), and Cardiac Output (CO) (Figure 11).

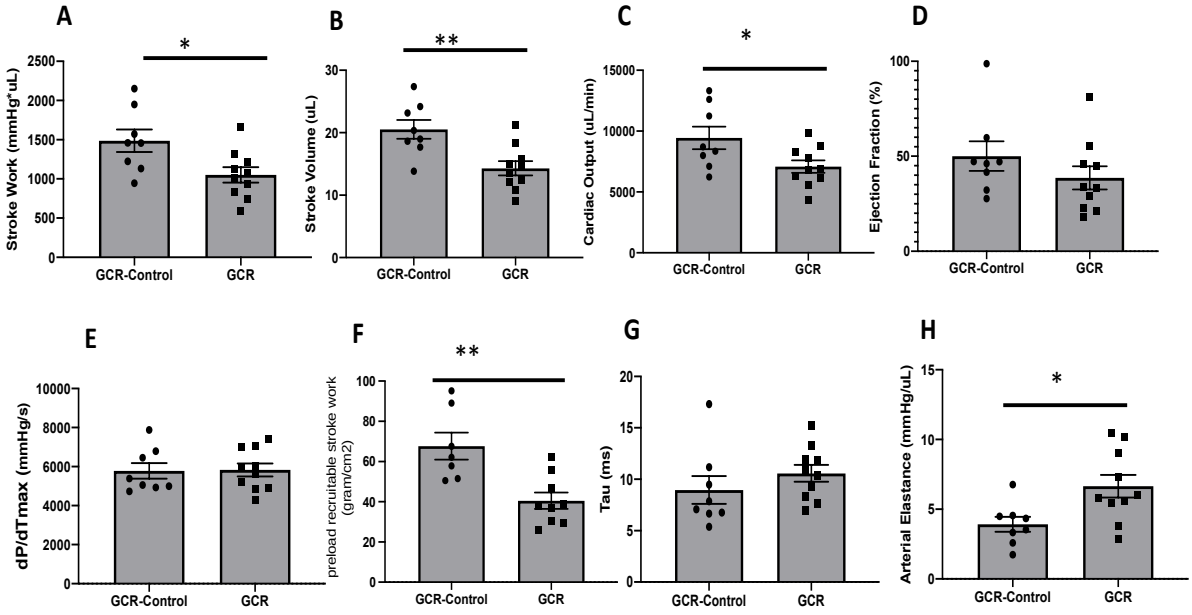

Figure 11: Changes in pressure volume loop parameters one year after GCR radiation. GCR radiated animals had a large drop in stroke work, stroke volume, cardiac output, ejection fraction and reload recruitable stroke work compared to control. These animals also had a large increase in arterial elastance compared to controls

Furthermore, load independent Preload Recruitable Stroke Work (PRSW) was significantly reduced by nearly 30% in GCR exposed animals. For instance, the median difference of PRSW between GCR and GCR control was -25.21%, with a 95%CI (-48.4%1 to -11.74%). Finally, arterial elastance (Ea) was significantly increased in GCR animals as compared to controls (Figure 10H). To confirm that the subset of animals that were randomly chosen for PVL had echo result similar to the larger cohort of mice, as a sensitivity analysis we analyzed the echocardiograms of PVL animals, demonstrating no

observed differences on echocardiograms, and consistent with overall echocardiogram data for the overall cohort.

2.3.3 Changes in animal weights, blood pressure and overall survival after radiation

Epidemiological studies of long term cardiovascular risk after radiation exposure have reported increased rates of hypertension[96]. Furthermore, given the changes seen on PVL for arterial elastance, animals underwent blood pressure and weight measurement (Figure 11). There appears to be no difference in systolic, diastolic or mean tail cuff blood pressure for GCR vs control animals. Furthermore, the GCR and control animals had comparable weights at the study conclusion (Figure 12).

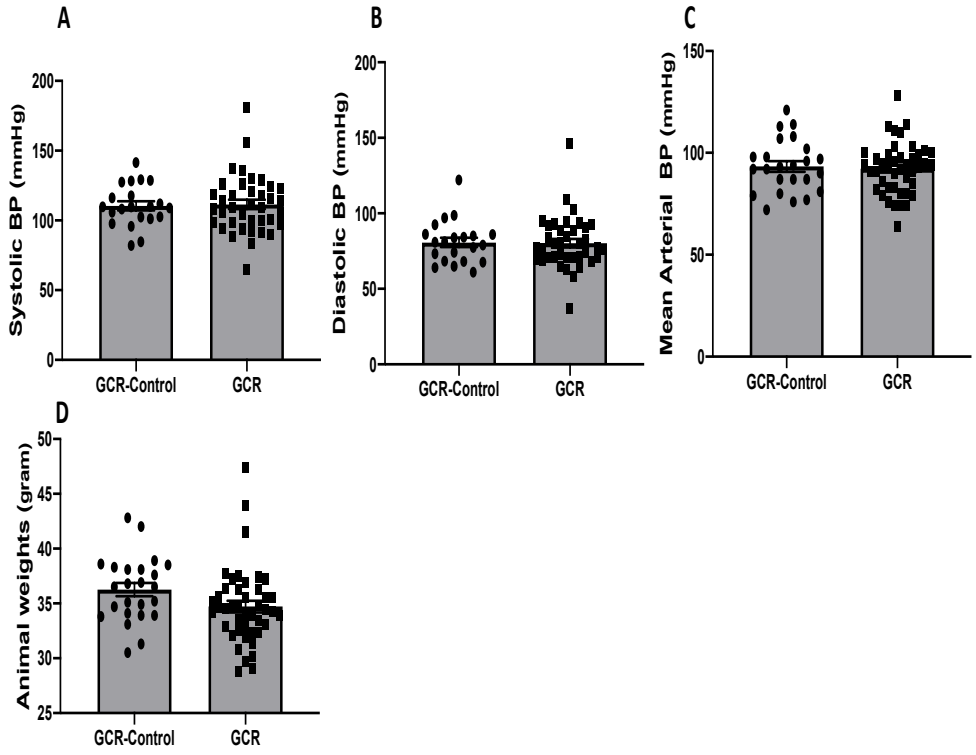

Figure 12: Changes in animal weights and blood pressure after radiation. There is no difference in systolic or diastolic blood pressures, and animal weights one year after GCR radiation Furthermore, there was no changes in overall survival between the GCR and control animals as seen in the survival figure below (p=0.12).

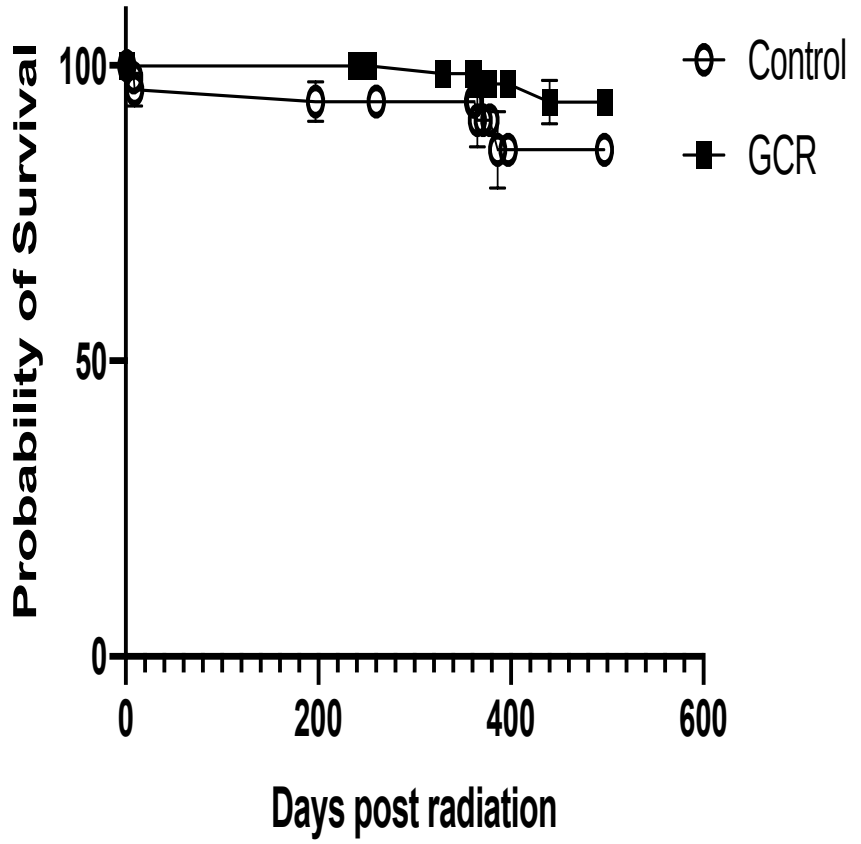

Figure 13: No difference in overall survival between GCR and control animals one year after radiation exposure

Interestingly, the Fe radiated animals had a decrease in their long term survival compared to the controls for the 50cGY radiated animals (p=0.04). This was all cause mortality, and was unique to the Fe radiated animals. There was no differences in survival for the Ox or Gamma ray animals. (Figures 14)

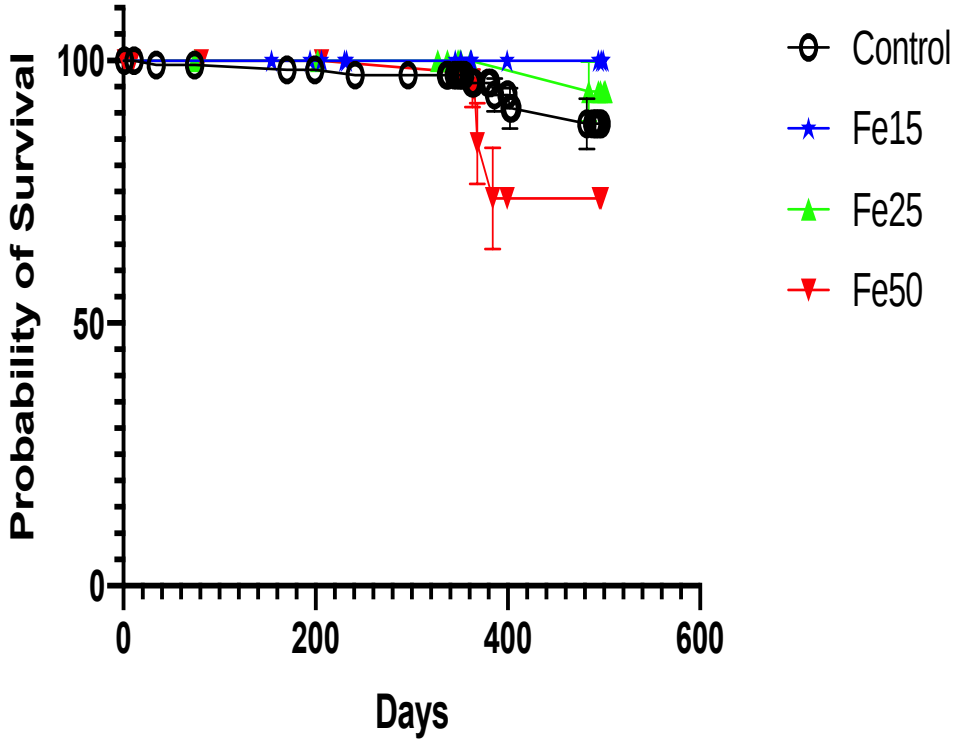

Figure 14: Differences in survival for Fe radiated animals. Animals receiving 50cGy or Fe radiation had worse long term survival compared to controls

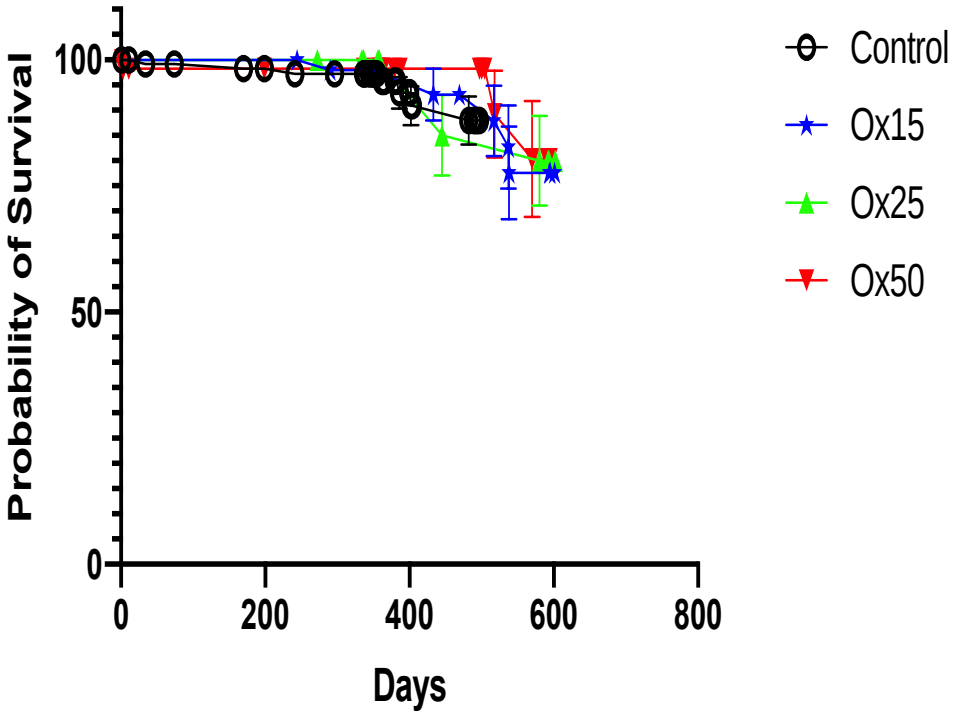

Figure 15: No Differences in survival for Ox radiated animals compared to controls one year after radiation

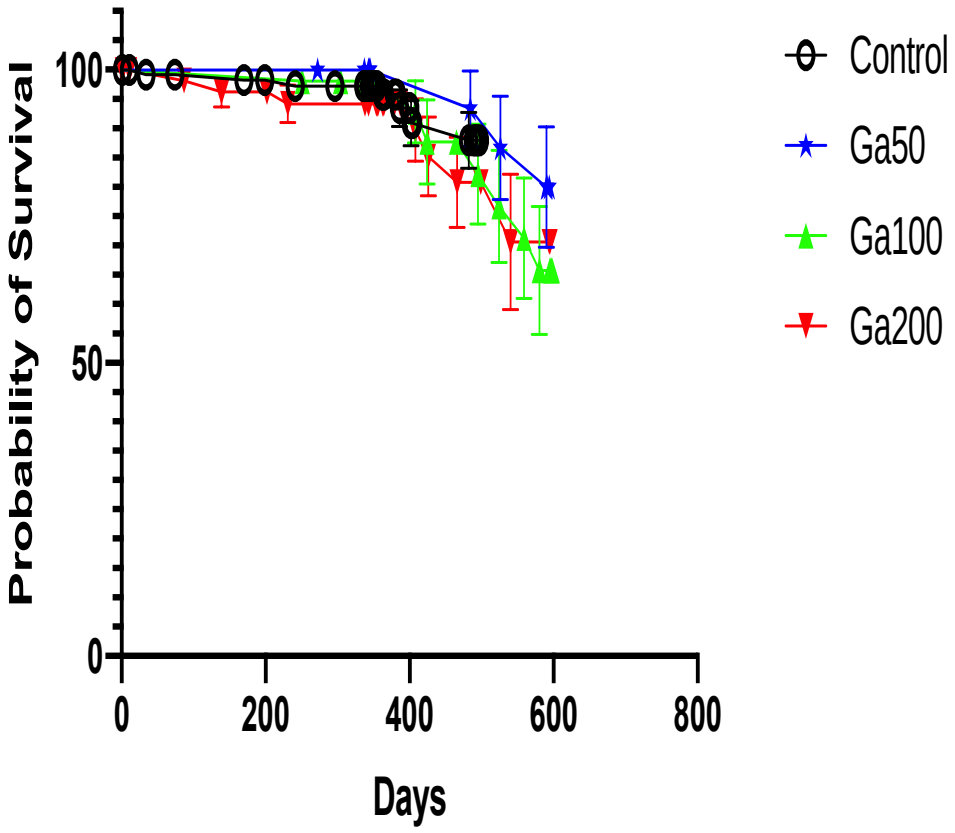

Figure 16: No differences in survival for Gamma radiated animals compared to controls one year after radiation

2.3.4 Changes in cardiac structure and function using Cardiac MRI after GCR radiation

Cardiac MRI (cMRI) represents an important modality for the assessment of a number of cardiac functional and structural characteristics[97]. All cMRI evaluations were performed at our center's small animal imaging core facility. Experiments were performed on a 7.0 T Bruker Biospec small animal MRI scanner (Bruker Inc., Billerica, MA). Animal anesthesia was induced and maintained with inhaled isofluorane (0.5-2.0%), and breath rate was monitored for the duration of the scans. Animals were

positioned on a custom 3D-printed bed and body temperature was maintained with warm water circulation.

Images were acquired using ParaVision® 6.0.1 platform (Bruker Inc.) with a mouse brain receive-only four coil array combined with a 72 mm diameter actively decoupled linear volume coil for transmission. Cardiac time-course images were acquired using an intra-gated multi-slice T1-weighted cine FLASH sequence (TE/TR = 2.0/88.6 ms; 0.1 X 0.1 X 0.8 mm voxel size; 8 slices; 12 frames/cardiac cycle), with the addition of a bright-blood pulse to enhance blood pool signal without the need for an injected contrast agent. Slice orientation was adjusted to take serial slices perpendicular to the long axis of the heart, such that the 0.1 mm2 in-plane slices demonstrated cross-sections of the LV which was verified by a cardiac clinician (MB).

Images were analyzed using 3D Slicer open source image analysis software (www.slicer.org), as well as Image J (https://imagej.nih.gov). At each timepoint throughout the cardiac cycle, LV volume was measured by manual segmentation of each slice. Cardiac wall thickness was measured using Image J, with the location standardized using the papillary muscles. Linear distances in 6 radial positions across the LV at peak systole and diastole, and all measurements were performed in triplicate to assess measurement precision. The animals were only kept under isoflurane for less than an hour, as cardiac function drops over time as a result of prolonged sedation. The animals were recovered after the completion of cMRI image acquisition.

To further characterize *in vivo* changes in cardiac structure and function associated with GCR radiation, a subset of animals underwent detailed cMRI evaluation. While there appears to be no difference in SV and LV thickness during systole, a small change was detected for LV thickness at end of diastole for GCR animals as compared to controls , 1.02 mm vs 1.15 mm, respectively (difference of 0.13mm, 95% CI -0.24 to -0.01, p=0.032) (Figure 17). Finally, changes in cardiac volumes across the cardiac cycle between the groups appeared to be similar.

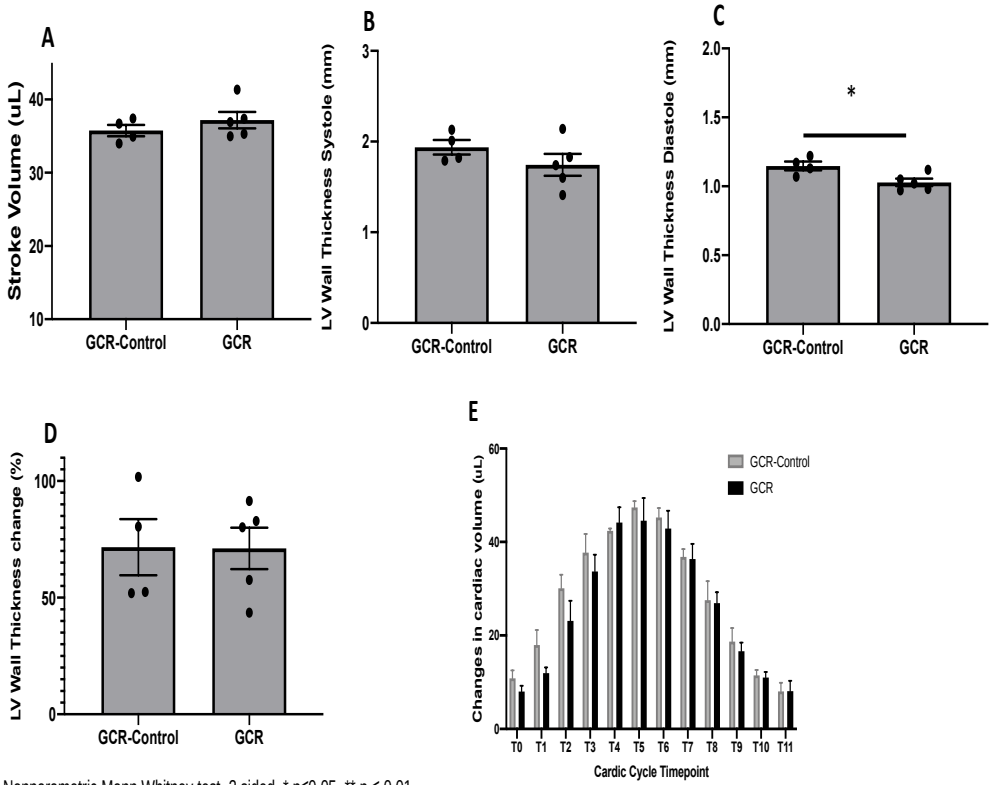

Figure 17: Cardiac MRI changes post GCR radiation. One year post radiation, GCR radiated animals did not have clinically meaningful changes in stroke volume or wall thicknesses compared to controls.

2.3.5 Histological assessment of mouse aortas after radiation exposure

At the time of euthanasia, animal hearts were rapidly extracted and flushed with heparanized saline, then fixed using 4% PFA overnight. They were then transferred to PBS and underwent paraffin imbedding and sectioning by our histology core facility. The aorta was similarly treated, and sectioned in the short axis. All staining was done by our histology core facility according to established inhouse protocols. A clinical cardiac pathologist (Dr Glass) evaluated all finished slides in a blinded fashion including grading of elastic fiber changes, and fibrosis in the myocardium.

To further evaluate structural changes in the mice after GCR exposure, a subset of animals receiving GCR and similar controls underwent histological evaluation of heart and aorta. While there was no significant change in cardiac fibrosis between groups, evaluation of the thoracic aorta revealed an overall increase in elastic fiber fragmentation, thickening and degeneration as evaluated by a blinded cardiovascular pathologist (Figure 18 and Table 1). In Figure 18, A-C represent H&E staining, and D-F represent immunofluorescence against elastin (and DAPI).

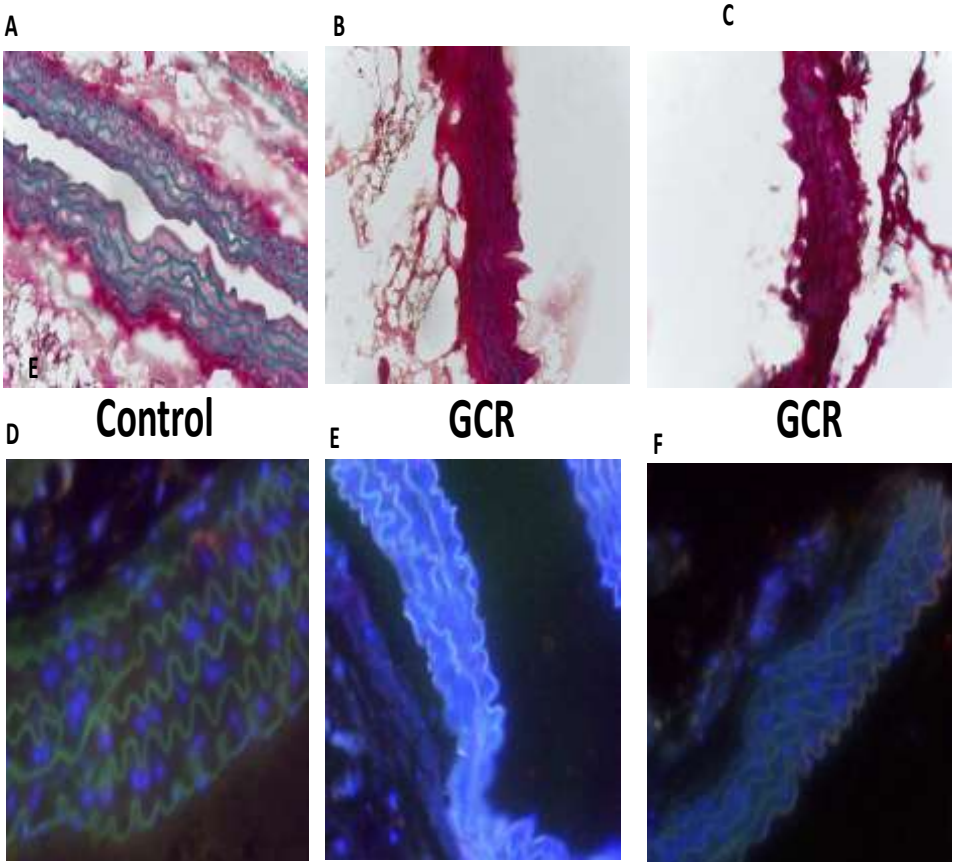

Figure 18: Elastic fiber changes in the aorta one year after GCR radiation. Using Masson Trichrome (top panel) or immunofluorescence (bottom panel), GCR radiated animals have more elastic fiber fragmentation compared to age matched controls.

Table 2: Histological assessment of radiated mice aortas

Group	Medial necrosis	Elastic fiber fragmentation	Elastic fibers characterization
GCR	None	None	Thick
GCR	focal	Multi-focal, disorganized	Thick
GCR	None	Focal, disorganized	Thick
GCR	focal	Focal, disorganized	Thick
GCR	Multi-focal	Multi-focal, severe degeneration	Degenerated
GCR	focal	Focal, disorganized and degenerate	Degenerated
Control	focal	None	Normal
Control	None	Focal	Normal
Control	None	None	Normal

2.4 Discussion

In this study we report for the first time clinically meaningful changes in resting load dependent and independent measures of cardiac function, as well as a significant increase in resting arterial elastance one year after exposure of mice to GCR radiation. Further, changes in arterial elastance appear to be related to long term damage in aortic elastic fibers.

There has been a number of animal studies that simulated the effect of terrestrial and space radiation scenarios on cardiac function [15,16,47]. Available studies to date had

limited follow up times, limited methods of evaluating cardiac function, and no study has evaluated the effects of more complex radiation scenarios that are likely to be experienced in space such as Galactic Cosmic Rays (GCR)[12]. To study the space radiation environment, particle accelerators have been used to generate single ion beams at fixed energies similar to what is expected in space. However, space radiation is much more complex, with a mixture of different ion species and energies, scenarios that are not existent on earth [98]. Recently, Galactic cosmic rays (GCR) simulation became possible at NASA's space radiation laboratory (NSRL)[12], making the current report possible.

In this study, we use multiple modalities to assess cardiac function (Echo, PV Loop and MRI). We chose a comprehensive approach for cardiac evaluation given the limitations of different testing modalities, and the need to compare measures across modalities for validation. Despite reporting large and clinically meaningful differences in cardiac function after GCR using PVL testing, we failed to see differences on echocardiography. This can help explain inconsistency in the current animal literature using echocardiography as the primary method of cardiac functional assessment. Another important difference is the use of awake echo which we did in our studies, vs echocardiography under sedation used with the majority of reports today [16]. Given the negative inotropic effect of isoflurane on cardiac function[86], such effect might mask more subtle differences in cardiac function related to the treatment effect. Evaluation of mouse echocardiographic studies requires rigorous quality assurance mechanisms, where

significant variability exists even among experienced readers. For instance in our study, we used two independent experienced clinician evaluators for all echocardiogram assessments, that were both blinded to the study group of each animal. To our knowledge, of the current available literature in this field, we are the first to use such robust methodology of echocardiogram analysis on such a large cohort of animals.

Pressure volume testing demonstrated important and consistent changes in load dependent and independent measures for GCR exposed animals. These changes had a similar large effect size across multiple measures. Of note, arterial elastance was increased, which is consistent with a number of clinical reports of changes in arterial stiffness after radiation exposure [99]. These vascular changes maybe the primary drivers of cardiovascular function changes seen, or are taking place in combination with a primary cardiac injury. For instance, significant increases in arterial stiffening will lead to a secondary systolic function decline given the large increases in afterload. Therefore, the changes seen in our systolic functional assessments with our mice might be a secondary effect of a primary arterial elastance. This was further investigated with histological assessments of the thoracic aorta and the myocardium. This revealed important changes in elastic fiber integrity and organization for the GCR exposed animals as compared to age matched control animals.

These changes in the elastic fibers are likely to have important changes in the aorta's pressure response [100]. While aging is associated with important changes in the

integrity of aortic elastic fibers [101], GCR exposed animals had significant deterioration as compared to the aged matched controls. Elastic fiber integrity is critical for the Windkessel effect, which is important for proper blood pressure control and secondary organ blood flow [102]. Typically, such changes in aortic elastance would be associated with measured blood pressure changes, something we failed to see in our study. In fact, the blood pressure of our GCR exposed animals was similar to the age matched controls. This however can be due to limitations in obtaining sensitive tail cuff blood pressure in mice.

There are a number of important limitations of this study, and how it relates to human space travel and radiation risk. In this study, the entire dose was delivered acutely to the animals, which is different than the slow and chronic exposure that would be experienced during space travel. In fact, this is a limitation of all studies using particle accelerators to simulate the space radiation environment. According to NASA, each cell in an astronaut's body in deep space is traversed by a proton every three days, by a He nucleus every few weeks, and by a heavy ion every few months[12]. This corresponds to a dose rate of 0.3–0.6 mGy/day. This is significantly lower than the dose rate delivered during our studies. Therefore, the findings reported in this study will need to be validated by more long term chronic radiation exposure experiments when those become available.

Another important limitation of this study, is the inability to fully tease apart the important elements of the GCR exposure that caused the biological effect reported. The GCR designed and delivered at NSRL is aimed at simulating organ exposures within a shielded spacecraft with the majority of the total GCR dose derived from protons (50–60%) and alpha particles (10–20%), and the remainder coming from heavier ions and secondary particles [12]. Therefore, it is unclear if this combination of energy particle exposure was needed for the reported biological effect, or if the effect was primely due to certain elements of the GCR, such as protons. While we had single ions for Oxygen and Iron heavy ions, we did not have a single exposure to proton group. There is recent evidence to suggest that proton exposure alone is associated with long term alterations of the proteome in both the heart and the brain[87,103].

In this study, we report for the first time clinically meaningful changes in cardiac function for GCR exposed healthy animals as compared to age matched controls. This effect was only seen for GCR exposure and not for the studied single ion or Gamma exposed control animals. These findings have important implications for current and future plans of deep space exploration by NASA.

3. Early functional and proteomic changes to cardiomyocytes post IR

3.1 Introduction

There has been a dramatic increase in the dose of radiation exposure for an average American today, mainly due to medical based imaging and uses[2,104]. For example, one Positron Emission Tomograph-CT (PET-CT) scan is associated with an acute radiation dose of 25mSv. This is equivalent to nearly 8 years worth of background natural radiation[104], or nearly 7% the lifetime radiation exposure limit to a radiation worker[1]. A number of large scale epidemiologic studies suggest an increased risk of long term cardiac mortality after radiation exposure[37,105]. In one study looking at long term cardiac mortality following breast cancer radiation, major differences in mortality took 15 years to emerge[105]. This time course was replicated across a number of different studies[106]. However, a major limitation of these studies is the inability to isolate changes related to endothelial response to radiation vs primary cardiomyocyte damage[70]. Another major confounder is secondary cardiac damage to the elevated inflammatory state associated with radiation exposure[107]. Evidence from cell and animal literature suggest that IR can affect cells of the heart via apoptosis, inflammation, and oxidative stress, but much of that data is in the setting of high or lethal doses of radiation[108].

In this part of the dissertation, we investigate the early changes in the proteome after cardiomyocyte radiation exposure to better understand cellular processes that are affected[109]. Furthermore, we use a novel cardiac patch microphysiological system (MPS)

to investigate the functional derangement of cardiomyocyte early after radiation exposure.

3.2 Methods

3.2.1 Neonatal Ventricular Rat Cardiomyocyte (NVRCM) isolation

These experiments were approved by Duke University Medical Center IACUC. NVRCMs were isolated from ventricles of 2-day-old Sprague-Dawley rats (Charles River Laboratories) as previously described[110]. In brief, ventricles were harvested, minced, and enzymatically dissociated using trypsin and collagenase. Cells were then suspended in DMEM/F-12 with 10% Fetal Bovine Serum and 10% Horse Serum, and pre-plated for 45 min at 37 °C to increase the fraction of cardiomyocytes in the cell suspension. Cells were cultured in 6-well plates at a density of 1.5x105 cells/cm^2 depending on the assay. The cells were maintained in culture for 2 days and were contractile prior to radiation exposure. Different isolations were performed for the different experiments (cell assays, proteomics, western blot, and building of cardiac patches). In total 6 different isolations were used for these studies.

3.2.2 Cardiac Patch Fabrication

Our cardiac patch fabrication protocol has been previously described[111,112]. In brief, polydimethysiloxane (PDMS, Dow Corning) tissue molds are created by curing the polymer in a custom PTFE template. A cell/hydrogel mixture is prepared with a final composition of 2 mg/mL fibrinogen, 1 U/mL thrombin, 10% matrigel, and 10 × 106

cells/mL[111]. Media is initially changed 24 hours after patch fabrication and every 48 hours thereafter. Engineered patches are cultured for 12–14 days prior to radiation exposure and functional assessment.

3.2.3 Cell and Patch Irradiation

Twenty-four hours before irradiation NRCMs and cardiac patches received fresh culture medium. They are irradiated at room temperature with a single dose of 0, 0.1, 0.3, 0.5 or 2 Gy, using a Mark I 68A Cs 137 irradiator for Gamma rays (JL Shepherd and Associates, San Fernando, CA) and an XRAD 360 for X-ray radiation. Average dose rate was 1.5Gy/minute. During the radiation exposure, they are placed on a plate rotator to insure equalized radiation delivery (for Gamma rays). After irradiation, they are returned to the incubator and maintained at 37 °C under 5% CO2 for 24 h. At 24 h, media samples are taken, some of the cells are pelleted, flash frozen in liquid nitrogen, and stored at -80C for proteomic analysis, while other cell/media samples were used for biochemical assays. Cells were scrapped off gently. This same experiment was repeated for western blot analysis, where lysis buffer (RIPA) was added to the cells for 30min. The cardiac patches underwent force testing and after which they were flash frozen for immunostaining.

3.2.4 Optical Mapping of Membrane Potentials and Intracellular Calcium For 2D Cells

Cells were stained with di-4 ANNEPS (5μM) for 5 min at room temperature for action potential measurements or Rhod2 AM for intracellular calcium imaging and

assayed using a hexagonal array of 504 optical fibers (RedShirt Imaging, Decatur, GA) with a spatial resolution of 750 μm. For optical mapping, cultures were incubated at room temperature with a voltage-sensitive dye (Di-4 ANEPPS, 16 μmol/L) for 5 min, transferred to a custom-made, thermo-regulated recording chamber, and illuminated by a light emitting diode (LED) light source (λ = 520 ± 30 nm). To limit cell phototoxicity, light exposure was synchronized with data acquisition and electrical stimulation using LabView (National Instruments, Austin, TX). Red fluorescence (λ > 590 nm) was collected by the fiber-optic array, converted to voltage by photodiodes, sampled at 1.2 kHz, and saved to a PC. Cells were stimulated using either field electrodes or custom-made platinum electrode for point stimulation.

3.2.5 Patch Electrical and Contractile Function

Cardiac patches underwent mechanical and electrical testing 24 h after radiation. Action potential propagation in the cardiac patch is measured using a voltage-sensitive membrane dye, as previously described[113–115]. Patches were stained with 10 μM di-4 ANEPPS, incubated in 37 °C Tyrode's solution with the excitation-contraction uncoupler blebbistatin (10 μM), and stimulated at the patch periphery by a platinum point electrode connected to a Grass SD9 stimulator. Optical signals are recorded by a photo diode array connected to 504 hexagonally arranged, 750 μm optical fibers. Data are acquired in 2–5 sec episodes after 10 sec of pre-pacing at a sampling rate of 1.2 kHz.

Cardiac patch contractile force is measured using a custom system consisting of a heated tissue bath (Cell MicroControls BD-42) maintained at 37 °C, a force transducer, and platinum field stimulus electrodes. Opposite edges of the patch frame are mounted to a force transducer and to a fixed PDMS block. Patches are then stimulated at a rate of 1 Hz in Tyrode's solution containing 1.8 mM Ca2+, and force data were acquired at a sampling rate of 1 kHz. The patches are stretched in increments of 3% up to 15% elongation using a 1-axis motorized stage (Thorlabs MT1-Z8), and active and passive force were measured at each tissue length.

3.2.6 Mass Spectrometry and Analysis

Immediately upon removal of the cells from -80C storage, 200 μL of 0.25% RapiGest (Waters Corp.) in 50 mM ammonium bicarbonate, pH8, was added to the bottom of each tube. This volume was pipetted up and down several times to break up the cell pellet, and then each sample was probe sonicated for 3 cycles of 5 second bursts at power level 3, cooling on ice between bursts. Tubes were then frozen at -80C for 10 minutes, removed from freezer and thawed on ice, and freeze/thaw cycle was repeated. Samples were centrifuged at 15,000 rpm for 5 minutes, and a very small white pellet was visible at the bottom of each epi tube. Sample concentrations were determined by mini-Bradford assay (BioRad, Inc.) against a bovine serum albumin (BSA) calibration curve. 25 μg from each sample was removed (volumes based on concentration) and added to new 1.5 mL epi tubes. Then 0.25% RapiGest was added to each sample to bring the

volume to 17.4 μL. Samples were then digested according to an in-solution tryptic digestion protocol. Mass spectrometry grade porcine trypsin gold was added at 1:50 enzyme: protein ratio and samples were incubated at 37C overnight while shaking. Following overnight digestion, RapiGest surfactant was hydrolyzed by addition of 1% TFA/2% ACN final. All samples were also spiked with ADH1_YEAST digest (Massprep standard, Waters Corp.) as a surrogate standard (50 fmol ADH per ug total protein). All samples were heated at 60C for 2 h and centrifuged at 15,000 rpm for 5 min before pipetting all supernatant into individual TotalRecovery LC vials (Waters, Corp.). 5 μL was pipetted from each and combined to make a pool for QC purposes. 1 μg from the pooled sample was injected before each replicate group queue and was also injected once at the end of the queue for a total of five pooled analyses. One of the five pooled analyses was run in data-dependent acquisition mode (DDA) for complementary peptide identifications whereas the others were performed as detailed below.

Quantitative LC/MS/MS was performed on 1 μg of protein digest per sample, using a nanoAcquity UPLC system (Waters Corp) coupled to a Synapt G2 HDMS high resolution accurate mass tandem mass spectrometer (Waters Corp.) via a nanoelectrospray ionization source. Briefly, the sample was first trapped on a Symmetry C18 300 mm × 180 mm trapping column (5 μl/min at 99.9/0.1 v/v water/acetonitrile), after which the analytical separation was performed using a 1.7 um Acquity BEH130 C18 75 mm × 250 mm column (Waters Corp.) using a 90-min gradient of 5 to 40%

acetonitrile with 0.1% formic acid at a flow rate of 400 nanoliters/minute (nL/min) with a column temperature of 55C. Data collection on the Synapt G2 mass spectrometer was performed in ion-mobility assisted data-independent acquisition (HDDIA or HDMSE) mode, using 0.6 second alternating cycle time between low (6V) and high (27-50V) collision energy (CE). Scans performed at low CE measure peptide accurate mass and intensity (abundance), while scans at elevated CE allow for qualitative identification of the resulting peptide fragments via database searching. The total analysis cycle time for each sample injection was approximately 2.25 h.

Data was imported into Rosetta Elucidator v3.3 (Rosetta Biosoftware, Inc), and all LC-MS files were aligned based on the accurate mass and retention time of detected ions ("features") using PeakTeller algorithm (Elucidator). The relative peptide abundance was calculated based on area-under-the-curve (AUC) of aligned features across all runs. The dataset had 328,028 quantified features and 17,518 annotated spectra. This MS/MS data was searched against a NCBI RefSeq database with rattus norvegicus taxonomy (25,485 forward entries) appended with a decoy reverse-sequence of each forward entry for false positive rate determination. The sequences for ADH_yeast, CASA1_bovin, and CASA2_bovin were also appended to the database representing internal standards used. The following dynamic mass modifications were allowed with up to 2 missed cleavages - carbamidomethylation (from alkylation protocol) on Cys residues, oxidation on Met and Cys residues, dioxidation on Cys

residues, trioxidation on Cys residues, and deamidation on Asn and Gln residues. After individual peptide scoring using PeptideProphet algorithm (Elucidator), the data was annotated at a 0.9% peptide false discovery rate. The final quantitative dataset was based on 4,269 peptides and contains 813 proteins.

3.2.7 Bioinformatics analysis

Bioinformatics analysis was performed by Yared Kidane. Outliers were screened using a Principal Component Analysis to identify the top three principal components. Components were based on z-scored transformed summed protein intensities. Analytical reproducibility during this study was assessed by measuring the average variation of all protein intensities (n=813) within the QC pool treatment group (n=4 analyses). Global expression profiles and quantitative trending within the samples was measured by a two-dimensional agglomerative clustering of protein expression levels. To look at dose response, fold-changes were calculated from the average protein expression values between the zero-dose group and each of the other doses. A T-test was also performed (without multiple hypothesis correction) for these same comparisons.

3.2.8 Structural Characterization and Immunofluorescence of Radiated Patches

Immunofluorescent analysis was performed after 24 hr post radiation exposure. Briefly, cardiac patches were washed with Ca^{2+} free PBS and fixed with cold 4% paraformaldehyde (EMS) for 15min on a rocker. Tissues were blocked and

permeabilized in 3D block solution (PBS, 0.5% Triton-X100, 5% chicken serum) overnight at 4ºC, and incubated with primary antibodies (1/250-1/500) overnight at 4ºC. After washing, tissues were incubated with species-appropriate AlexaFluor (Invitrogen) secondary antibodies (1:1000 dilution) overnight at 4ºC. Tissues were mounted on microscope slides in Fluoromount-G (EMS), covered with a cover glass and sealed with nail polish for long-term preservation of fluorescence. Images were taken on a Leica SP5 inverted confocal microscope and post-processed with ImageJ.

3.2.9 Western Blot

To confirm some of the proteomics data analysis, a literature and an antibody search was conducted to help identify pathways or proteins identified as significant and their expression level in radiated myocytes. Two proteins were chosen that met the criteria of having a relevant pathway of interest as well as well validated antibody for detection. New radiation experiments were conducted as per above. The cell pellets were thawed out in lysis buffer. The cells were homogenized and spun down using a microcentrifuge for 20 minutes at 12,000 RPM at 4C. The supernatant was aspirated and maintained on ice. A small sample of the supernatant was used to perform a protein quantification assay. The samples were run on an 8-12% Gel, 100V. After transfer to a nitrocellulose membrane, the membrane was blocked with milk-based blocking buffer. Next, samples were incubated with the primary antibody for AIF (Abcam ab1998) (0.5ug/ml dilution) overnight at 4C. The membrane was washed, and re-exposed to

secondary antibody (1/3000 dilution for 1 h at room temperature). After additional washing, the membrane was exposed to film (exposure time 1 second). Band intensity was analyzed using ImageJ.

3.2.10 Oxidative Stress Indices

H_2O_2 production was analyzed using the culture media and examined by ROS-GloTM Assay (Promega) using a Turner Biosystems Veritas luminometer (Sunnyvale, CA). Mitochondrial ROS production was assessed using MitoTracker Red CMXRos (Molecular Probes, Eugene, OR). CMXRos was delivered at 100 nM and assayed at 579/599 nm using a FLUOstar OPTIMA fluorometric plate reader (BMG LABTECH, Cary, NC). GSH-to-GSSG levels were analyzed using the GSH/GSSG-GloTM Assay (Promega).

3.2.11 Cell Damage Assays

LDH in culture media was detected using the CytoTox-ONETM Homogenous Membrane Integrity Assay (Promega) on a fluorometric plate reader. Glutathione S-Transferases (GST) in culture media was analyzed by an assay by Promega (Madison, WI) using luminometry. Caspase-3 activity was performed on cell lysates as previously described[110].

3.2.12 Statistical analyses

For the cardiac patch analysis one-way ANOVA followed by Dunnett's multiple comparisons test was performed. For the 2D experiments and given the small sample

size, Kruskal-Wallis test with Dunn's multiple comparisons was used in GraphPad Prism version 8.0. Western blot analysis was performed using ImageJ, and band intensity statistics run using GraphPad nonparametric testing. Three independent experiments were performed for each assay. Significance was considered at $p \leq 0.05$.

3.3 Results

3.3.1. Experimental design

The overall experimental design can be seen in Figure 19. For all experiments, neonatal rat ventricular cardiomyocytes (NRVMs) were isolated from variable number litters in a total of 6 different isolations per the methods described above. They were maintained in culture prior to the below experiments.

Cells and media are processed 24 h post radiation (Figure 19A) and underwent quantitative LC/MS/MS yielding 4,269 unique peptides per sample (Figure 19B). For the proteomics experiments, 3 independent samples were used per radiation group (control, 0.1 Gy, 0.3 Gy, and 0.5 Gy). These were all from the same cell NRVCM isolation. Other experiments including western blotting (n= 2 independent radiations, 1 control), cardiac patch generation (n=4-8 patches per group) used different isolations, but the same protocol.

For the proteomics analysis, by filtering to 2 matching peptides per protein, 457 proteins were identified. The unique protein data set then underwent a number of data quality checks and clustering to identify any batch effects, a differential expression

analysis based on the treatment group, and a number of additional analyses including protein pathway analysis and interaction analysis (Figure 19B). Similarly, the cardiac patches were studied 24 hr after radiation, and media samples were collected for biochemical analysis. They underwent functional testing and were then fixed for staining (Figure 19C).

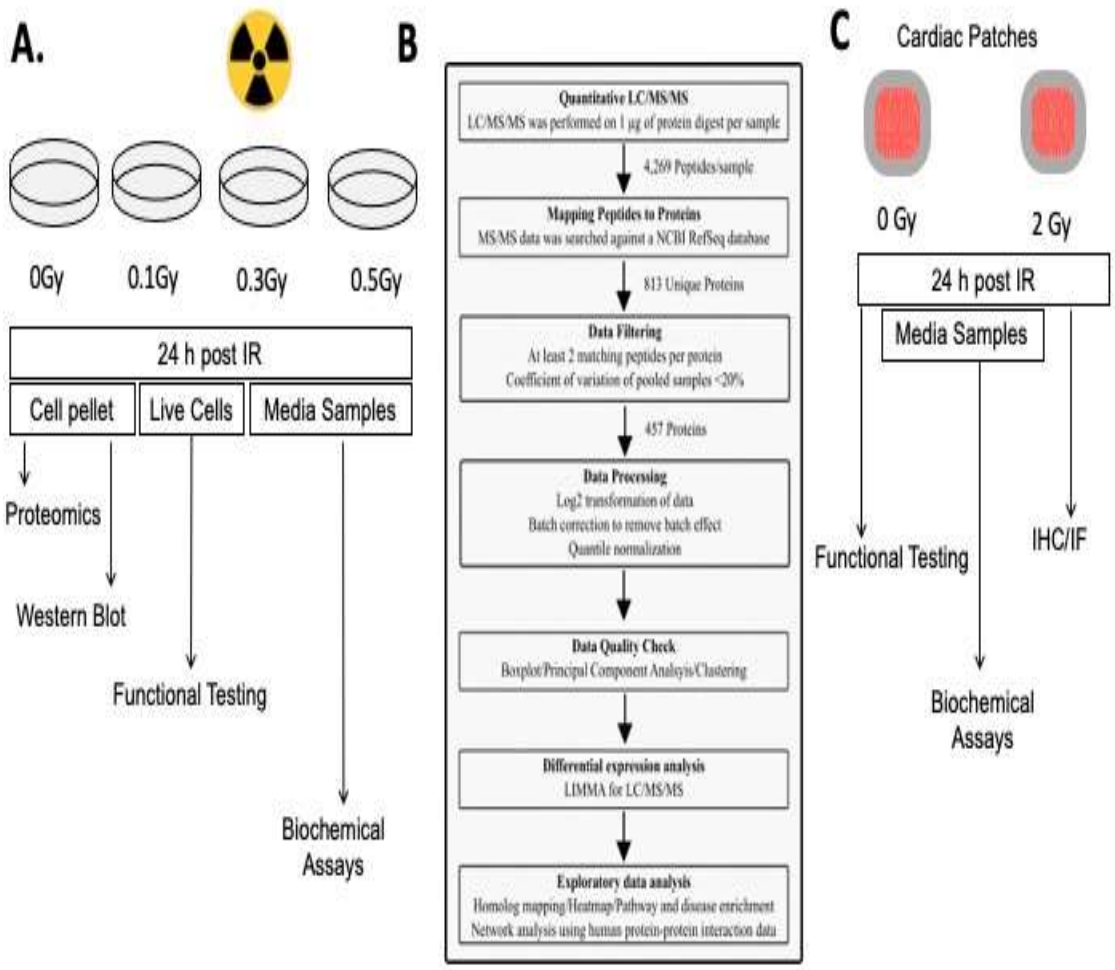

Figure 19: 2D and cardiac patch radiation experimental design. Rat neonatal cardiomyocytes were isolated and cultured. They were radiated with different doses of gamma rays (A). The cells and media were assessed 24 h after, as well as the cells sent for proteomics analysis (B). Finally, cells were used to generate cardiac patches, that were radiated using 2Gy of x-rays and assessed for mechanical and electrical function.

The protein yield of all the different replicates was adequate to proceed with the proteomics analysis as can be seen in the table below, minimum level needed for these specific experiments is 100-150ug.

Table 3: Protein yield for proteomics analysis from radiated cardiomyocytes

Proteomics ID	Sample Name	Run Order	[c] (mg/mL)	Protein Yield (ug)
ID12298	0 #1	2	1.44	288
ID12299	0 #2	7	1.53	306
ID12300	0 #3	12	3.33	666
ID12301	0.1 #1	3	1.91	382
ID12302	0.1 #2	8	1.58	316
ID12303	0.1 #3	13	1.66	332
ID12304	0.3 #1	4	2.01	402
ID12305	0.3 #2	9	2.06	412
ID12306	0.3 #3	14	4.87	974
ID12307	0.5 #1	5	2.51	502
ID12308	0.5 #2	10	2.35	470
ID12309	0.5 #3	15	1.88	376
ID12341	pool	1, 6, 11, 16	n/a	n/a

3.3.2. Effect of radiation on 2D NRVMs and rat cardiac patch forces

2D irradiated cells demonstrated a statistically significant decline in action potential duration (APD) as compared to controls for the 0.5 Gy dose (Figure 20A, p=0.02). Furthermore, cells that underwent 0.5 Gy of radiation had an important decrease in Ca transit duration as compared to controls (Figure 20B, p=0.01). However, this was not associated with any changes in conduction velocities (CV) (Figure 20C). Furthermore, maximum capture rate can be also compared by pacing the cells at increasing frequencies and determining the highest frequency where they continue to pace. There appeared to be a trend of an increase in the maximum capture rate for 0.5

Gy radiated cells as compared to controls (p=0.09) (Figure 20D). (n=3 wells per group, 3 independent samples per group, non-parametric Kruskal-Wallis test with Dunn's multiple comparisons test. Bar graph mean ± SEM).

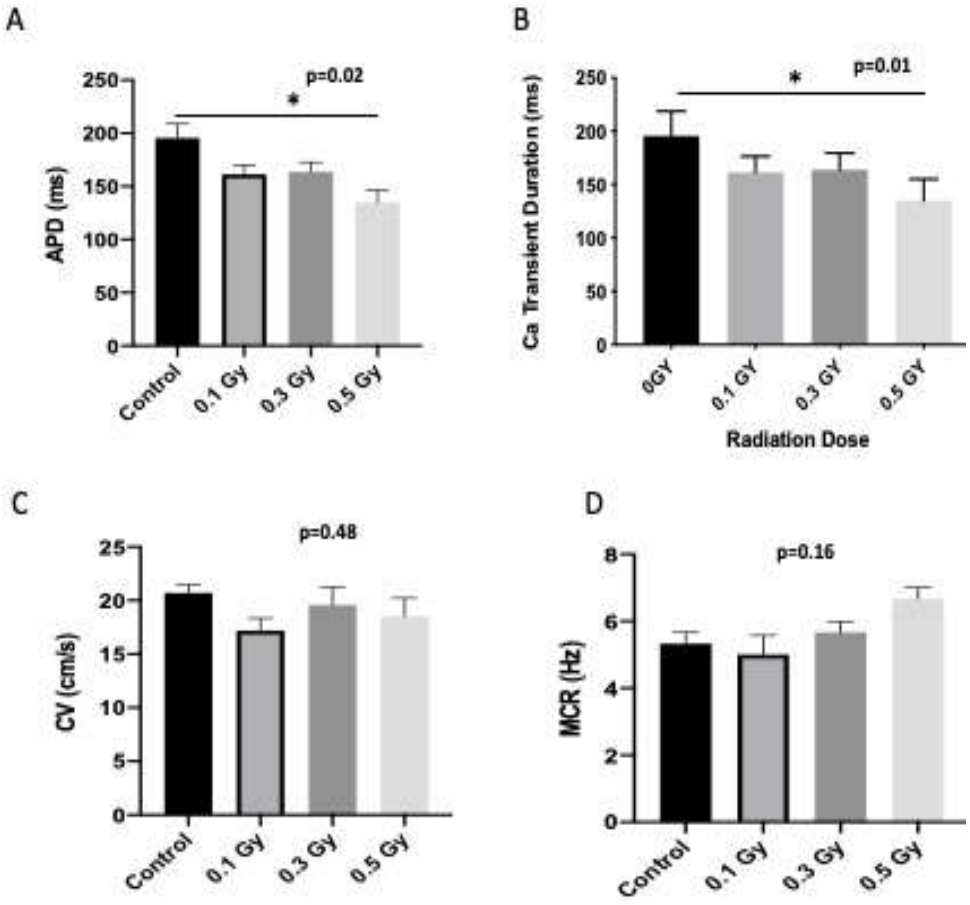

Figure 20: Changes in 2D cardiomyocyte properties following IR.Cardiomyocytes radiated with 0.5Gy had a significant drop in action potential duration and Ca transit, with no changes in capture rate or conduction velocity.

Using the cardiac patch system, at 24 hours, we noted important changes including (a) a trend towards a decrease in Maximum Active Forces (Figure 21A), a trend showing a decrease in Conduction Velocity (Figure 21B), and no change in Action Potential Duration (APD), (Figure 21C, p=0.54). (n=7-8 patches per group, Mann-Whitney test, Bar graph mean ± SEM).

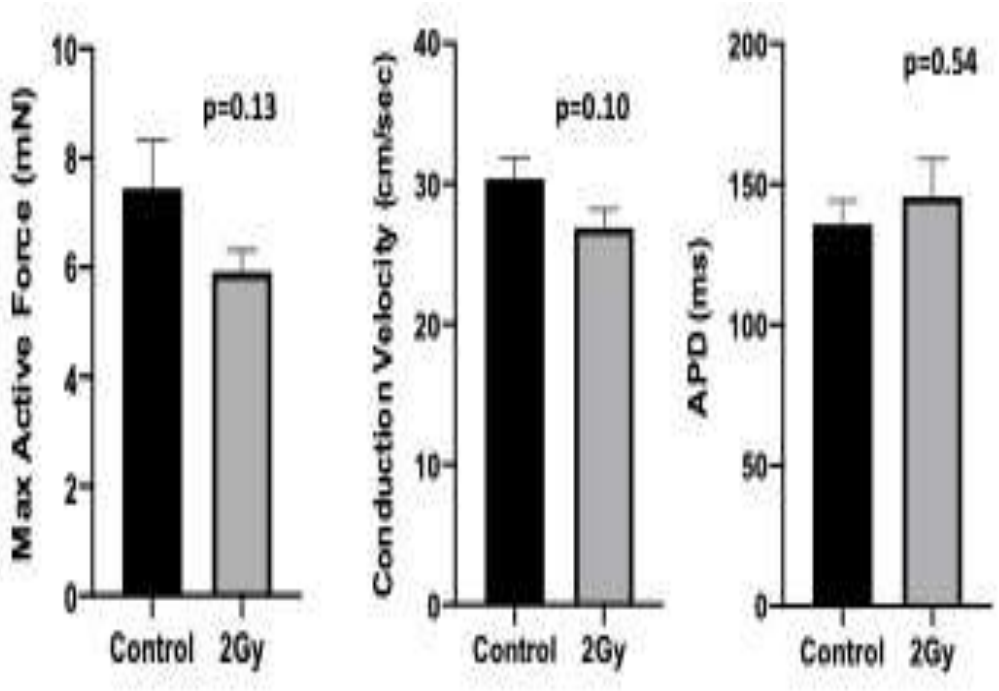

Figure 21: Changes in cardiac patch properties following IR. There was a trend of a decrease in active force and conduction velocity 24hrs after radiation compared to controls. There was no change in action potential duration.

To further investigate changes in patch mechanical properties, we generated force length curves for the different patches in the treatment groups. As can be seen, these patches display the expected force-length relationship of cardiac tissue[116]. Furthermore, we added a 3rd group with a much higher radiation does (10 Gy) in an effort to demonstrate an extreme effect. Interestingly, and as can be seen in the Figure 22, 24 hr post radiation, while the radiated patches on average had lower active forces at different stretch degrees than controls, there appeared to be little to no differences in those undergoing 2Gy vs 10 Gy of radiation. (Figure 22, n=4 patches per group). The

different color lines represent different patches. One patch in the control group (blue) had much higher active forces than the rest of the group.

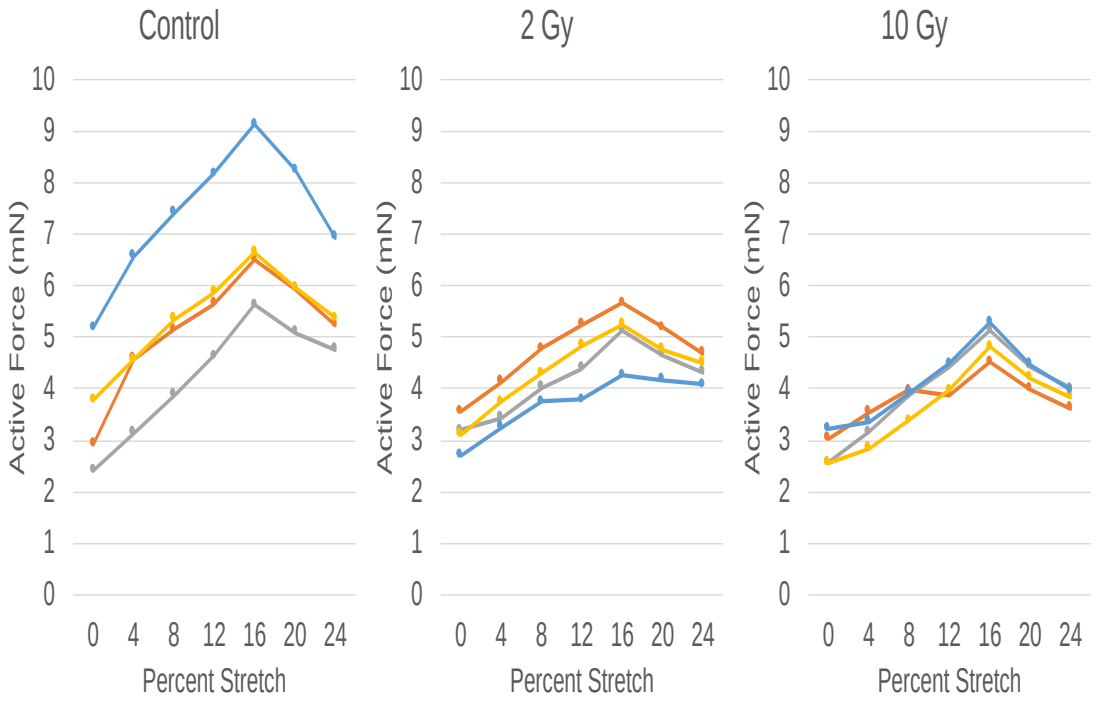

Figure 22: Changes in cardiac patch force length curve after radiation evaluated 24 h after radiation

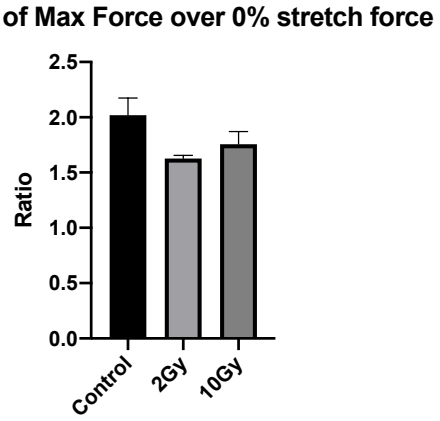

Figure 23: Ratio of max force over force at 0% stretch for cardiac patches radiated with 2Gy or 10 Gy gamma rays compared to controls.

Another method to evaluate the changes to the max force, is to index it to the baseline force, or the force at no stretch. As can be seen in Figure 23, there is a slight decrease in this ratio for the radiated patches, however, that decline did not reach statistical significance (p=0.09).

Similar to the force length curves, when we evaluated the force frequency relationship for control patches vs 2Gy and 10 Gy radiated patches, there was a drop in the active force across frequencies studied, with little to no difference observed for the 2 Gy radiated patches as compared to the 10 Gy radiated patches. (Figure 24, n= 4 patches per group). It is important to note, that this patch model does not show the expected positive slope for the force frequency relationship. This is mainly a limitation of the patch model that has been previously reported[114].

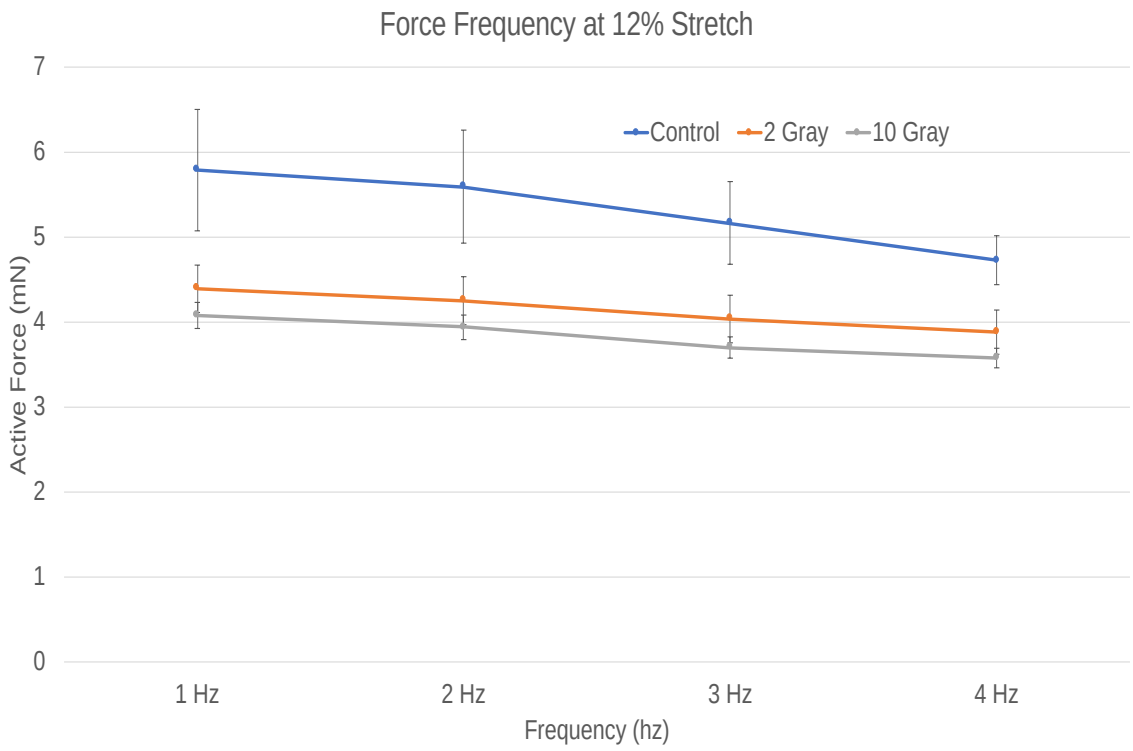

Figure 24: Force frequency relationship for radiated cardiac patches 24 h post radiation.

Electrical mapping of these patches did not display any differences other than what was previously reported in the average APD and CVs. Representative images of the cardiac patch mapping, showing activation time is shown in Figure 25. These are

quantified as part of the conduction velocity analysis from before.

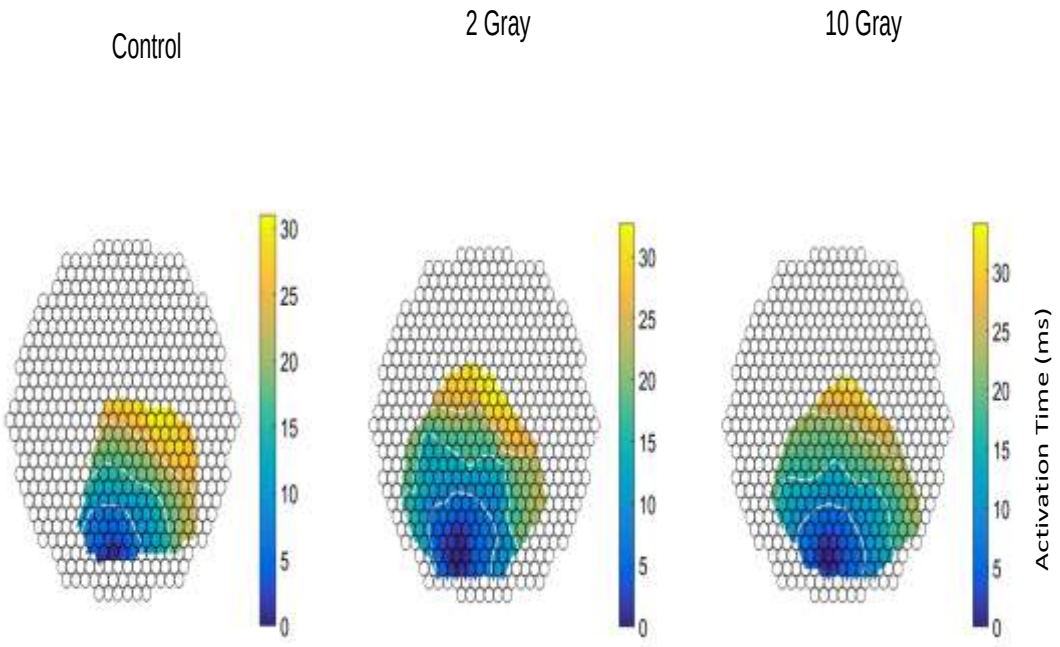

Figure 25: Cardiac patch mapping and changes in activation time 24 h after radiation of 3 representative 2Gy radiated patches.

Finally, the patches were evaluated for any early (24 h) structural changes after 2 Gy exposure. Staining the patches for markers of cellular structure, injury and organization did not reveal differences between the radiated and control patches. Cardiac patches are stained for sarcomeric a-actinin (SAA), Vimentin (Vim), NKX2.5 (marker of immature cardiomyocyte with potential for division), Ki67, and F-actin. No expression of NKX2.5 or Ki67 is seen. This was primarily looked at given some reports that low dose radiation can actually induce cell proliferation in certain cell types[117].

Structural markers did not display any specific changes in patch structure between the control and radiated patches, and similar overall densities (DAPI).

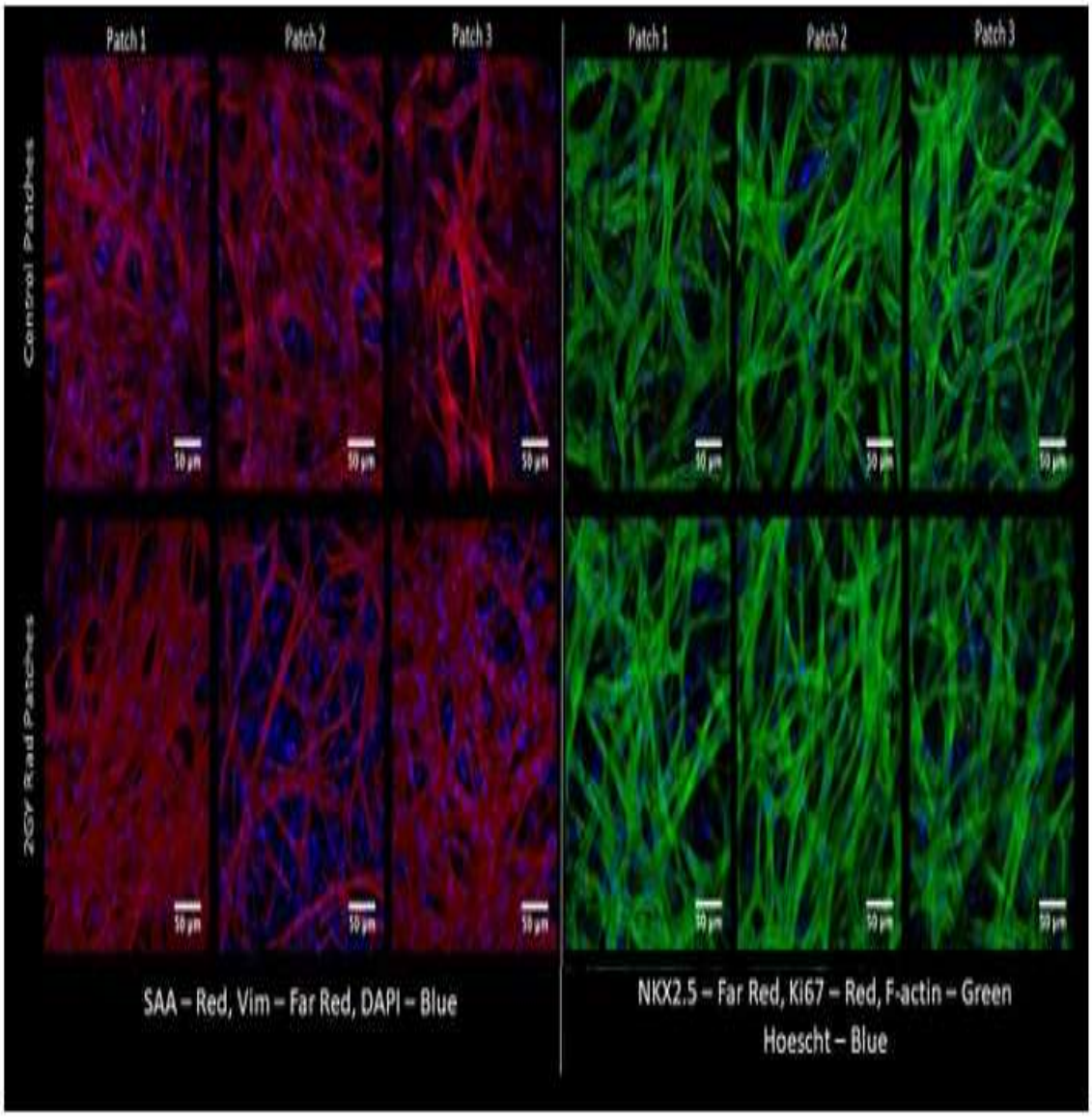

Figure 26: Cardiac patch immunofluorescence studies post radiation. Pathes were fixed and imaged 24 h after exposure to 2Gy of radiation (bottom panel) compared to controls, (top panel)

3.3.3. Enhancement of oxidative stress following IR

2D radiated cells were analyzed for indicators of oxidative stress and cellular damage 24 h post-irradiation. While there was no difference in LDH release ($p = 0.44$;

Figure 27A), GST ($p = 0.10$; Figure 27B) and Caspase 3 activity ($p = 0.744$; Figure 27C), above baseline levels for the control conditions, cardiomyocytes had significantly higher ROS production, compared to control cells at all the studied doses ($p < 0.05$; Figure 27D). There was also no difference in GSH/GSSG ratio (Figure 27E)., (n=3 independent samples per group). Units are arbitrary and represent relative change from the control samples (set to 1)

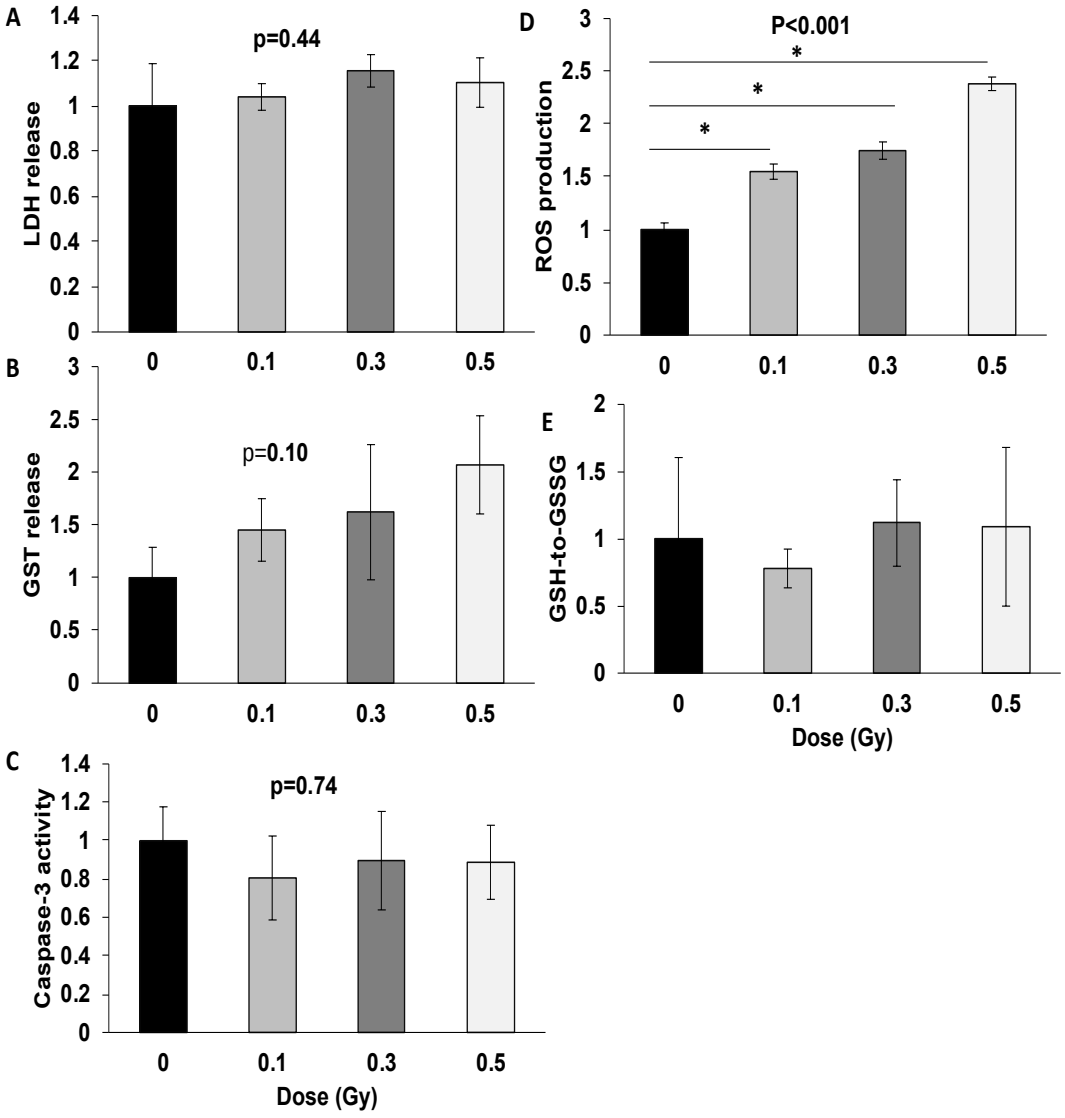

Figure 27: Markers of cell death and oxidative stress after radiation. 24 h after radiation, media from cardiomyocytes radiated with different doses of gamma rays.

3.3.4. Proteomics analysis of radiated cardiomyocytes

Analytical reproducibility during this study was assessed by measuring the average variation of all protein intensities (n=813) within the quality control (QC) pool treatment group (n=4 analyses), as has been previously recommended[118]. Average percent coefficient of variation (%CV) in the QC pool was 13.8% with a median of 10.8% across all proteins, as shown in the tables below. For proteins quantified by 2 or more peptides (n=478), the average CV was 9.9% and median was 8.8%. The average %CVs across all other samples, reflecting biological variability (or variability in cardiomyocyte isolation/protein extraction steps), were 29% for all proteins, and 22% for proteins

uantified by 2+ peptides.

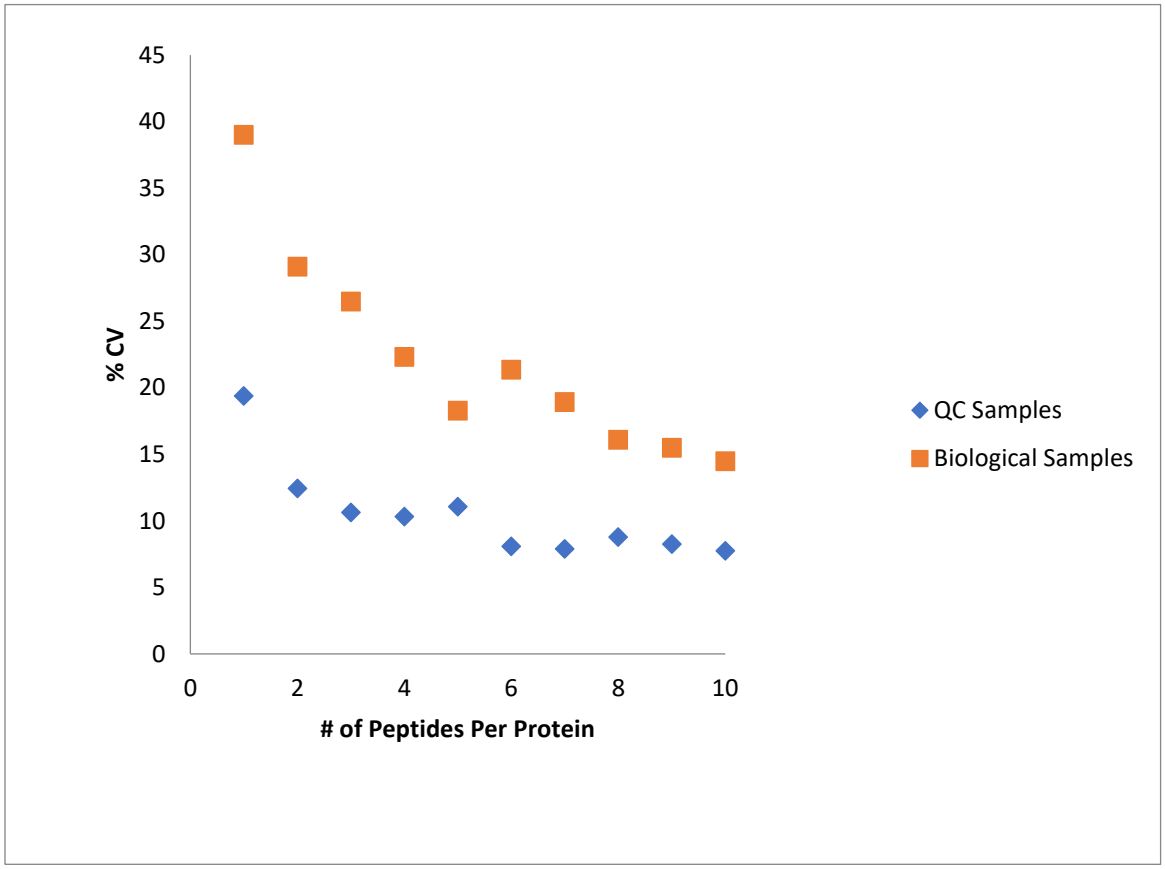

Figure 28: Coefficient of variation as a function of number of quantified peptides as a quality check for cardiomyocytes 24 h after radiation

We also examined the quantitative precision as a function of number of quantified peptides per protein. In the QC pool, there was an improvement in %CV between proteins quantified by one versus two peptides per protein, but the average CVs of "single-hit" proteins were still only 19%. The analytical variability leveled out at around

10% CV with 3 or more peptides. As expected, the individual biological samples showed a higher variance than the technical variance (n=3 for each of the radiation doses), usually by a margin of about 2x. For instance, with proteins containing 2 peptides the average biological %CV is nearly 30%, while this value is below 15% for technical %CV. The measured biological variability in protein quantity shows continual slow decline as the number of peptides to the protein increases from 1 to 10 (or more).

Of the total 813 proteins examined, 87 were found to have differential expression between the radiated cardiomyocytes compared to controls (Figure 29). Evaluating the proteome reveals that a number of different proteins are differentially upregulated or down regulated with different radiation doses (n= 3 independent exposure for each

condition) (Figure 28).

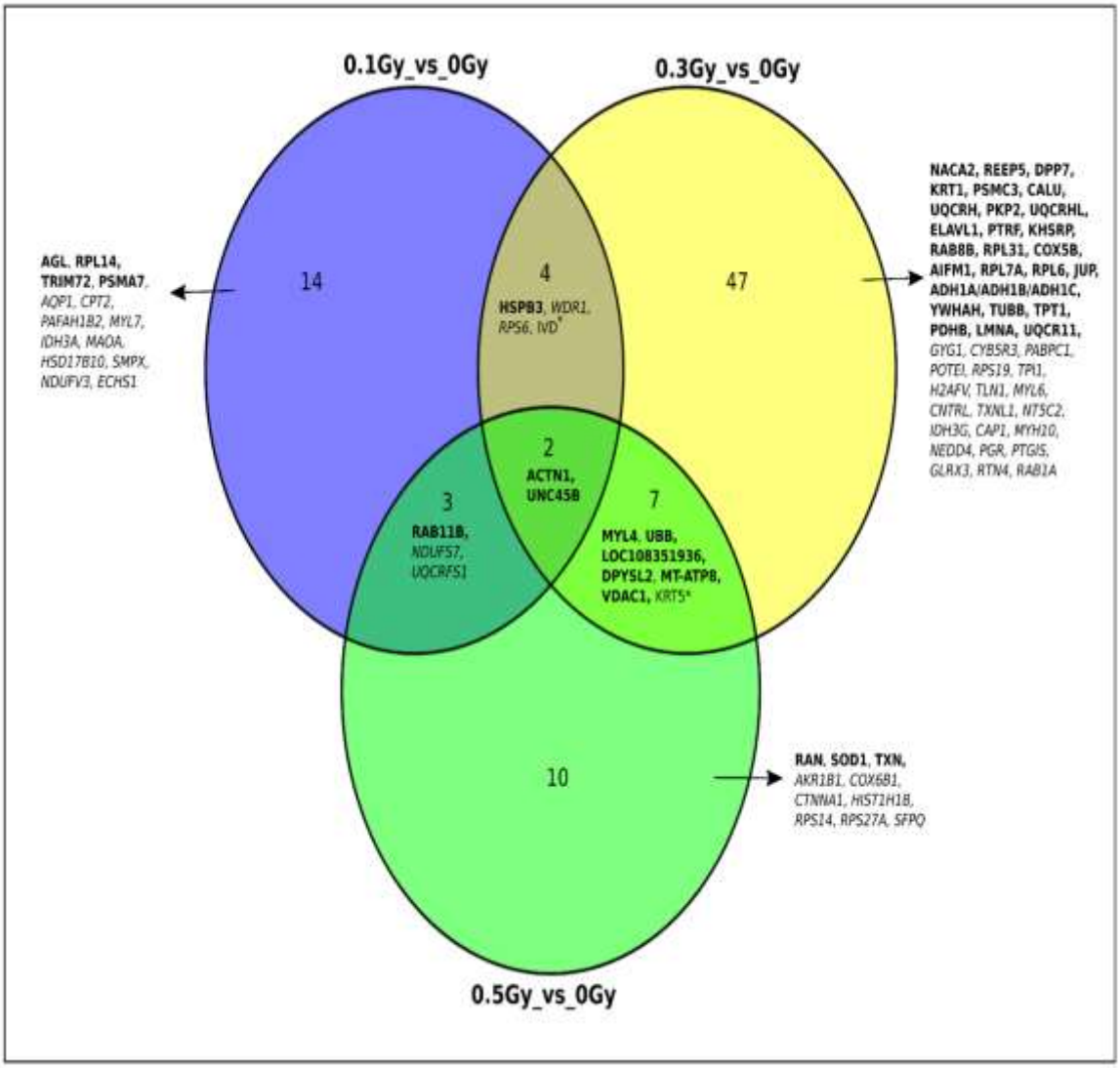

Figure 29: Changes in protein expression compared to controls for the different doses of gamma rays 24 h after cardiomyocyte radiation

Gene names that are bolded represent those that have an upregulation as compared to controls (p values are found in the tables below). The non bolded names are those that are found to be downregulated. Compared to control, 0.1 Gy of radiation was associated with significant changes in 23 proteins, 0.3 Gy associated with changes in 60 proteins, and 0.5 Gy with 22 proteins. The roles of the overlapping proteins can be seen in the network diagram below.

A PCA analysis (Figure 30) for the studied samples was then performed. The PCA shows significant differences for the control cells, and better clustering of the 0.3Gy radiated cells.

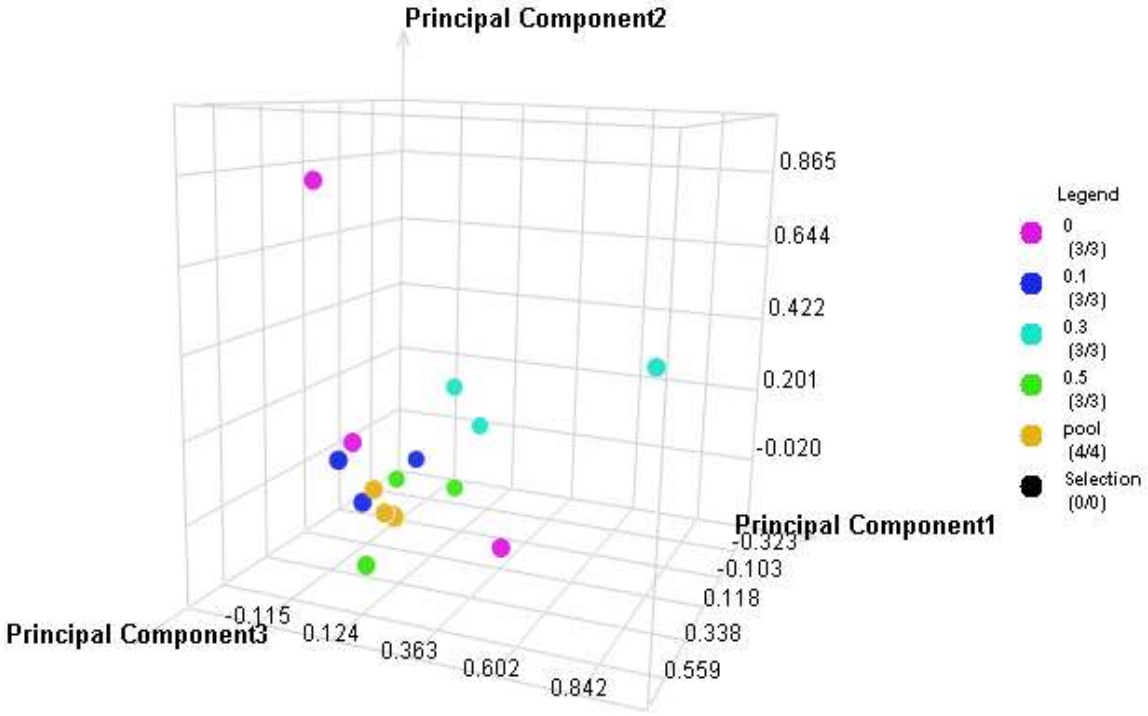

Figure 30: PCA analysis of the proteomics samples from cardiomycoytes radiated with different doses of gamma rays

It was unclear why such difference existed since the cells came from the same animal isolation as discussed above. This batch effect might be due to biological variability that can exist, or methodological issues related to sample handling and preparation. One important point to note about the PCA, is the technical replicates, which are the pooled samples from all the groups, are grouping more tightly together, suggesting biological variance is much higher than technical variance. No outliers can be

removed even if they were detected, due to the current limitation on only n=3 biological replicates.

Using the gene ontology framework[119,120], many of these proteins found to be differentially regulated after radiation exposure in cardiomyocytes are associated with mitochondrial function and dysfunction displayed using a REVIGO[119] blot (Figure 31). In this type of chart, different cellular processes revealed during the proteomics analysis are displayed using bubbles. A significant number of mitochondrial related proteins were found to have differences in regulation after radiation exposure. Bubble size represents the frequency of the gene ontology term, and the color represent the "p value". The bubbles' x and y coordinates are derived by applying multidimensional scaling to a matrix of the ontology terms' semantic similarities. This is the reason why different bubbles representing mitochondrial process are displayed in more close proximity.

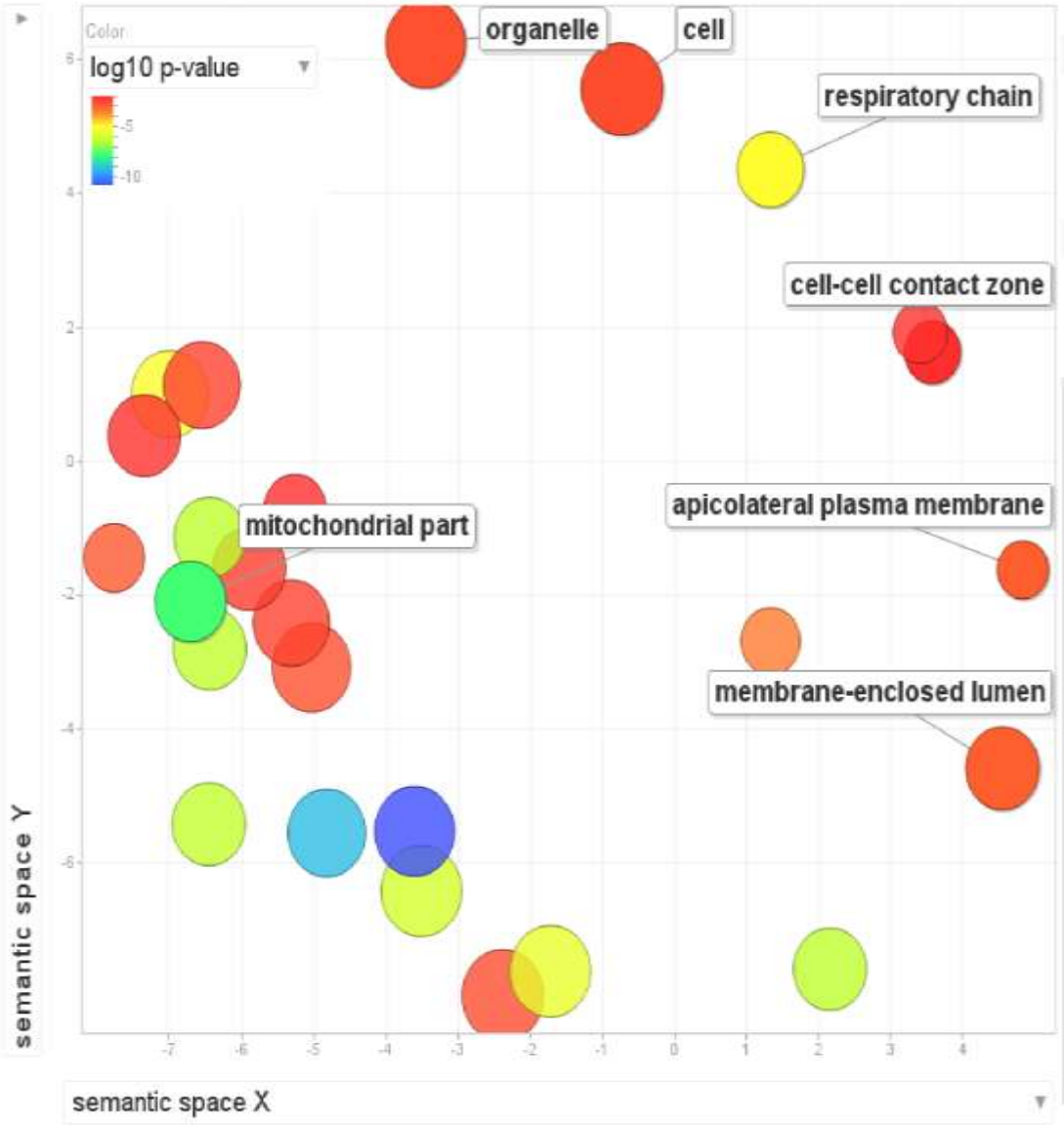

Figure 31: REVIGO blot of cellular elements involved post radiation demonstrating large involvement of mitochondrial pathways

The overall proteomic signature appears to be different for the different doses, and involvement of a number of other cellular pathways (Figure 32). A full list of the protein changes and fold change is provided in the Table below.

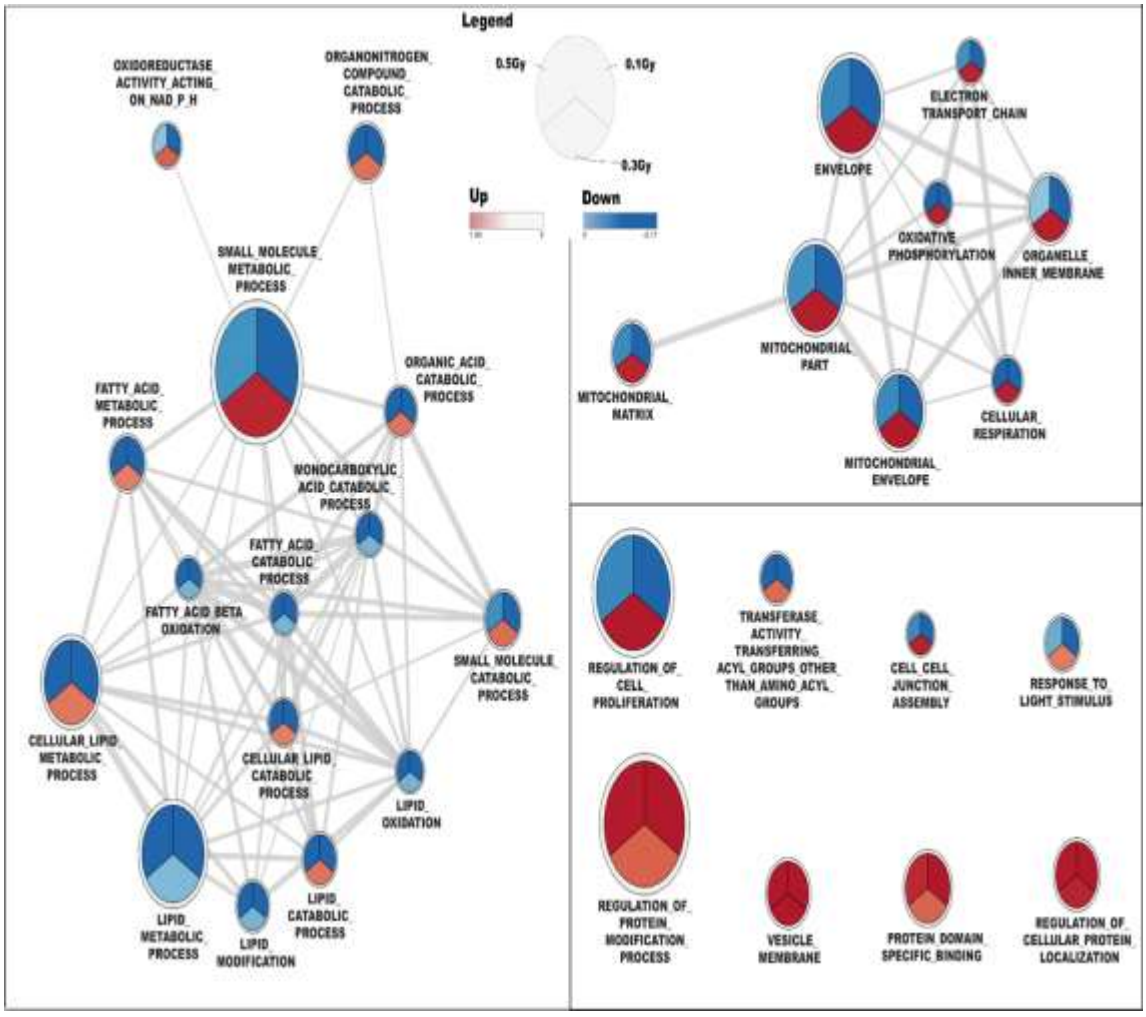

Figure 32: Changes in the proteomic signature 24 h following different doses of radiation exposure of cardiomyocytes

Figure 32 shows the different cellular pathways that are significantly altered after the different radiation doses. Of note, the 0.3 Gy radiated cardiomyocytes appeared to behave differently than the other 2 doses. They had down regulation in a number of different pathways that had upregulation by the other two doses. This finding will require further study and validation.

Table 4: Significantly perturbed KEGG and WIKI pathways for radiated Cardiomyocytes

PathwayName	#Gene	EntrezGene	Adj Pval
KEGG			
Metabolic pathways	21	26196 24513 25179 29253 24172 688869 114096 29539 690848 24192 362029 291103 100363253 362837 94194 25527 63864 366448 64539 64189 289950	4.96E-14
Parkinson's disease	10	26196 83529 192255 94194 362837 688869 690848 366448 64539 291103	7.55E-12
Huntington's disease	9	26196 83529 94194 362837 688869 690848 366448 64539 291103	1.89E-09
Alzheimer's disease	9	26196 94194 362837 63864 688869 690848 366448 64539 291103	1.89E-09
Oxidative phosphorylation	8	26196 94194 362837 688869 690848 64539 366448 291103	2.81E-09
Cardiac muscle contraction	5	688869 690848 366448 94194 291103	2.16E-06
Arrhythmogenic right ventricular cardiomyopathy (ARVC)	4	60374 287925 81679 81634	3.64E-05
Citrate cycle (TCA cycle)	3	114096 25179 289950	8.02E-05
Pyruvate metabolism	3	29539 24192 289950	0.0002
Fatty acid metabolism	3	29539 25413 24172	0.0002
Valine, leucine and isoleucine degradation	3	63864 24513 29539	0.0003
Glycolysis / Gluconeogenesis	3	29539 24172 289950	0.0009
Histidine metabolism	2	29539 29253	0.0022
Pentose and glucuronate interconversions	2	29539 24192	0.0028
Ribosome	3	296596 117042 64298	0.0028
Tight junction	3	81634 289759 79433	0.003
Tyrosine metabolism	2	29253 24172	0.003
Tryptophan metabolism	2	29539 29253	0.005
Glycerolipid metabolism	2	29539 24192	0.0052
Proteasome	2	29677 29674	0.0052
Arginine and proline metabolism	2	29539 29253	0.0057
Focal adhesion	3	81634 289759 313494	0.0062
Regulation of actin cytoskeleton	3	81634 289759 79433	0.008
Drug metabolism - cytochrome P450	2	29253 24172	0.0119
Leukocyte transendothelial migration	2	81634 289759	0.0204
Oocyte meiosis	2	25154 25576	0.0204
Systemic lupus erythematosus	2	81634 685909	0.0253
WIKI PATHWAYS			
Electron Transport Chain	7	26196 690848 366448 64539 362837 94194 291103	9.37E-09
Proteasome Degradation	4	29677 192255 25489 29674	2.81E-05
TCA Cycle	3	114096 25179 289950	8.02E-05
Fatty Acid Omega Oxidation	2	29539 24172	0.0003
Cytoplasmic Ribosomal Proteins	3	296596 117042 64298	0.0013
Glycogen Metabolism	2	362029 81675	0.0041
Oxidative phosphorylation	2	64539 362837	0.0095
TNF-alpha NF-kB Signaling Pathway	3	29677 117042 25576	0.0101
Tryptophan metabolism	2	63864 29539	0.0108
Androgen Receptor Signaling Pathway	2	94194 25576	0.0274
Adipogenesis	2	60374 25527	0.0277
Regulation of Actin Cytoskeleton	2	81634 79433	0.0339
Insulin Signaling	2	64185 81675	0.0339

We then looked specifically at the altered proteins for the different radiation doses.

Table 5: Altered proteins in cardiomyocytes after 0.1 Gy radiation

Symbol	Direction	FC	pvalue	Human Description
MYL7	↓	1.63	0.04	myosin light chain 7
AQP1	↓	1.53	0.01	aquaporin 1 (Colton blood group)
CPT2	↓	1.47	0.01	carnitine palmitoyltransferase 2
RPL14	↑	1.43	0.10	ribosomal protein L14
IVD	↓	1.42	0.06	isovaleryl-CoA dehydrogenase
ECHS1	↓	1.39	0.07	enoyl-CoA hydratase, short chain 1
RAB11B	↑	1.36	0.00	RAB11B, member RAS oncogene family
UQCRFS1	↓	1.35	0.15	ubiquinol-cytochrome c reductase,
PAFAH1B2	↓	1.34	0.02	platelet activating factor acetylhydrolase
PSMA7	↑	1.34	0.12	proteasome subunit alpha 7
UNC45B	↑	1.33	0.05	unc-45 myosin chaperone B
WDR1	↓	1.29	0.12	WD repeat domain 1
SMPX	↓	1.28	0.04	small muscle protein, X-linked
NDUFV3	↓	1.27	0.07	NADH:ubiquinone oxidoreductase subunit V3
HSD17B10	↓	1.25	0.03	hydroxysteroid 17-beta dehydrogenase 10
MAOA	↓	1.24	0.01	monoamine oxidase A
AGL	↑	1.24	0.06	amylo-alpha-1, 6-glucosidase, 4-alpha-glucanotransferase
IDH3A	↓	1.24	0.00	isocitrate dehydrogenase 3 (NAD(+)) alpha
HSPB3	↑	1.24	0.00	heat shock protein family B (small) member 3

TRIM72	↑	1.23	0.10	tripartite motif containing 72
NDUFS7	↓	1.23	0.10	NADH:ubiquinone oxidoreductase core subunit S7
ACTN1	↑	1.21	0.05	actinin alpha 1

Table 6: Altered proteins in cardiomyocytes after 0.3 Gy radiation

Symbol	**Direction**	**FC**	**Pvalue**	**Human Description**
H2AFV	↓	5.16	0.00	H2A histone family member V
NEDD4	↓	4.61	0.04	E3 ubiquitin protein ligase
TXNL1	↓	3.62	0.01	thioredoxin like 1
VDAC1	↑	3.45	0.00	voltage dependent anion channel 1
GYG1	↓	3.35	0.00	glycogenin 1
CNTRL	↓	2.67	0.01	Centriolin
PTGIS	↓	2.19	0.08	prostaglandin I2 synthase
ADH1A	↑	2.16	0.00	alcohol dehydrogenase 1A (class I), alpha polypeptide
ADH1B	↑	2.16	0.00	alcohol dehydrogenase 1B (class I), beta polypeptide
ADH1C	↑	2.16	0.00	alcohol dehydrogenase 1C (class I), gamma polypeptide
MT-ATP8	↑	2.09	0.00	mitochondrially encoded ATP synthase 8
DPP7	↑	2.09	0.01	dipeptidyl peptidase 7
KHSRP	↑	2.03	0.04	KH-type splicing regulatory protein
KHSRP	↑	2.03	0.04	KH-type splicing regulatory protein
KRT1	↑	2.00	0.02	keratin 1
CALU	↑	1.95	0.02	Calumenin
MYL6	↓	1.87	0.01	myosin light chain 6
GLRX3	↓	1.71	0.08	glutaredoxin 3
NT5C2	↓	1.67	0.02	5'-nucleotidase, cytosolic II
GDI2	↓	1.66	0.00	GDP dissociation inhibitor 2
TUBB	↑	1.64	0.10	tubulin beta class I

IDH3G	↓	1.63	0.03	isocitrate dehydrogenase 3 (NAD(+)) gamma
ELAVL1	↑	1.61	0.00	ELAV like RNA binding protein 1
UQCR11	↑	1.58	0.00	ubiquinol-cytochrome c reductase, complex III subunit XI
YWHAH	↑	1.54	0.00	tyrosine 3-monooxygenase
AIFM1	↑	1.52	0.05	apoptosis inducing factor, mitochondria associated 1
UNC45B	↑	1.50	0.01	unc-45 myosin chaperone B
PSMC3	↑	1.45	0.13	proteasome 26S subunit, ATPase 3
PTRF	↑	1.44	0.02	polymerase I and transcript release factor
HSPB3	↑	1.43	0.00	heat shock protein family B (small) member 3
DPYSL2	↑	1.41	0.00	dihydropyrimidinase like 2
PGR	↓	1.40	0.04	progesterone receptor
REEP5	↑	1.39	0.01	receptor accessory protein 5
CAP1	↓	1.39	0.03	adenylate cyclase associated protein 1
TLN1	↓	1.37	0.17	talin 1
COX5B	↑	1.36	0.00	cytochrome c oxidase subunit 5B
RPS19	↓	1.36	0.15	ribosomal protein S19
TPT1	↑	1.34	0.01	tumor protein, translationally-controlled 1
RAB1A	↓	1.32	0.10	RAB1A, member RAS oncogene family
NACA2	↑	1.30	0.20	nascent polypeptide associated complex alpha subunit 2
MYL4	↑	1.30	0.00	myosin light chain 4
IVD	↑	1.25	0.20	isovaleryl-CoA dehydrogenase
JUP	↑	1.24	0.01	junction plakoglobin
WDR1	↓	1.24	0.14	WD repeat domain 1
RAB8B	↑	1.23	0.00	RAB8B, member RAS oncogene family
RTN4	↓	1.23	0.14	reticulon 4
ACTN1	↑	1.22	0.02	actinin alpha 1
LMNA	↑	1.22	0.13	lamin A/C
PDHB	↑	1.22	0.13	pyruvate dehydrogenase (lipoamide) beta
UQCRH	↑	1.21	0.02	ubiquinol-cytochrome c reductase hinge protein
UQCRHL	↑	1.21	0.02	ubiquinol-cytochrome c reductase hinge protein like
CYB5R3	↓	1.20	0.14	cytochrome b5 reductase 3

Finally, we looked at those proteins for the 0.5 Gy radiated cells. These can be seen in the table below.

Table 7: Altered proteins in cardiomyocytes after 0.5 Gy radiation

Symbol	Direction	FC	pvalue	Human Description
MYL7	↑	1.79	0.02	myosin light chain 7
MT-ATP8	↑	1.45	0.06	mitochondrially encoded ATP synthase 8
AQP1	↑	1.44	0.02	aquaporin 1 (Colton blood group)
CPT2	↑	1.39	0.02	carnitine palmitoyltransferase 2
IVD	↑	1.37	0.09	isovaleryl-CoA dehydrogenase
VDAC1	↑	1.37	0.00	voltage dependent anion channel 1
RAB1A	↓	1.34	0.12	RAB1A, member RAS oncogene family
DPYSL2	↑	1.33	0.02	dihydropyrimidinase like 2
UQCR11	↑	1.30	0.08	ubiquinol-cytochrome c reductase
ALDH2	↑	1.30	0.01	aldehyde dehydrogenase 2 family (mitochondrial)
RPS14	↓	1.29	0.17	ribosomal protein S14
AKR1B1	↓	1.27	0.05	aldo-keto reductase family 1 member B
HIST1H1B	↓	1.23	0.09	histone cluster 1 H1 family member b
HBD	↓	1.22	0.06	hemoglobin subunit delta
HBB	↓	1.22	0.06	hemoglobin subunit beta
PAFAH1B2	↑	1.22	0.11	platelet activating factor acetylhydrolase
PRDX2	↓	1.21	0.02	peroxiredoxin 2
COX6B1	↓	1.21	0.02	cytochrome c oxidase subunit 6B1

There are a number of common proteins and pathways that have been modulated across these doses. To better display these, we constructed a network diagram revealing a number of important central nodes associated with these changes, with apoptosis-inducing factor (AIF) being an important node that is down regulated (Figure 33).

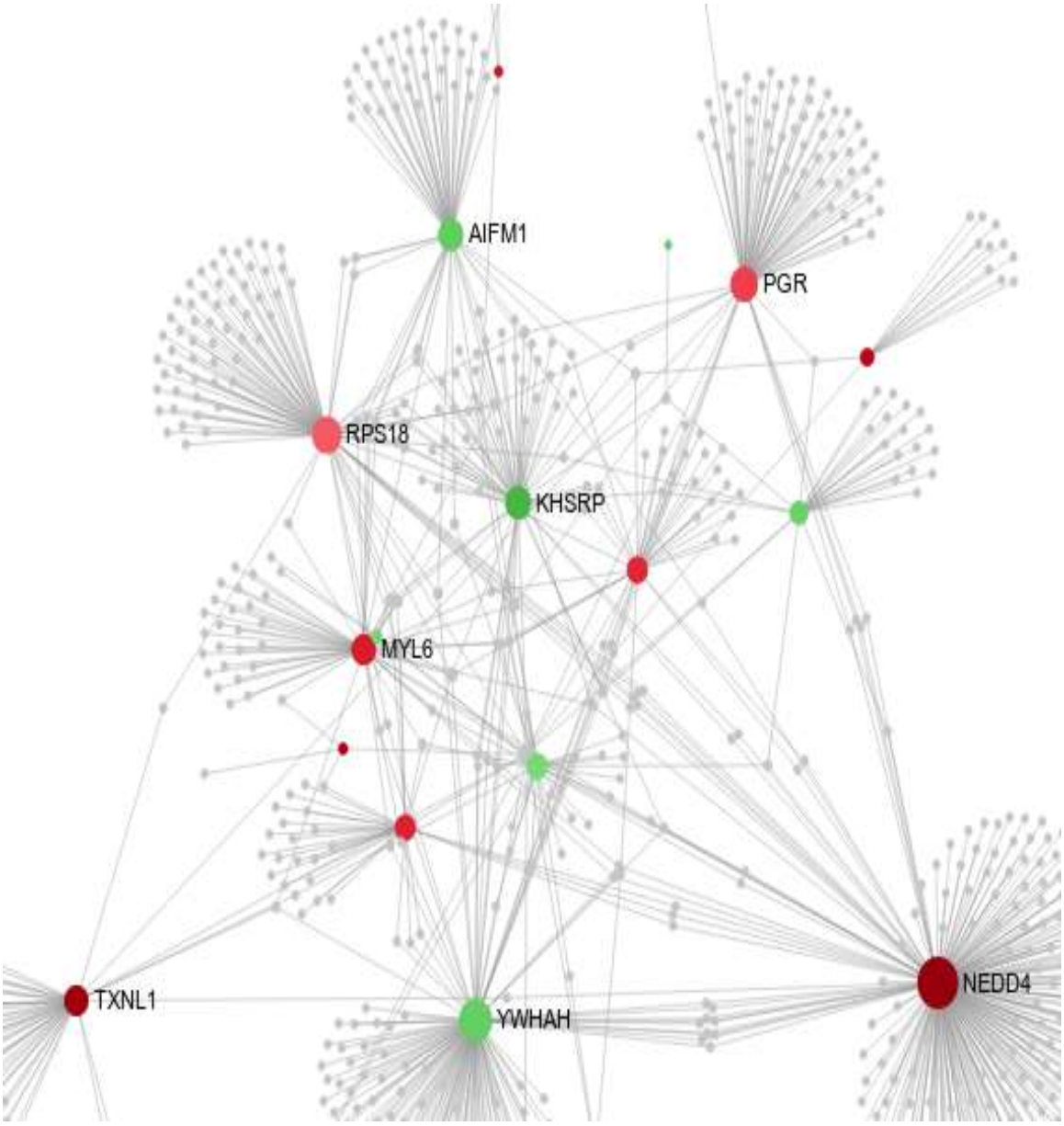

Figure 33: A network diagram of important nodes affected by cardiomyocyte radiation 24 h after exposure

This network diagram helped identify a few important central nodes that are modulated after radiation exposure. NEDD4 was found to be significantly upregulated after radiation. It is a known ubiquitin ligase that has a number of different cellular functions, but importantly it serves to ubiquitinate voltage gated ion channels[121–125]. Importantly, and relevant to our studies, it has been shown to be upregulated post myocardial infarction, which help activate PI3k/Akt signaling and promoting myocyte survival rather than apoptosis[121]. This is the first description of its possible involvement in post radiation cardiomyocyte adaption.

Another import node that has been identified is Apoptosis-Inducing Factor (AIF). It is a known mitochondrial oxidoreductase that is an upstream regulator of caspase independent apoptosis as well as a key protein involved in the assembly of the mitochondrial respiratory chain[126]. Decreased levels of AIF or abnormalities in its function lead to mitochondrial dysfunction[127]. In our studies, AIF downregulated after radiation, which is consistent with mitochondrial injury and dysfunction. This was shown as a central node on our network diagram. Importantly, since we did not see evidence of cell death, decreased levels of AIF are consistent with downregulation of the apoptotic response. This is an important finding given it is a parallel and independent pathway to the caspase apoptotic pathway[126].

We further evaluated changes in AIF expression after radiation in cardiomyocytes using western blot for two different batches of cardiomyocytes.

Figure 34: Western blot of AIF levels 24 h post radiation vs controls

3.3.5. Role of mitochondrial specific ROS scavenger in post radiation cardiac patch function

Given that the proteomics and cell assay data suggest mitochondrial ROS involvement after cardiomyocyte exposure, we used a drug that specifically inhibits mitochondrial ROS production during radiation exposure. Mito-TEMPO is a compound that combines piperidine nitroxide TEMPO with the lipophilic cation triphenylphosphonium. This helps target it to the mitochondria, to act as superoxide dismutase mimetic[128]. It has been shown to decrease mitochondrial specific ROS production[50], with superoxide and alkyl radical scavenging properties[128]. The drug does not have any specificity for individual ROS enzymes, however it is likely to decrease NADPH Oxidase 4 (NOX4) activity, given the direct response of NOX4 to mROS[129]. The therapeutic effect of mito-TEMPO in the setting of radiation induced mitochondrial activation, and its utility in decreasing NOX4 activation and activity has not been previously investigated.

The same set of experiments were carried out as above, with the addition of a treatment arm of mito-TEMPO. Cardiac patches in the mito-TEMPO treatment group were treated with 3 μM of mito-TEMPO at the time of radiation exposure, and were tested after 24 hr. (n=4 individual patches per group). This dose was chosen based on previous reports showing safety and efficacy using this dose in 2D cells[130].

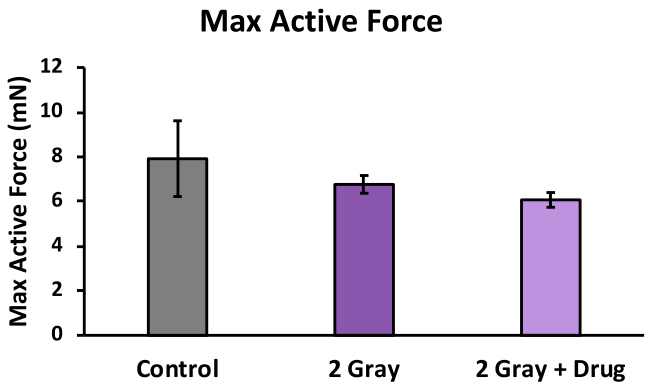

Figure 35: Changes in cardiac patch maximum active force with vs without 3μM mito-TEMPO treatment 24 h after x-ray radiation exposure.

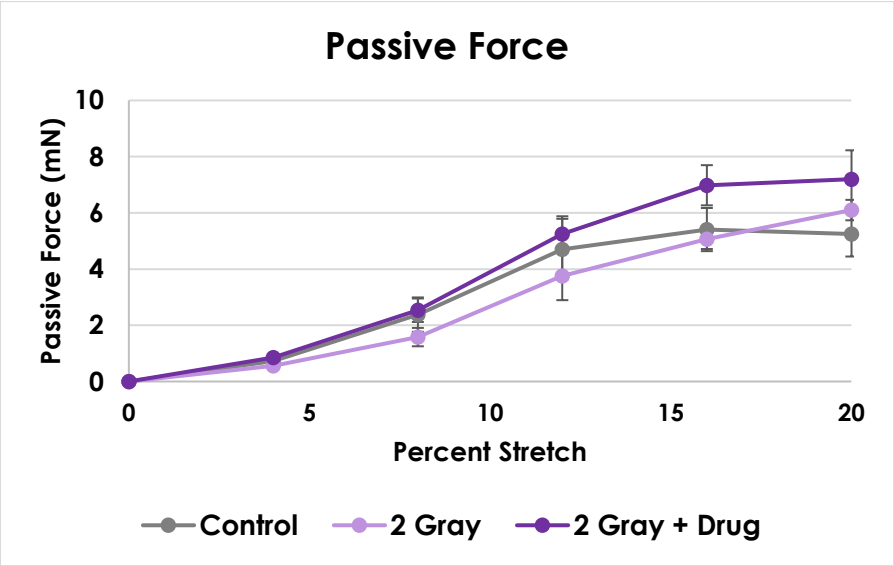

Figure 36: Changes in cardiac patch passive force with vs without mito-TEMPO treatment 24 h after x-ray radiation exposure.

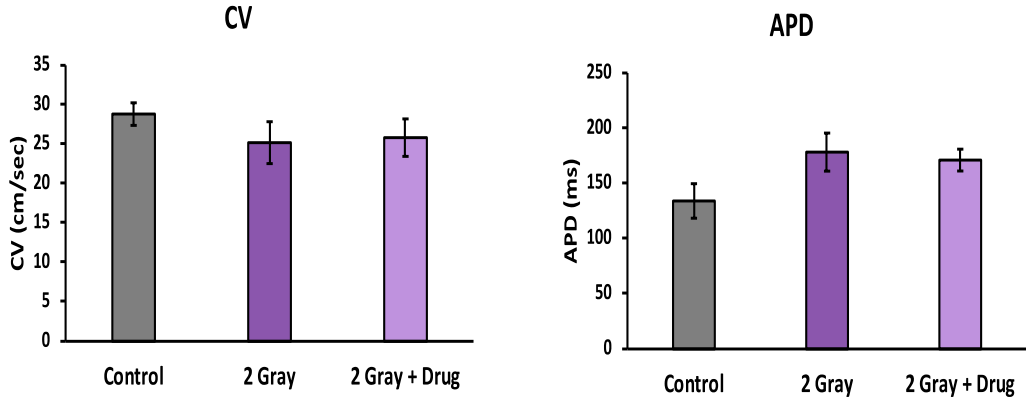

Figure 37: Changes in cardiac patch conduction velocity and action potential duration with mito-TEMPO treatment 24 h after x-ray radiation exposure

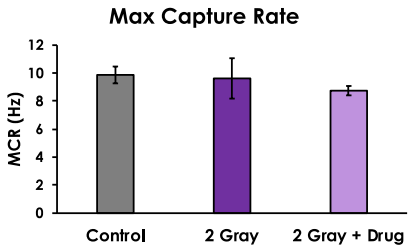

Figure 38: Changes in cardiac patch max capture rate with vs without mito-TEMPO 24 h after x-ray radiation exposure

Across measures of patch mechanical and electrical properties, 3μM treatment with mito-TEMPO did not appear to have an effect on patch function. This might be due to a number of reasons, including incorrect dosing of the drug, the timing of the administration, or the fact that the radiation dose was not severe enough to see an effect from drug administration. Future experiments will focus on performing a dose response curve for the effect of radiation doses on cardiac patch function, followed by another dose response curve to look at the proper dosing of mito-TEMPO for this unique system. Media was also collected from those experiments and will be examined for changes in ROS levels with vs without the drugs. If ROS levels appears unchanged, that lends more evidence to issues related to drug dosing, or administration time.

3.4 Discussion

In this study, we demonstrate an early and significant change in the proteome as well as the production of ROS within 24 hr of radiation exposure to isolated cardiomyocytes. Bioinformatics analysis of the proteomic dataset generated revealed an important protein turnover seen mainly within the mitochondrial machinery. In our

interpretation, this is convincing evidence of direct damage to the cardiomyocytes experienced from low dose radiation. Even at 24 hours, there appears to be small changes in cardiomyocyte mechanical and electrical properties. The long-term consequences of such changes have not been explored.

Cellular sensitivity to radiation varies among different cell types[131]. Adult cardiomyocytes are post mitotic and non-dividing, and relatively radioresistant[132]. Consistent with literature, we did not observe significant cell lysis or activation of the apoptotic pathway in cardiomyocyte as the mechanism of disease[132]. Most studies examining the effect of radiation on the heart *in vivo* however, are unable to differentiate the biological effect on the endothelium within the heart (coronary arteries) vs that to the cardiomyocytes[47]. Importantly, a hallmark of cardiac radiation damage is coronary artery disease, and increased risk of myocardial infarctions[133]. This maybe solely caused by endothelial damage and injury within the coronaries or arterial system causing a secondary cardiac specific effect[37]. In this study, we were able to study the direct effect of radiation on isolated cardiomyocyte.

To overcome the limitation of using 2D cells cultured on a plate, we used a novel dynamic cardiac patch system that allows us to examine relatively sensitive functional parameters affected by radiation[134]. These cardiac patches exhibit uniform and high volume density, cross-striations, and robust electrical and mechanical junctions much closer to what is seen in vivo as compared to 2D cells[111,134–136].They show spatially

uniform action potential conduction across the entire patch, and increase in contractile force with stretch, with average conduction velocities most resembling *in vivo* conditions compared to other patch systems[135]. We used these engineered cardiac patches as a surrogate of human heart tissue to evaluate the effect of 2Gy radiation doses on cardiomyocyte function. Within 24 h, radiated patches had a trend of a decrease in active force, and conduction velocity, with an increase in action potential duration. These findings are consistent to what is expected in early and subtle cardiac injury. In this study we limited the evaluation to early changes, future planned studies will look at this effect long term. It is currently unclear if such effect is likely to get worse with time or will improve. Importantly, these changes might play a role in secondary inflammatory changes in the heart reported[41,137] after radiation exposure, as they might influence inflammatory cell recruitment and activation. Furthermore, these inflammatory changes are important first steps in eventual cardiac fibrosis, an important hallmark of high dose cardiac radiation exposure[138,139].

In these studies, there was no difference in the GSH/GSSG ratio for different doses of radiation as compared to control. Glutathione (GSH) is an important cellular antioxidant serving as a free radical scavenger in healthy cells. In healthy cells, reduced GSH, should be significantly higher than oxidized GSH (GSSG)[140]. This ratio has been previously shown to be an important index of radiation exposure in both animal and human experiments[141]. Our failure to see a difference in our model system could be

related to the cell type we are studying, as it appears that the liver is a major producer of GSSG[141]. Furthermore, in one study, the levels were significantly altered immediately, but began to normalize after 6 h[141]. Since we evaluated the media at 24 h post radiation, the level derangements might have been missed.

A number of reports have suggested that energy metabolism derangement is an important factor leading to cardiovascular dysfunction after radiation exposure. In our study, mitochondrial pathways were significantly altered on proteomics analysis, and we saw significant increase in oxidative stress even at the lower doses (0.1Gy). This was further confirmed by western blot showing significantly decreased AIF levels in radiated cardiomyocytes as compared to controls.

Apoptosis-inducing factor (AIF) is a mitochondrial oxidoreductase that is important to the assembly of the respiratory chain, stabilization of complexes I and III and decreased levels are associated with mitochondrial dysfunction[126,127]. Other downstream signaling of AIF is also important for mitochondrial bioenergetics[127]. Therefore, our finding of decreased levels of AIF post radiation has important implications for cardiomyocytes, a cell type where mitochondria make up nearly 30% by volume[142]. Proper mitochondrial health is essential for cardiomyocyte health, and small derangement have important implication for cardiomyocyte contractile function[142]. In one *in vivo* mouse study of chronic radiation, heart mitochondria were isolated and studied long term after radiation exposure. The authors found significant changes in

mitochondrial acetylation and impairment metabolism[142]. Therefore, these early mitochondrial changes seen might have long term consequences on cardiac function.

Another notable observation from the proteomics analysis is the finding that relative to the biological variability, the technical replicates ('pool' runs) are grouping more tightly together, suggesting biological variance is much higher than technical variance. This might be due to a number of reasons, including ones explained by differential pathways that are activated at different radiation doses. This is evident when looking at the Venn diagram showing a number of differently activated proteins comparing the 0.5 Gy vs the 0.3 Gy doses as compared to controls.

The statistical analysis applied did not have biological powering sufficient to allow for multiple hypothesis correction. This test resulted in 4 peptides with $p<0.05$ at 0.1 Gy versus 0 Gy, 24 peptides with $p<0.05$ at 0.3 versus 0 Gy, and 8 peptides with $p<0.05$ at 0.5 versus 0 Gy. The data for the potentially oxidizable amino acid residues is therefore also suggestive that the observed differences between 0 and 0.3 Gy were greater than those between 0 and 0.5 Gy. It must be emphasized that with the low effect size of these changes combined with the low biological "n" of the experiment, the 'observed' differences being greater between 0.3 (vs 0) compared to 0.5 (vs 0) could simply be due to a slightly lower biological variability in the 0.3 Gy sample set.

3.5 Conclusion

With the dramatic increase in low dose radiation exposure to the average individual today, it is imperative to further our understanding of the biological effects of such exposure on the cardiovascular system. In this study, we demonstrate an early and significant change in the proteome as well as the production of ROS within 24 hr of radiation exposure to isolated cardiomyocytes. Bioinformatics analysis of the proteomic dataset generated reveled an important protein turn over seen mainly within the mitochondrial machinery. In our interpretation, this is convincing evidence of direct damage to the cardiomyocytes experienced from low dose radiation that is independent of secondary effects of inflammation.

4. Effect of Radiation on early vascular dysfunction

4.1 Background and Introduction

The primary cell types in the vasculature are endothelial (EC) and smooth muscle cells (SMC). These are complex cell types with a variety of functions[143–145]. Importantly, they have a significant level of interaction that is required for vascular health[146], including (a) cell to cell communication, (b) eNOS derived NO, (c) shared extracellular matrix, (d) communication via extracellular vesicles, and microRNA, and (e) shared response to external injury/stimuli[147]. Insights into the EC-SMC interaction have been in the field of atherosclerosis[82,99,147,148].

Much of the focus has been placed on endothelial cells (ECs) as the primary driver of vascular injury and disease. A large body of literature highlights the dynamic and complex role and function of the endothelium with mechanical, antithrombotic, immunological, secretory, synthetic, and metabolic functions[149–156]. They have unique features in different areas of the body, adding to the complexity of this cell type[157]. In the field of radiation biology, IR causes early and late changes to endothelial cells that have important consequences for both vascular and cardiovascular health[70,85,158–162].

Smooth muscle cell aberrant proliferation is an important hallmark for a number of vascular diseases and atherosclerosis. In addition, SMC apoptosis, senescence, and transformation to macrophage-like cells may promote inflammation[163]. Therefore, a

study of the effect of radiation on vascular is not complete without a better understanding of its effects on SMCs.

4.1.1 Dose Rationale

Epidemiological studies conducted in Japanese atomic bomb survivors demonstrated that an acute single dose of 2 Gy had a clinically and statistically significant increase in mortality from myocardial infarction, with a 17% increase in CVD related events for every 1 Gy increase in received dose[85,164]. These findings are further supported by studies using those having occupational radiation exposure, nuclear power plant works and the Chernobyl incident[85,165]. However, a systematic review on this topic, looking at 26 published epidemiologic studies dealing with radiation doses 0-5Gy, concluded that there is currently no clear evidence of an increased risk of cardiovascular disease at these doses[165]. Therefore, there remains an important gap in the literature of the consequence of these radiation doses on short- and long-term vascular health. Furthermore, there is an important need to better understand the consequence of these radiation doses to the cellular biology of ECs and SMCs beyond DNA damage.

4.1.2 Overview of the literature on endothelial cell radiation studies

In an effort to perform a comprehensive survey of the literature on the effect of radiation on endothelial cells and identify important trends as well as gaps in our knowledge on the topic, we performed a systematic review of articles with 'MESH' terms involving radiation and endothelial cells.

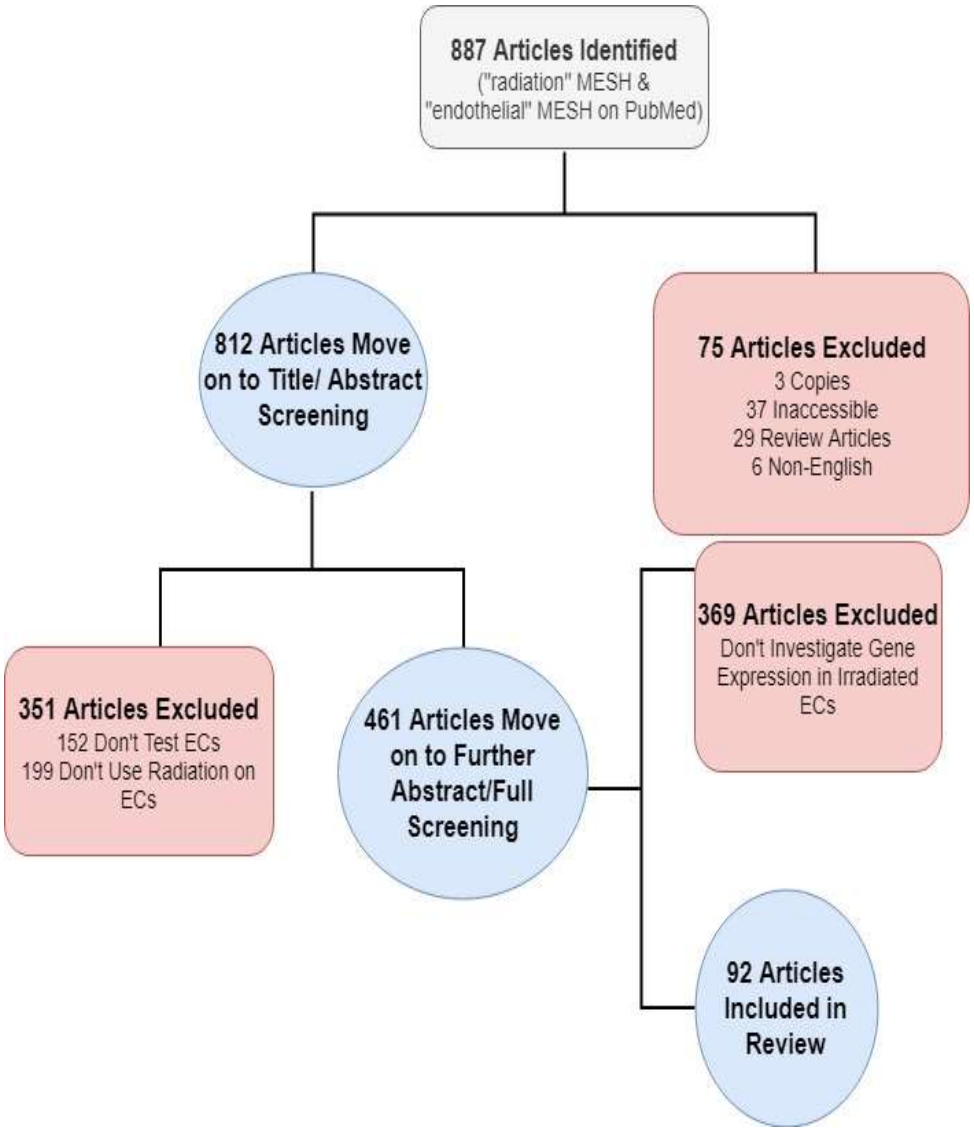

Figure 39: Tree diagram of the systematic review evaluating studies reporting on endothelial cell radiation

As expected, there is a large body of literature dealing with this topic, with over 90 articles identified that relate to the search criteria. After evaluation of these studies,

they were grouped according to the endothelial cell types used, types and doses of radiation and the main important findings. The majority of articles used X-rays, Gamma rays and UV radiation, with some not specifying in the main text the type of radiation used.

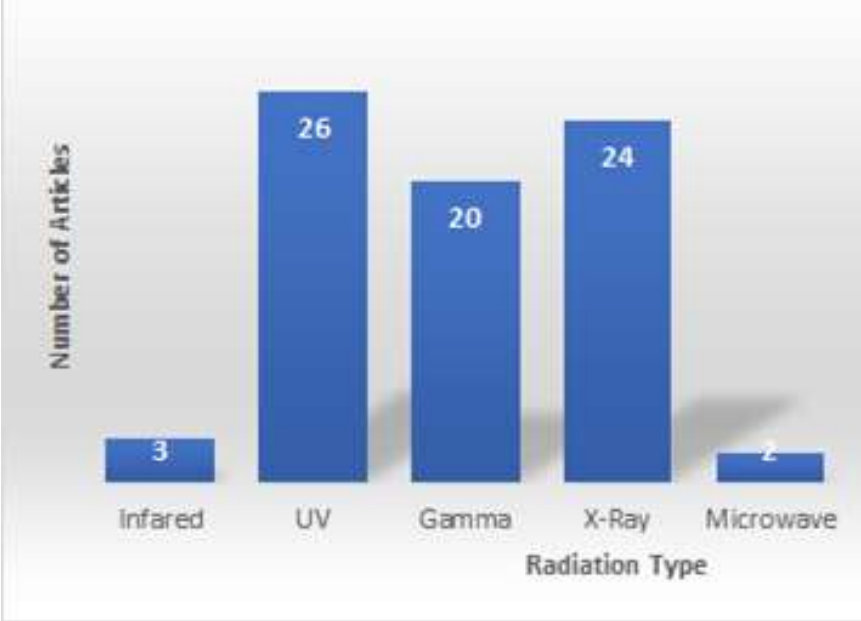

Figure 40: Types of radiation used by the studied articles in endothelial cells

We then wanted to better understand the doses these articles investigated. This was done by grouping articles according to dose ranges studied. It was clear that the doses studied were highly variable, with 10 Gy having the most number of articles that specifically evaluated it.

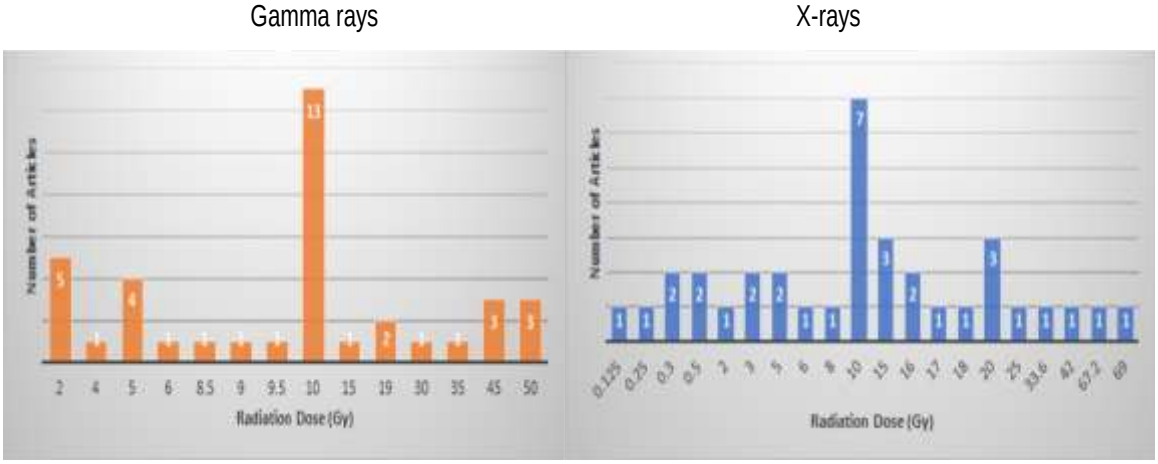

Figure 41: Distribution of doses used in the identified studies for both gamma rays (left) and x-rays (right)

The most common species was human, followed by mouse ECs. However, there were a few other species evaluated.

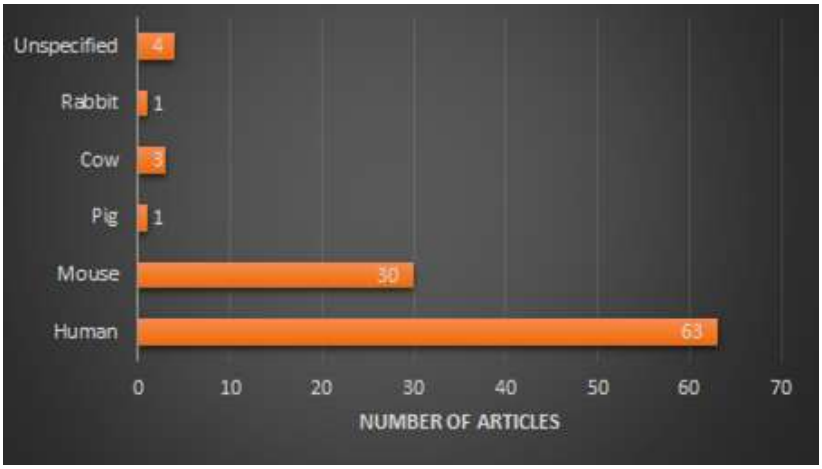

Figure 42: EC sources used for the different studies

Finally, and perhaps most relevant to this discussion, is the type of ECs used was found to be highly variable. When we limited the studies to those looking at human source of the ECs, a large number of different cell types were identified.

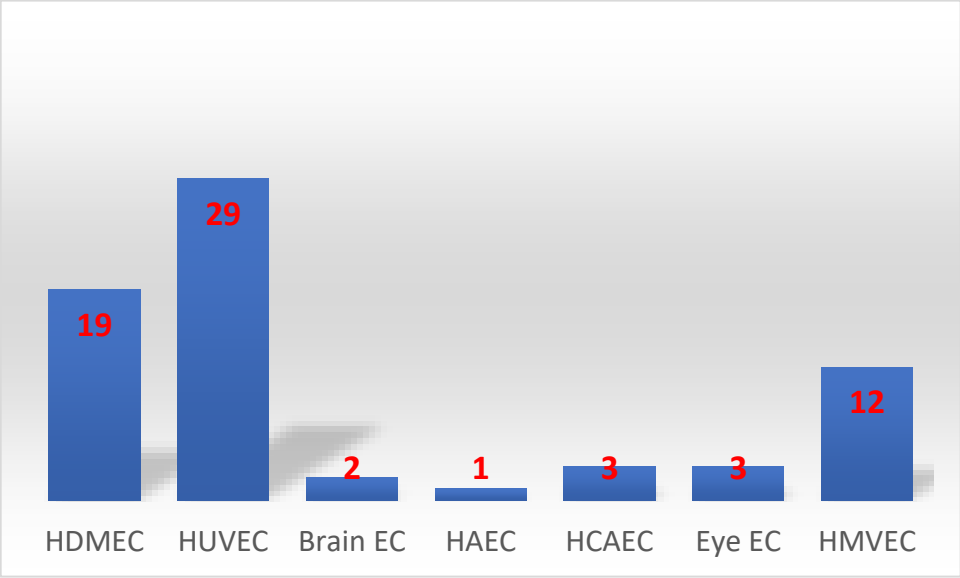

Figure 43: Types of different ECs used for human studies

The most common EC type was Human Umbilical Vein Endothelial Cells (HUVEC), followed by Human Dermal Microvascular ECs (HDMEC). There were 12 studies that used a more general microvascular ECs but did not specify the locations (HMVECs). Finally, a few studies used "eye" and "brain" ECs, one study used Human Aortic ECs (HAECs) and 3 used Human Coronary Artery ECs (HCAEC). These are important differences, as ECs have unique properties based on their source, with clear and documented differences between their different functions[166]. For all the experiments performed for this dissertation, we exclusively used primary coronary artery endothelial cells (CAECs) or cord blood derived endothelial colony forming cells (CB-ECFCs). These

cells have been shown in our lab to have excellent properties and responses to different stimuli[167–171].

Finally, we can then take studies that used similar ECs types, source, and dose, and evaluate changes of gene and cell functions that were examined. We did this for Human HUVECs that received 10 Gy or radiation, comparing Gamma vs X-rays.

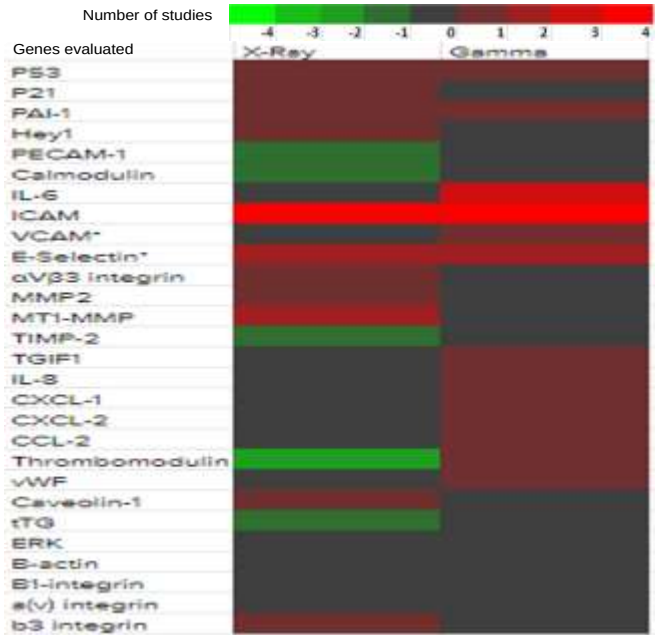

Figure 44: Heat map of literature review of gene changes. The color represent the direction of change (red, overexpression, and green, under expression). The color tone represents the number of studies validating the directional change.

The negative values are a down regulation of the gene (shades of green), and positive values are upregulation (shades of red). The most consistent and studied effect of radiation response of the endothelium is upregulation of adhesion molecules (ICAM-

1, VCAM-1, and E-selectin). There was significant variability in the timing of the experiments, making it difficult to pool these studies to study the overall effect[172,173]. Timing is important, as endothelial adhesion molecules have important type dependence to their expression[172].

The second most consistent finding is the over expression of Plasminogen Activator Anhibitor-1 (PAI-1). A number of studies has established a strong association between elevated PAI-1 levels and multiple consequences, including thrombosis and atherosclerosis[174–176].

Finally, the last consistently activated pathway across studies of radiation response in the endothelium is p53. While this pathway has been extensively studied for decades in response to high dose radiation and tumor response to radiation treatment, its role in modulating normal vascular function after low to medium doses of radiation is poorly understood[177]. Furthermore, new insights into the function of p53 "pulses" and how its complex expression patterns modulate cellular response has recently emerged[177,178]. One common pathway that combines the different findings from the literature review is endothelial cellular senescence.

4.1.3. Cellular senescence and p21 pathway

Cellular senescence is a unique pathway that is mainly characterized by replicative arrest[75,179,180]. However, in endothelial cells, senescence is a unique phenotype that includes changes in EC function, and has been implicated in a number of

cardiovascular diseases[66,153,181]. Of note, recent evidence has demonstrated the role of aging on endothelial senescence and the association with cardiovascular disease[182–184]. A master regulator of cellular senescence is p21. It is cyclin dependent kinase inhibitor (CDKI) that is activated by p53 in response to a number of different stimuli including radiation[185]. As discussed in the first chapter, this process is driven by ATM, as a consequence of "sensing" double stranded DNA breaks. This a protective cellular pathway to maintain the integrity of the DNA and arrest the cell cycle prior to DNA replication. It is currently not known how ATM phosphorylation and activation of p53 can either cause cellular senescence or cellular apoptosis. It is thought to be mainly due to the amount of double stranded breaks encountered, which leads to different signal intensity in p53 phosphorylation (and pulsation)[178]. In the following studies, we use a small molecule (Selleckchem, KU55933-ATM Kinase Inhibitor) that blocks the activity of ATM[186]. It has an IC50 of 6.3 nM for ATM in cell-free assays, 270- and 1600-fold more selective for ATM compared to DNA-PK, PI3K/PI4K, ATR and mTOR.

ATM is also thought to directly activate p53 binding protein (P53BP). Once activated, it relocates to the sites of double stranded DNA breaks and plays an important role in the recruitment of the remainder of the repair machinery. Cells deficient of P53BP are radiation prone, with a defective DNA damage response[187].

Another protein that is activated by ATM is H2A.X. This is done by phosphorylation at serine 139, where the activated yH2A.X is recruited to the site of

DNA break, and involved in the repair process[25,31,188]. Antibodies against yH2A.X are therefore often used for immunostaining and immunohistochemistry to detect the degree of double stranded DNA breaks[32,33].

4.1.4. ROS, mROS and blocking their effect after radiation

Increased ROS production is an important driving factor in EC and SMC injury post radiation exposure[72,80]. IR causes mitochondrial damage[49] and increased mitochondrial release of ROS[84,55]. Both mitochondrial damage as well as increased cellular levels of ROS leads to endothelial senescence[75,85]. Increased levels of ROS in radiated ECs is also thought to affect other nearby ECs in what is called the "bystander injury"[189]. The radiation injury followed by the increased ROS levels and further injury is a type of stress-induced premature senescence (SIPS), and is a major contributor to endothelial dysfunction[73,80,129,143]. Therefore, strategies to decrease ROS production after IR exposure has been used by many groups to mitigate cellular radiation injury[190]. However, as discussed previously, mROS are the main source of ROS after IR, and therefore, strategies that target mROS specifically might have an improvement in efficacy over a generalized antioxidant approach. Furthermore, targeting mROS might break the ROS-induced-ROS cycle[62]. Similar to the experiments in cardiac patches, we use mito-TEMPO as a strategy to block mROS specific release and compare that with the strategy of inhibiting ATM.

H2A.X, P53BP and P21 expression are therefore used as reproducible marker of DNA breaks (H2A.X and P53BP), and endothelial and SMC cell senescence (P21) as an output assay of vascular response to different types of injury. This can be done using western blotting of protein levels, immunofluorescence with image analysis limiting expression to the nuclease (percent positive nuclear staining) or PCR analysis of gene expression.

4.1.5 Hypothesis

Our hypothesis for this part of the dissertation is that a single dose X-rays leads to increased mitochondrial ROS activity that leads to early vascular cell senescence through enhanced p21 activity

4.2. Methods

This hypothesis will be tested using human primary coronary artery endothelial cells and smooth muscle cells. These cells will be used at p4-p6. They will be grown and passaged in T75 flasks, and prior to the radiation or doxorubicin exposure they will be plated in 6well plates at 80-90% confluence. They will undergo treatment with mito-TEMPO or ATM-Inhibitor 24 hours prior to exposure. All radiation experiments will be carried out using x-rays with a XRAD320, at a dose rate of 1.96 Gy/min (Duke Sands facility). They will then be fixed at 24 h after exposure, for the different analyses shown. Immunofluorescence protocol is provided in the appendix. For using nuclear specific positive cells, a DAPI mask is used in ImageJ as previously described[191] (ImageJ.net). In

brief, after staining the cells with the primary and secondary antibodies with the addition of DAPI, the cells are maintained in PBS. They are then imaged at 20x magnification, using the same exposure for each marker of interest (3-6 images per well, and 3-6 wells per condition). The images are then processed in a blinded fashion. For nuclear specific proteins (p21, ATM, P53BP), the DAPI images are analyzed first, and a mask is created. Next, that mask is used to create a region of interest (ROI) to look only at the nuclear component of the images for florescence.

4.2.1 Dysmorphic nuclear shape and radiation injury

A recent growing body of literature is developing relating to the importance of the nuclear shape and size and its association with different diseases[52]. The nuclear lamina provides much more than a mechanical structure, but importantly controls the trafficking of molecules in and out of the nuclease. Lamin proteins make up the main structural block, and many diseases involving it are termed laminopathies[192–194]. These diseases share a number of key elements including a misshaped nuclear envelope, changes in DNA synthesis and damage repair responses, differences in transcription and the regulation of genes involved in the response to oxidative stress[194–197].

Given that our lab studies progeria, we have a method for quantifying the percent of cells with "dysmorphic nuclei"[198]. It was noted early during our radiation experiments that some of the radiated cells appeared to have dysmorphic nuclei. There has been a scarcity of reports on this observation, with no mechanistic understanding of

such effect. Importantly it is unknown if this is a consequence of secondary ROS increases in radiated cells causing such abnormalities, or a different mechanism.

Therefore, this was added an important endpoint measure given its consequence on changes in gene transcription and translation as well as overall cellular health. It is currently unknown however if this nuclear shape change is alone is causative of cellular dysfunction.

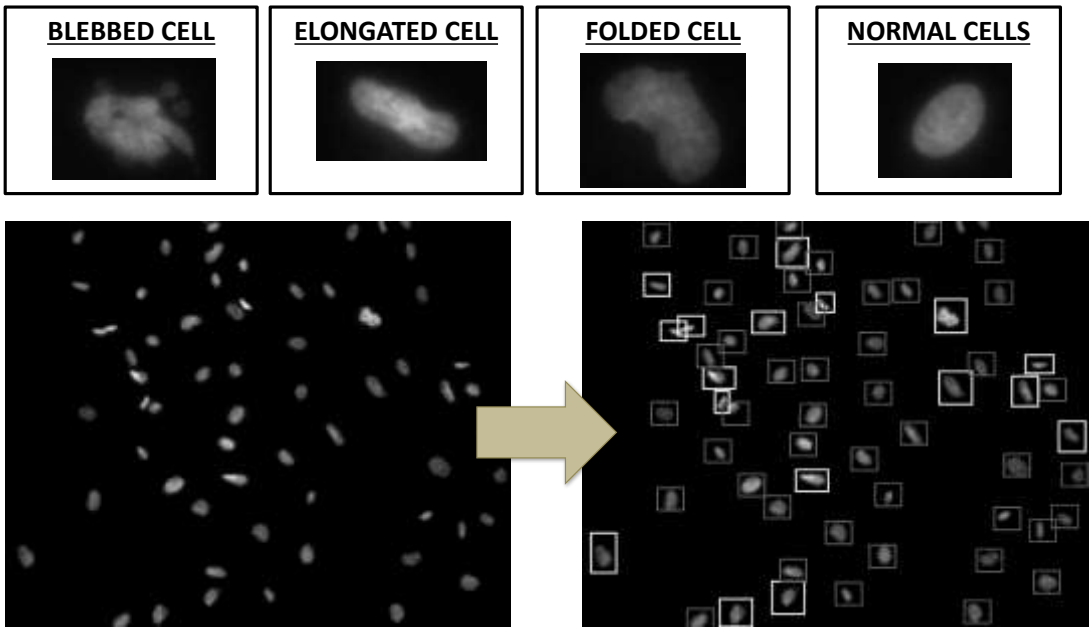

Figure 45: Method for quantification of dysmorphic nuclei using DAPI staining

4.2.2 Cell culture and immunofluorescence

Primary coronary artery endothelial cells (CAECs) or cord blood derived were seeded at a concentration of 20-30k per cm^2 in either 6, 12 or 24 well plates. They were

irradiated (5 Gy) using the XRAD320 at a dose rate of 1.96 Gy/min. 24 h after radiation, a number of different assays were performed to investigate early markers of DNA Damage (H2A.X, P53BP, Abcam primary Rb Ab)[188], cellular senescence (p21, Abcam Rb Ab)[199]. Finally, derangements to nuclear envelope structure were assessed by comparing the number of dysmorphic nuclei on DAPI staining[200]. For H2A.X expression, a primary antibody (Millipore, 05-636-I, dilution 1/500) was used. This antibody is specific to the phosphorylated H2A.X at the Ser139 position (which is the activated form).

In an effort to characterize changes in ATM staining with radiation, and the efficacy of the dosing of our ATM-inhibitor, cells were grown and platted as previously described. They underwent a media change 24 h prior to radiation with the addition of the ATM-inhibitor to the appropriate treatment groups. 24 h after radiation exposure, they were fixed per our immunofluorescence protocol in the Appendix, and stained with anti-ATM antibody (Abcam ab32420 at 1/1000 primary antibody dilution). Doxorubicin (Sigma-Aldrich, D1515) was used to induce senescence at 50 nM per the manufacturer's recommendation. ATM-Inhibitor, Selleckchem, KU55933-was used at 10nm per the manufacturer's recommendation.

4.3 Results

4.3.1 IR causes increases in dysmorphic nuclei early after radiation exposure

After radiation (5 Gy xray), an increased proportion of cells had dysmorphic nuclei. These changes were seen as early as 5 h after radiation, and were presistant for a

few days. They were not examined long term. In one experiment, CB-ECFC were radiated using 5Gy X-rays, and fixed 24 h after exposure. Using DAPI staining, the percent of cells with Dysmorphic Nuclei doubled from 20% in the controls to 40% ($p<0.05$) in the irradiated (Figure 46, and Figure 47, n= 9 per group). This is a novel finding in otherwise healthy cells especially this soon after radiation exposure.

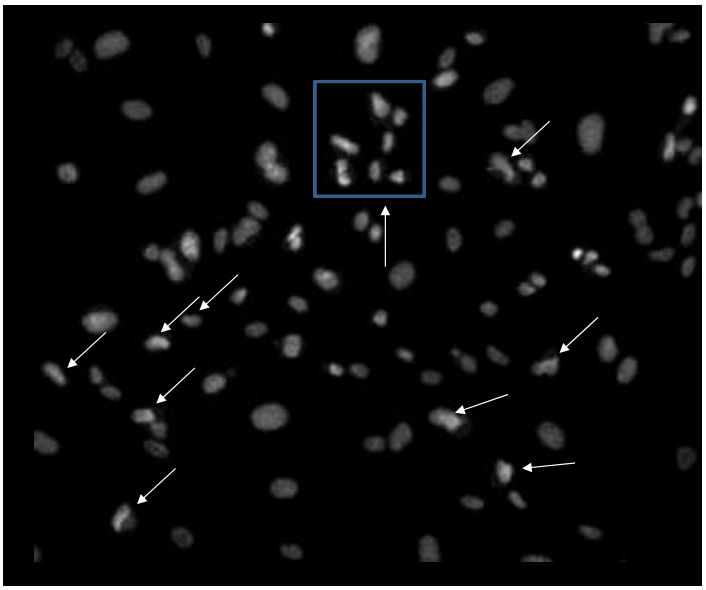

Figure 46: Effect of 5 Gy of radiation on dysmorphic nuclei at 24 h post x-ray exposure

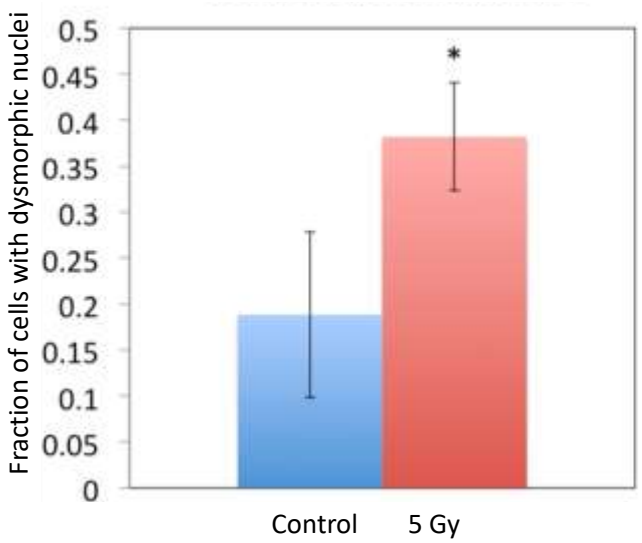

Figure 47: Percentage of dysmorphic endothelial nuclei 24 h post x-ray radiation

4.3.2 Changes in ATM staining in ECs and SMCs with radiation and ATM-Inhibitor

In the next set of experiments, we evaluate elements of the DNA damage repair pathway (H2A.X and P53BP) with ECs and SMCs that have been exposed to IR (X-rays, Xrad320, dose rate 1.96Gy/min) and Doxorubicin.

For the ECs, an extra control was added, with one control having no ATM-inhibitor added to the non-irradiated cells, and a second control having ATM-inhibitor added to look at changes in baseline ATM expression. (n=3 biological replicates, 6-9 technical replicates per treatment group, * $p<0.01$) (Figure 48). This is a confirmatory finding that the ATM-Inhibitor is able to decrease ATM expression after IR induced double stranded DNA breaks.

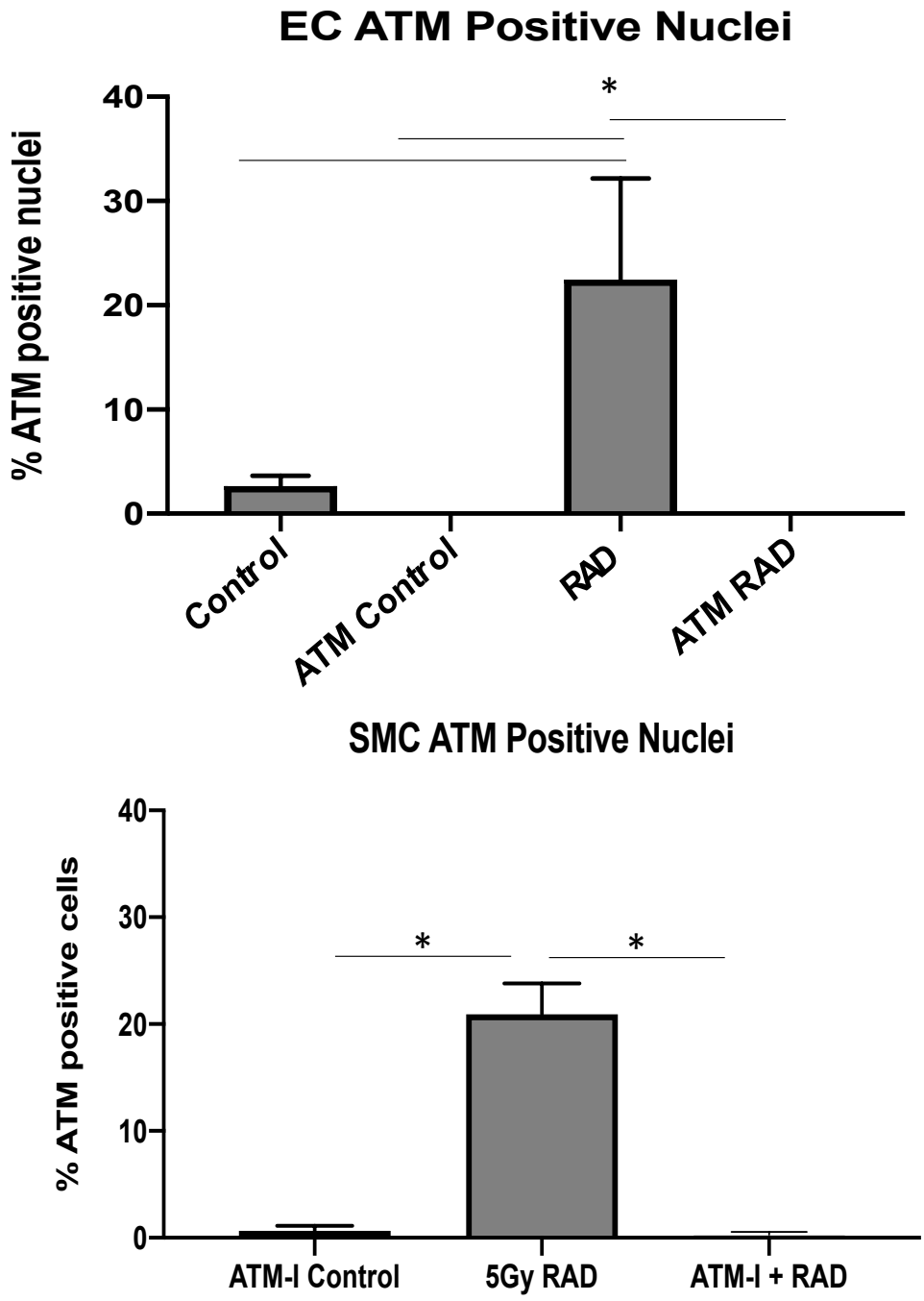

Figure 48: Changes in ATM expression after endothelial and smooth muscle cell radiation with vs without treatment with an ATM-inhibitor. Cells were evaluated using immunofluorescence 24 h after x-ray exposure

4.3.3 Changes in yH2A.X staining in ECs and SMCs with radiation and mito-TEMPO

As has been shown by numerous publications, radiation exposure causes double stranded DNA breaks, that leads to an increase in H2A.X expression[188,201]. However, it is currently not known if early mito-TEMPO treatment leads to a decrease in the acute phase of H2A.X expression. Our hypothesis is part of the DNA breaks seen after radiation exposure are due to mROS production secondary to mitochondrial activation. This hypothesis will be tested, but using mito-TEMPO to specifically block mROS after radiation exposure and evaluating degree of DNA damage compared to untreated cells, and subsequent p21 expression.

Cells were pretreated with 3 μM of mito-TEMPO 24 hr prior to radiation exposure. 24 h after radiation, the cells were fixed and stained for yH2A.X expression. As expected, radiation lead to a dramatic increase in cells expression H2A.X, however, there appears to be no difference with mito-TEMPO treatment (Figure 49). This may be due to the fact that early DNA damage from radiation exposure is related to the direct effect of the IR on the DNA, with little involvement of the mROS system.

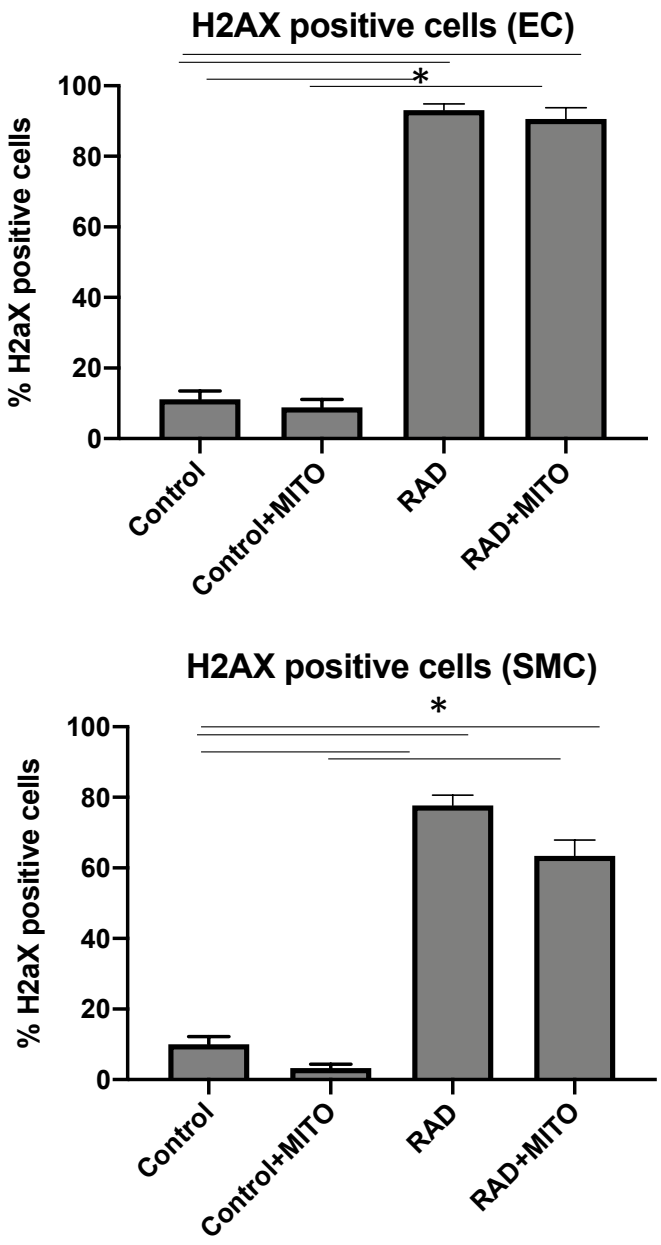

Figure 49: Changes in H2A.X expression in ECs (top panel) and SMCs (bottom panel) after x-ray radiation with vs without mito-TEMPO treatment

4.3.4 Changes in yH2A.X staining in ECs and SMCs with Doxorubicin, mito-TEMPO and ATM-Inhibitor

In the next set of experiments, we investigated yH2A.X expression in ECs and SMCs exposed to Doxorubicin for 24 h, and treated with mito-TEMPO, ATM-inhibitor, and the combination of the two. In the control cells, Doxorubicin administration lead to over 90% of cells to express H2A.X as compared to less than 5% in the non-treated cells ($p<0.01$). With mito-TEMPO treatment, there appears to be no change in H2A.X expression contrary to what we anticipated. This is likely related to that fact that the drug interacts directly on the DNA to cause DNA breaks, regardless of the mROS response. However, the administration of an ATM-inhibitor, caused a profound decrease in H2A.X expression. Interestingly, in the non-Doxorubicin treated control cells, ATM-inhibitor caused some increase in H2A.X expression over background (Figure 50). The cause of this is unclear, however it was consistent across 3 different replicate experiments.

Finally, the combination of Mito-TEMPO with ATM-inhibitor did not have any differences to ATM-inhibitor alone.

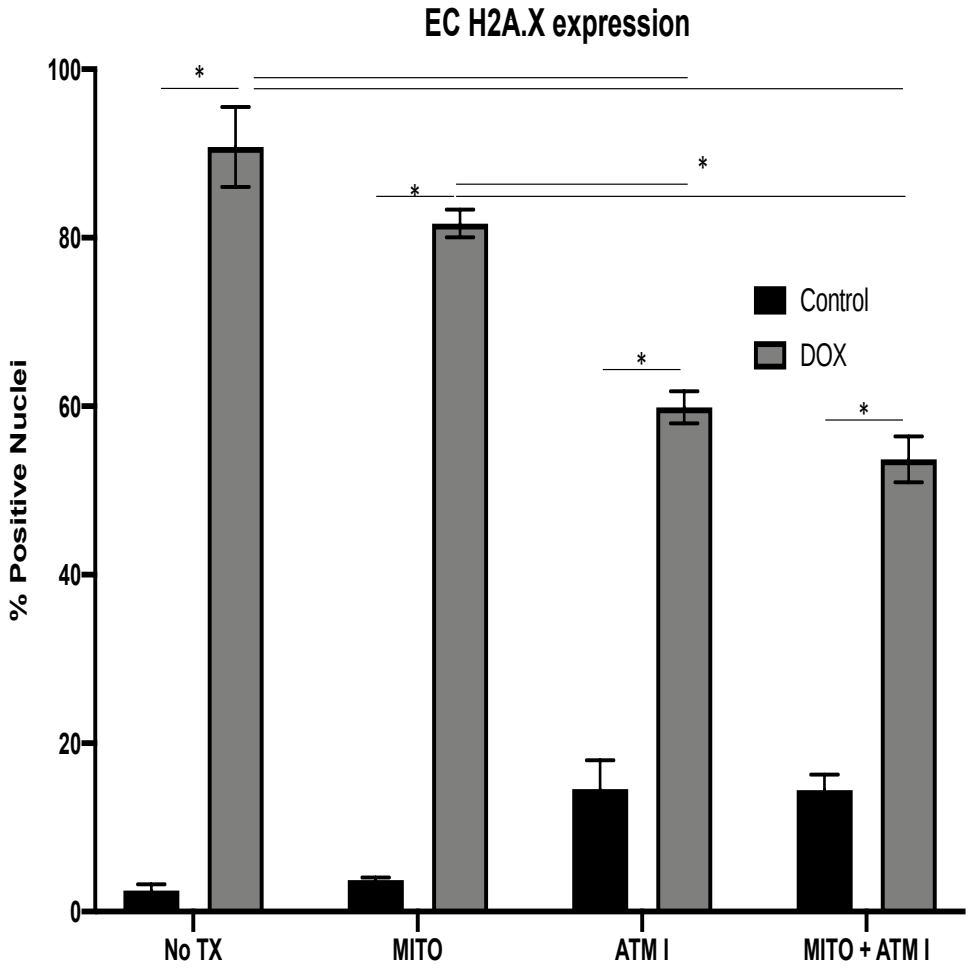

Figure 50: Changes in H2A.X in ECs with vs without Doxorubicin and ATM-Inhibitor. Cells were pretreated with ATM-Inhibitor 24 h prior to Doxorubicin exposure, and were then fixed and stained 24 h after

The same pattern was seen for SMC treated with Doxorubicin (Figure 51).

However, unlike ECs, the overall level of H2A.X nuclear expression was less. For instance, for the control group the expression of H2A.X was around 43%, which is almost half of the expression levels seen in ECs.

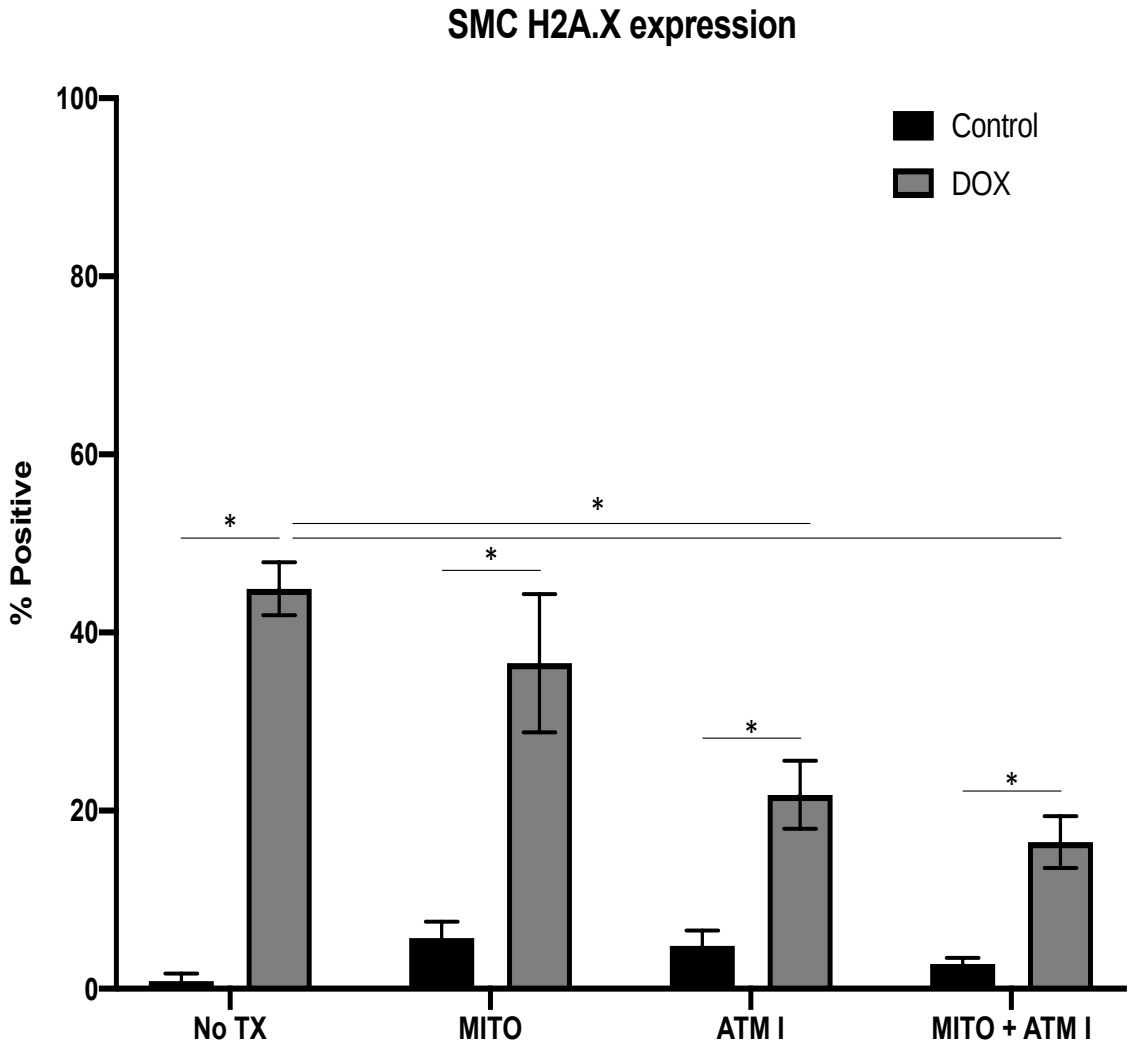

Figure 51: Changes in H2A.X in SMCs with vs without Doxorubicin and ATM-Inhibitor. Cells were pretreated with ATM-Inhibitor 24 h prior to Doxorubicin exposure, and were then fixed and stained 24 h after

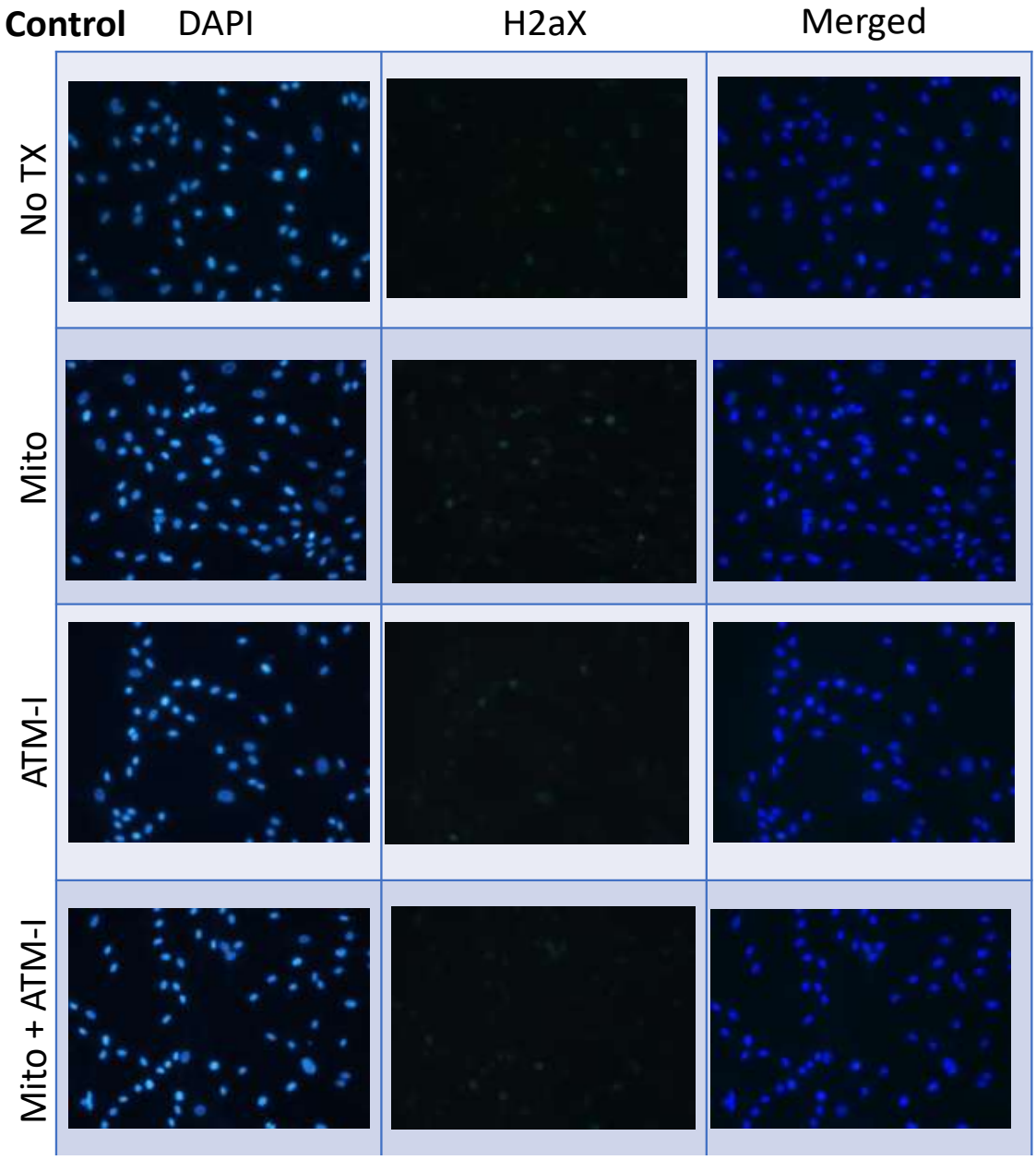

Figure 52: Representative IF images of control ECs H2A.X expression with different treatment groups

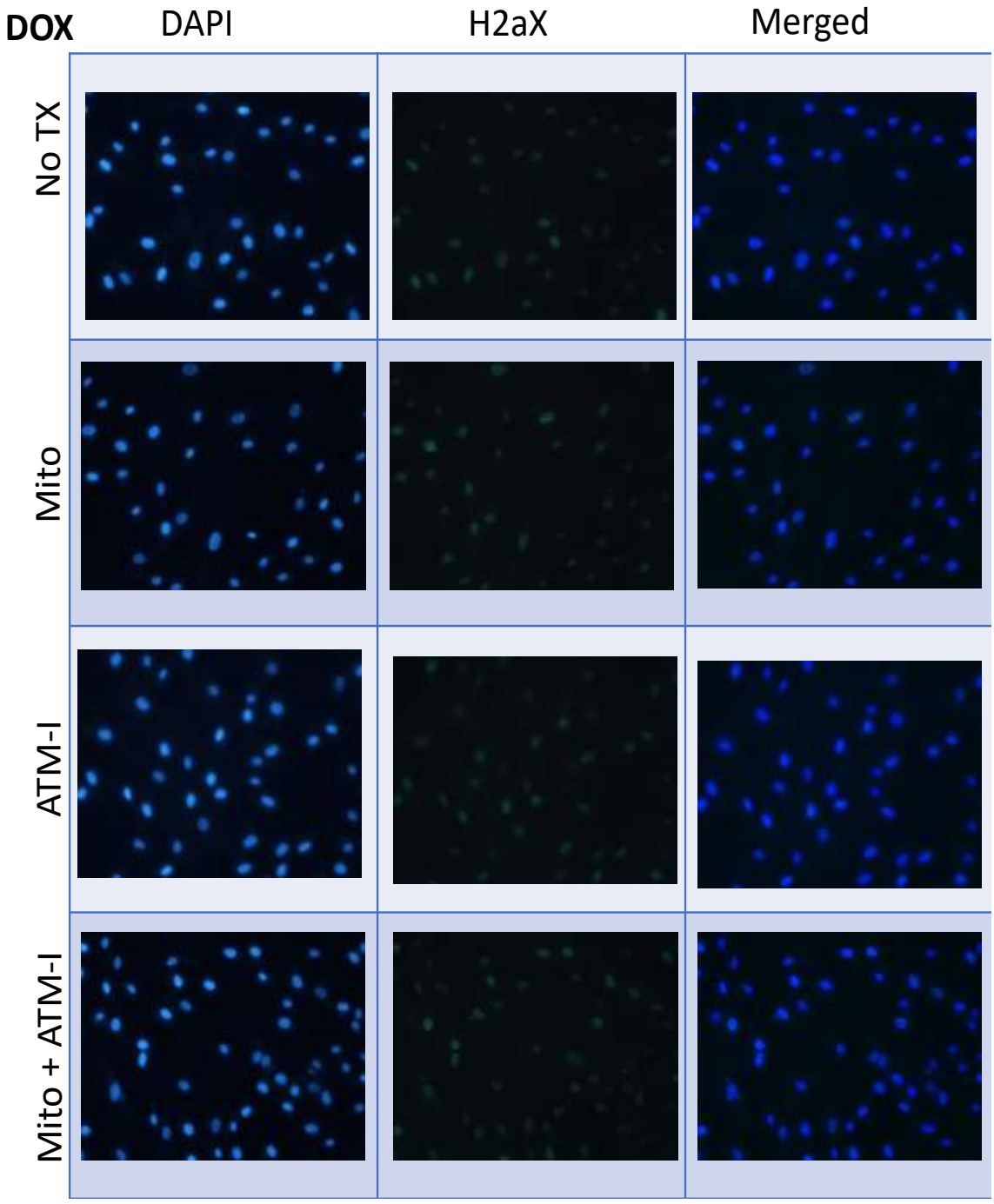

Figure 53: Representative IF images of Doxorubicin treated ECs H2A.X expression with different treatment groups

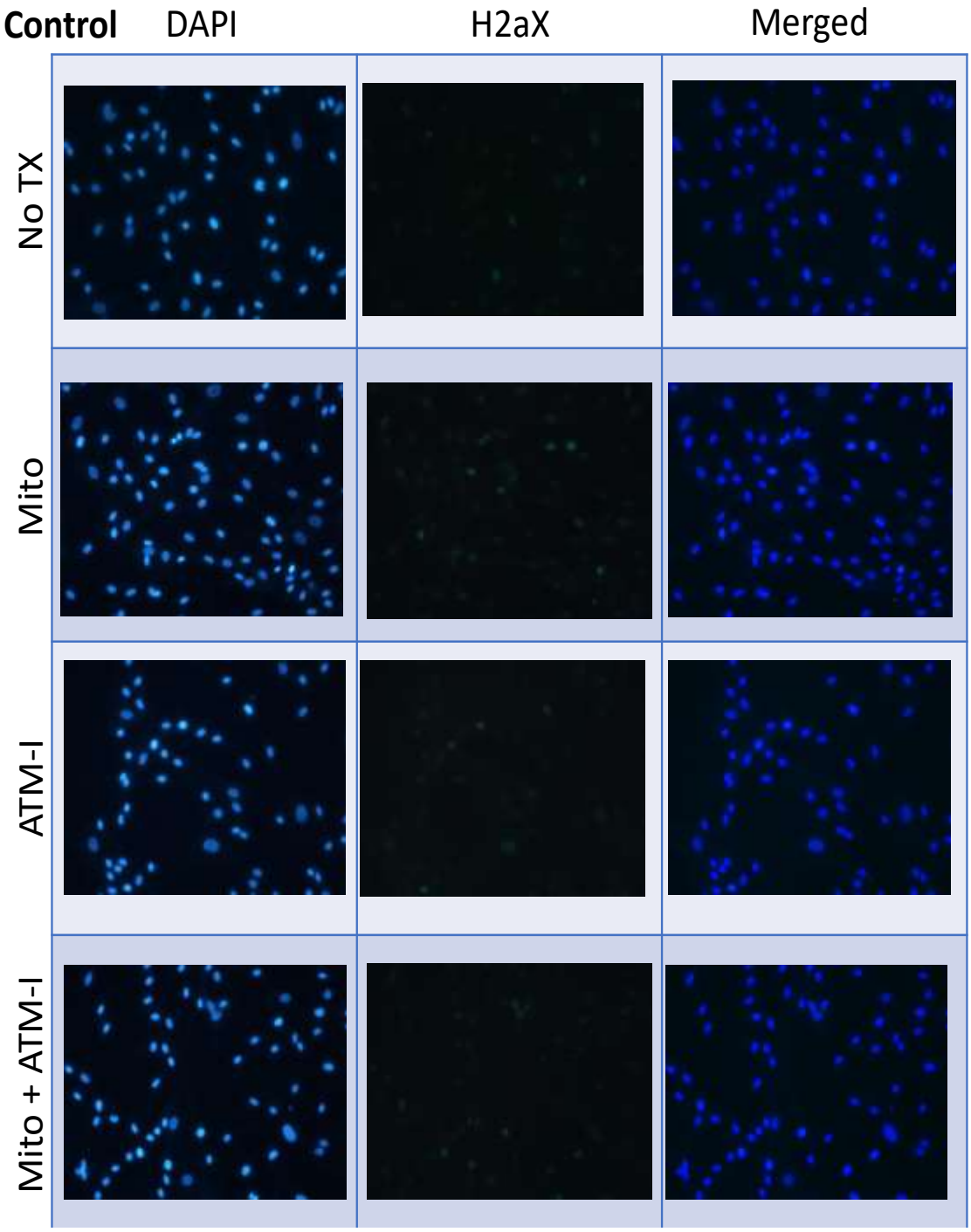

Figure 54: Representative IF images of control SMCs H2A.X expression with different treatment groups

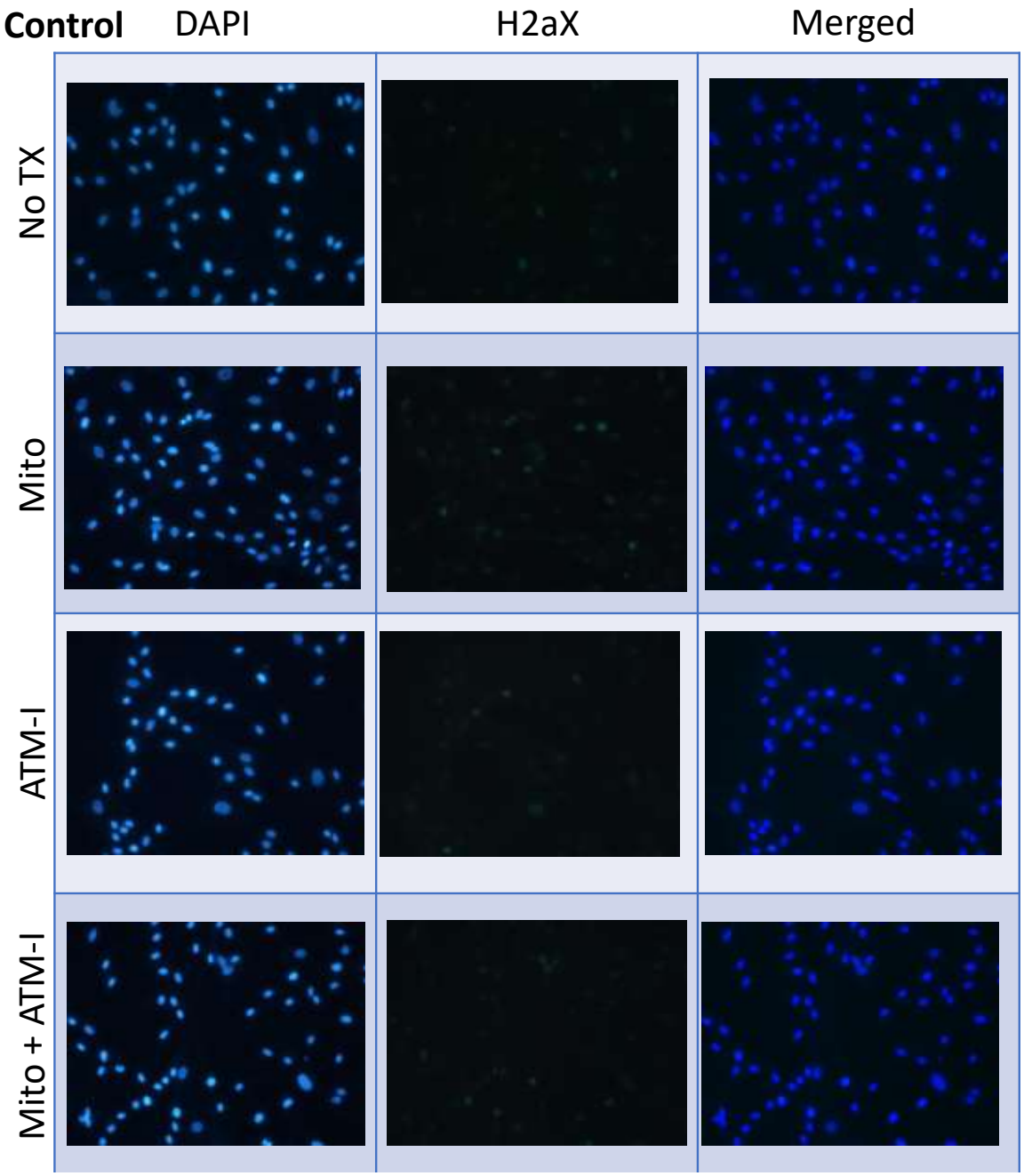

Figure 55: Representative IF images of Doxorubicin treated SMCs H2A.X expression with different treatment groups

4.3.5 Changes in P53BP staining with Doxorubicin, mito-TEMPO and ATM-Inhibitor

The same experiment as above was repeated with P53BP staining to confirm these findings. The only major difference was related to the mito-TEMPO treated cells showing a statistically significant decrease in P53BP expression, where that was not the case with H2A.X (Figure 56). The other findings were consistent among the two.

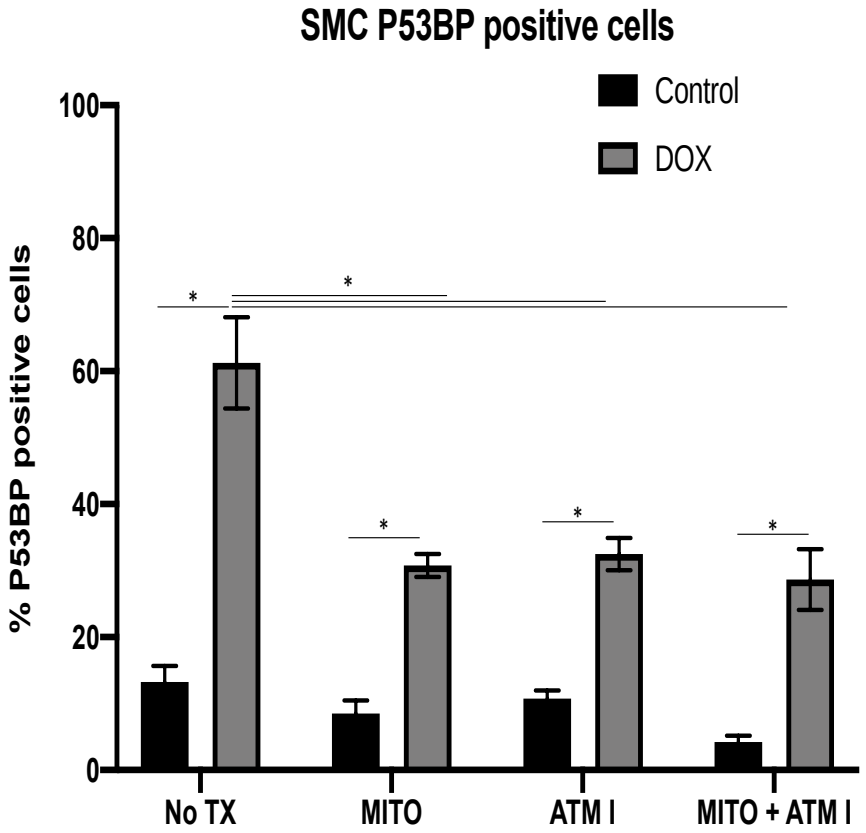

Figure 56: Changes in P53BP in SMCs with vs without Doxorubicin and ATM-Inhibitor. Cells were pretreated with ATM-Inhibitor 24 h prior to Doxorubicin exposure, and were then fixed and stained 24 h after

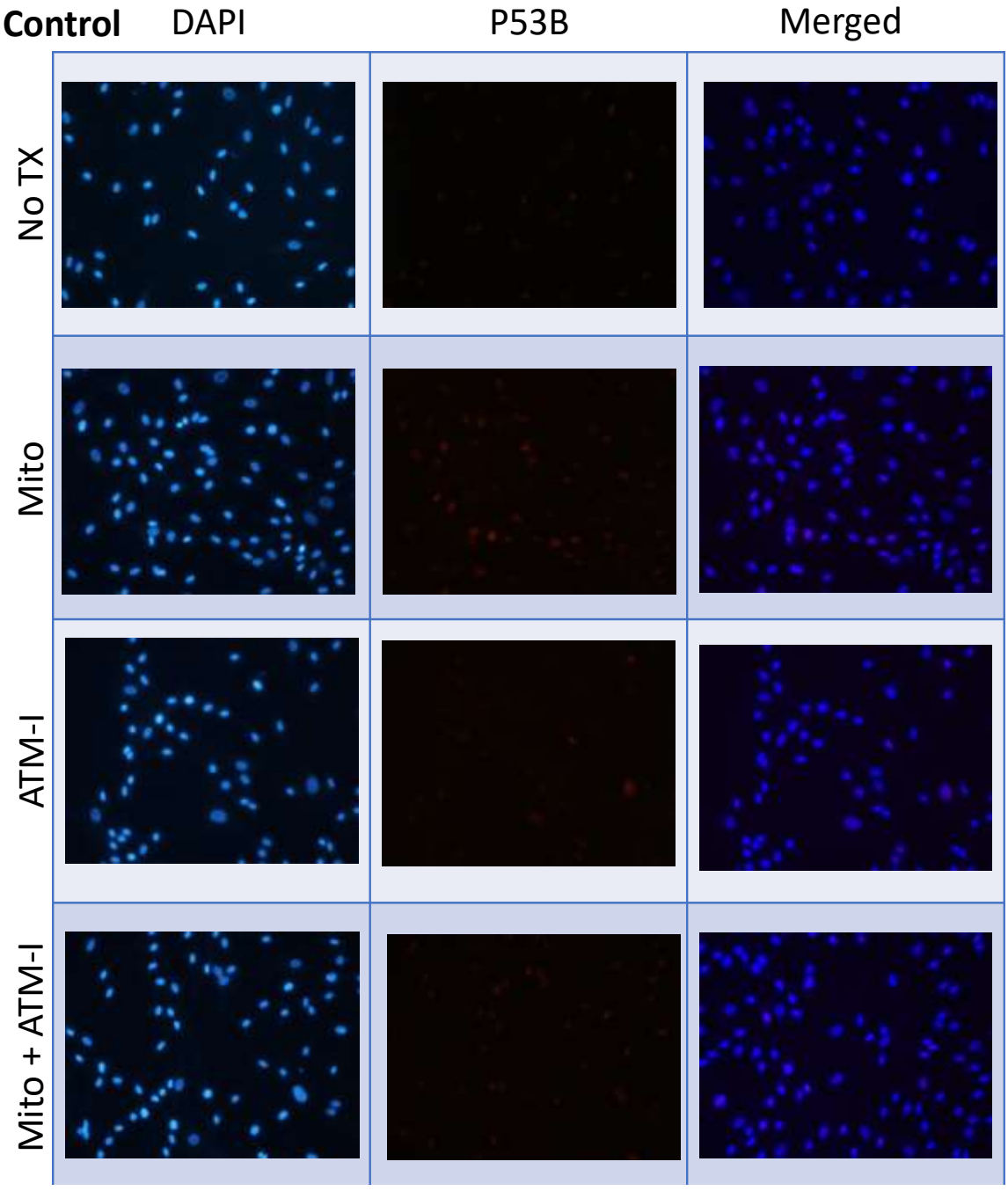

Figure 57: Representative IF images of control SMCs P53BP expression with different treatment groups

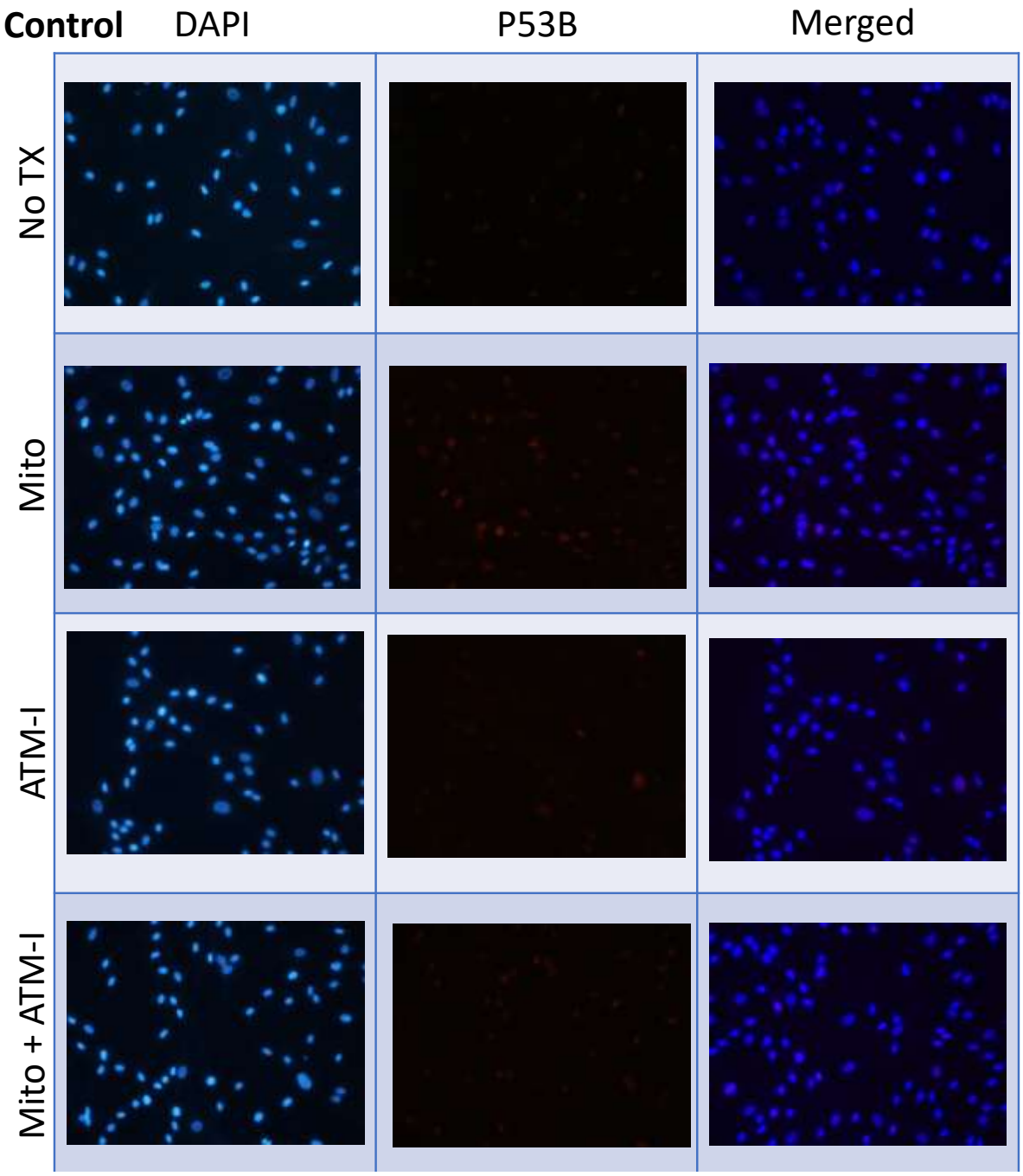

Figure 58: Representative IF images of Doxorubicin treated SMCs P53BP expression with different treatment groups

4.3.6 Changes in p21 Expression with Doxorubicin administration

As previously discussed, IR causes a number of different cellular derangements, and damage through a direct and indirect pathway. In an effort to work with a positive control to the radiation experiments, and to further provide insight into the downstream effect of double stranded DNA damage to vascular cells, we performed a set of experiments using Doxorubicin. Doxorubicin is a commonly used chemotherapeutic agent and belongs to a class of chemicals known as anthracyclines. Doxorubicin works primarily by causing DNA breaks. This is done as it intercalates into the DNA causing the inhibition of topoisomerase that leads to changes in chromatin structure, and failure of the DNA double strand to recombine, and thereby causing double stranded breaks[65,202–206207]. Furthermore, another reason for choosing this specific drug, is that in patients treated with Doxorubicin, one of the important side effects is cardiovascular toxicity.

In a recent high profile publication, Doxorubicin was demonstrated to induce high levels of cellular senescence after 24 h of treatment[208]. Therefore, the same dose and exposure times were used for the following studies, Doxorubicin (Sigma-Aldrich, D1515) was used to induce senescence at 50 nM.

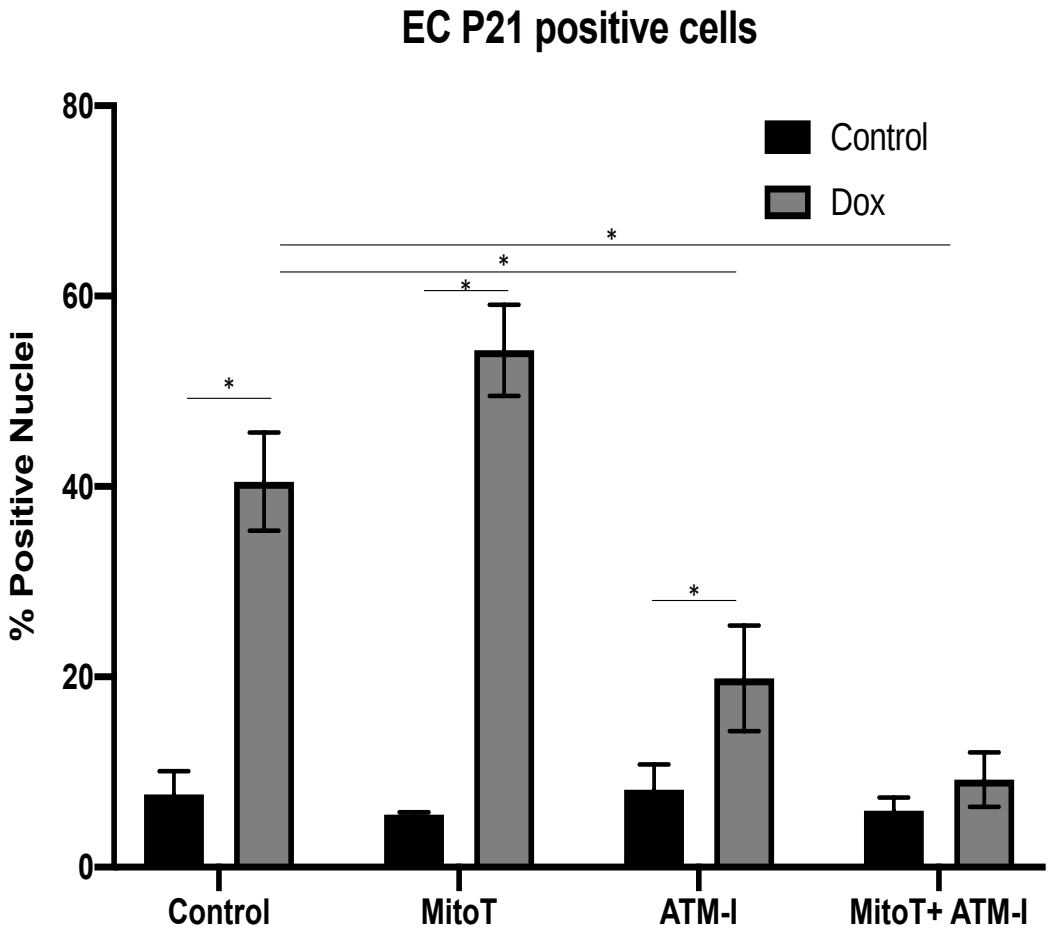

Figure 59: Changes in p21 expression in ECs with vs without Doxorubicin and ATM-Inhibitor. Cells were pretreated with ATM-Inhibitor 24 h prior to Doxorubicin exposure, and were then fixed and stained 24 h after

The expression of p21 was significantly increased after Doxorubicin treatment. For the control cells, 24 h of treatment lead to an increase from below 10% to over 40% of all cells expressing p21 ($p<0.01$). Cell treatment with mito-TEMPO did not appear to change p21 expression, however, the use of the ATM-inhibitor (ATM-I), lead to a significant decrease in p21 expression. This is evidence to suggest, that DNA breaks caused by Doxorubicin lead to the detection by ATM and likely activation of p21, likely

through p53 phosphorylation. Of note, the combined treatment using mito-TEMPO and ATM-I eliminated the difference in p21 expression between the control and Doxorubicin treated cells.

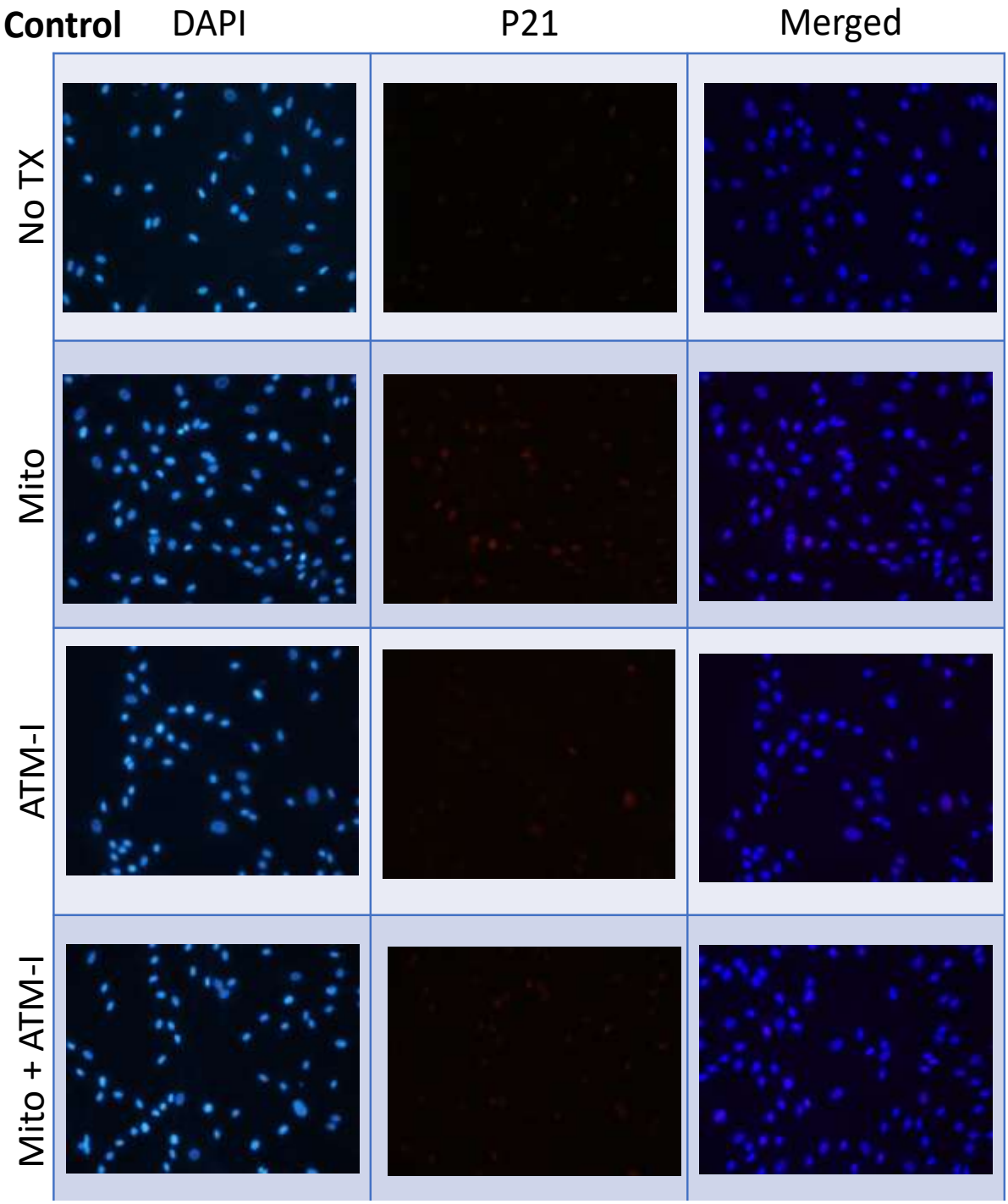

Figure 60: Representative IF images of control ECs p21 expression with different treatment groups

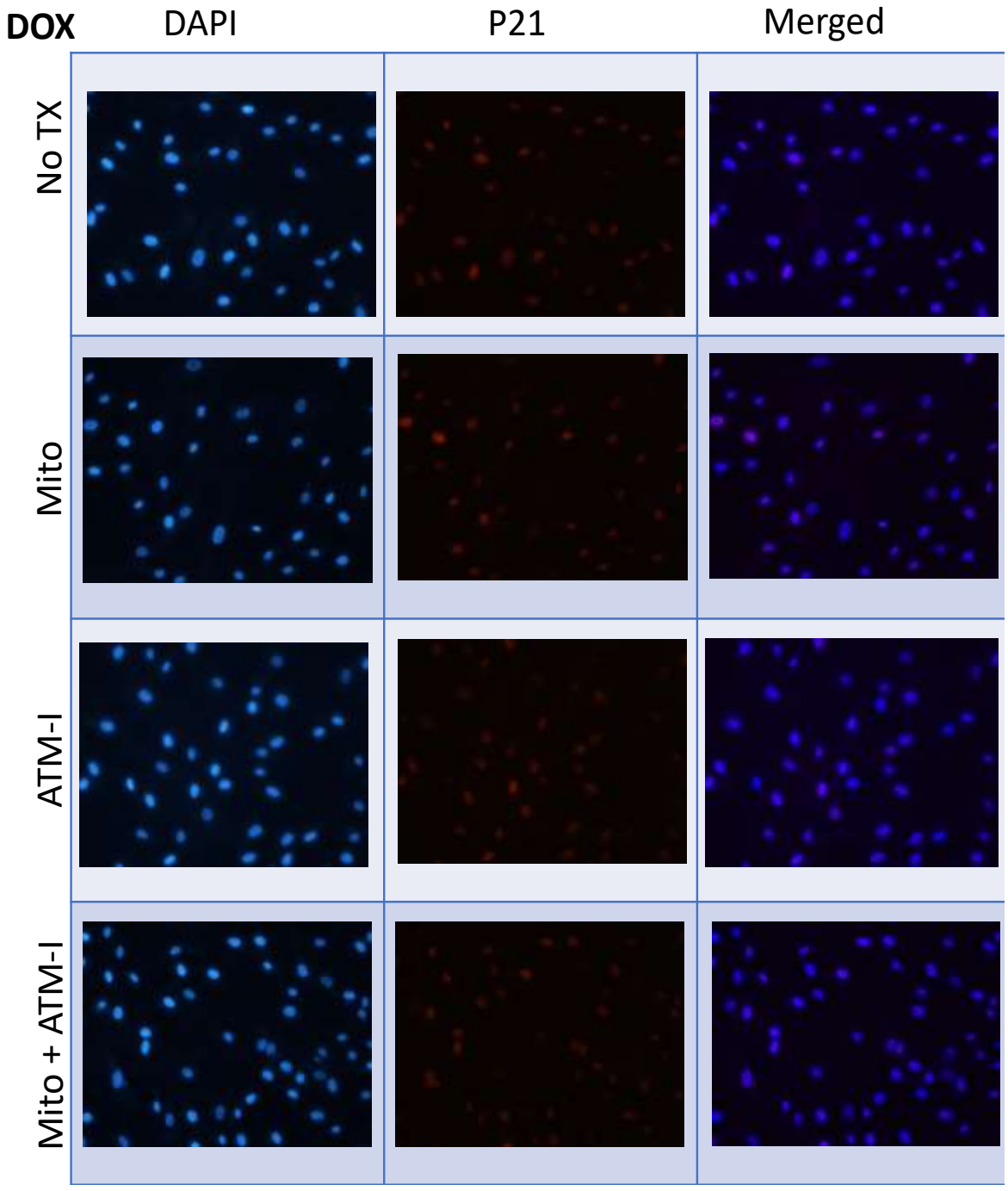

Figure 61: Representative IF images of Doxorubicin treated ECs p21 expression with different treatment groups

The same set of experiments were repeated using coronary artery smooth muscle cells (CASMC). The overall findings were similar, however, Doxorubicin treatment was associated with significantly more p21 expression in SMC than ECs (Figure 62). At baseline, less than 10% of cells were positive for p21 expression, which was increased to nearly 90% after 24hr treatment with Doxorubicin. Interesting, the addition of Mito-TEMPO lead to a statistically significant increase in p21 levels in the control cells. This was an unanticipated result, and a negative effect of this drug that has not been characterized. Inhibiting ATM activity, lead to a decrease in p21 expression after Doxorubicin treatment, with no increased expression of p21 seen for control cells.

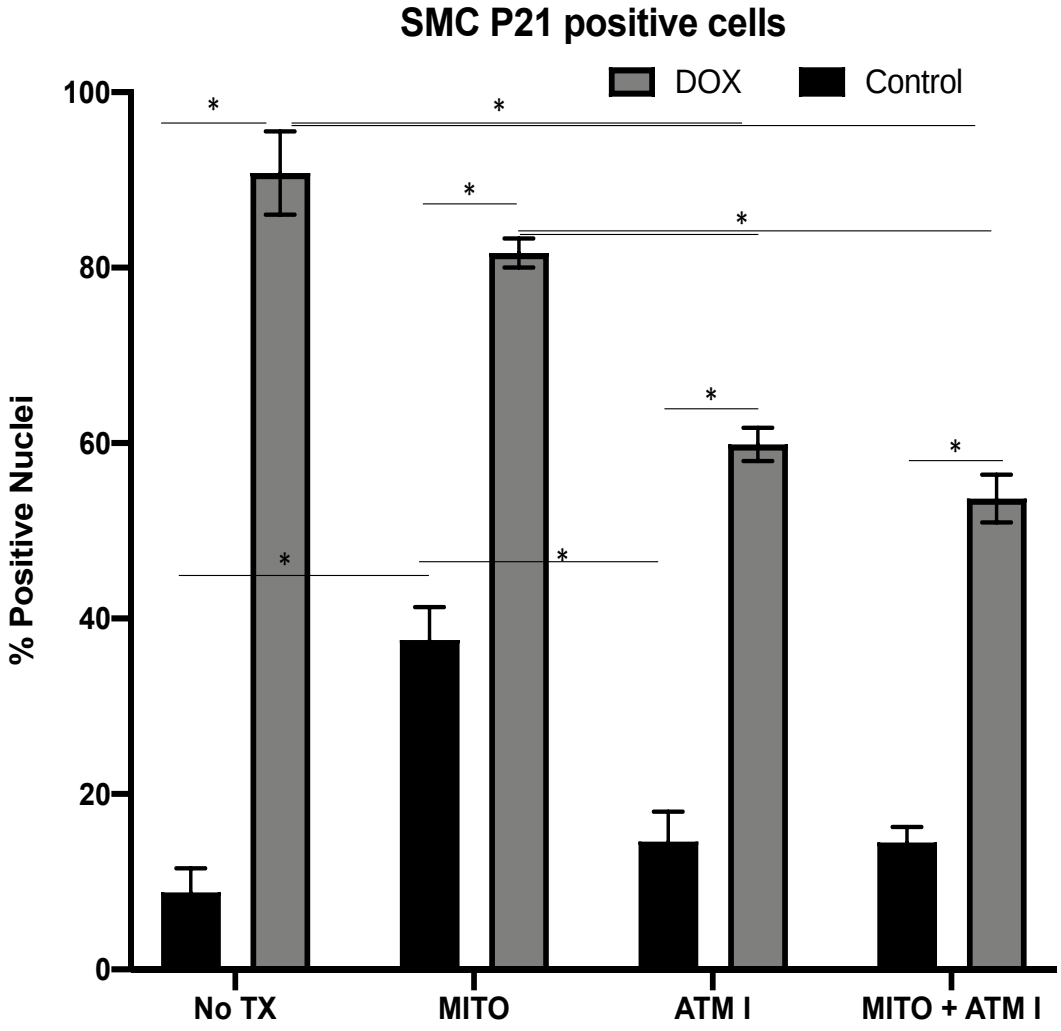

Figure 62: Changes in p21 expression in SMCs with vs without Doxorubicin and ATM-Inhibitor. Cells were pretreated with ATM-Inhibitor 24 h prior to Doxorubicin exposure, and were then fixed and stained 24 h after

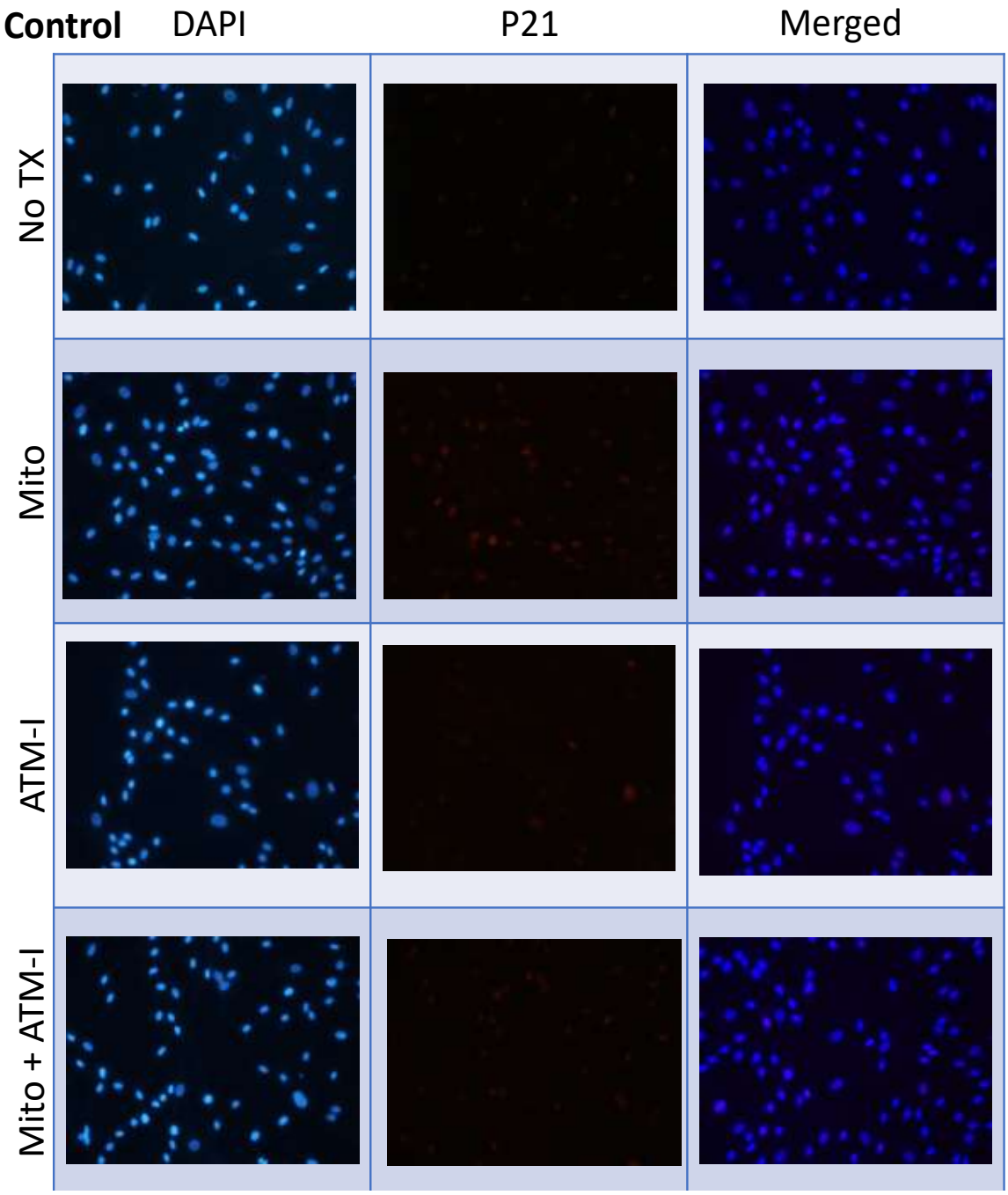

Figure 63: Representative IF images of control SMCs p21 expression with different treatment groups

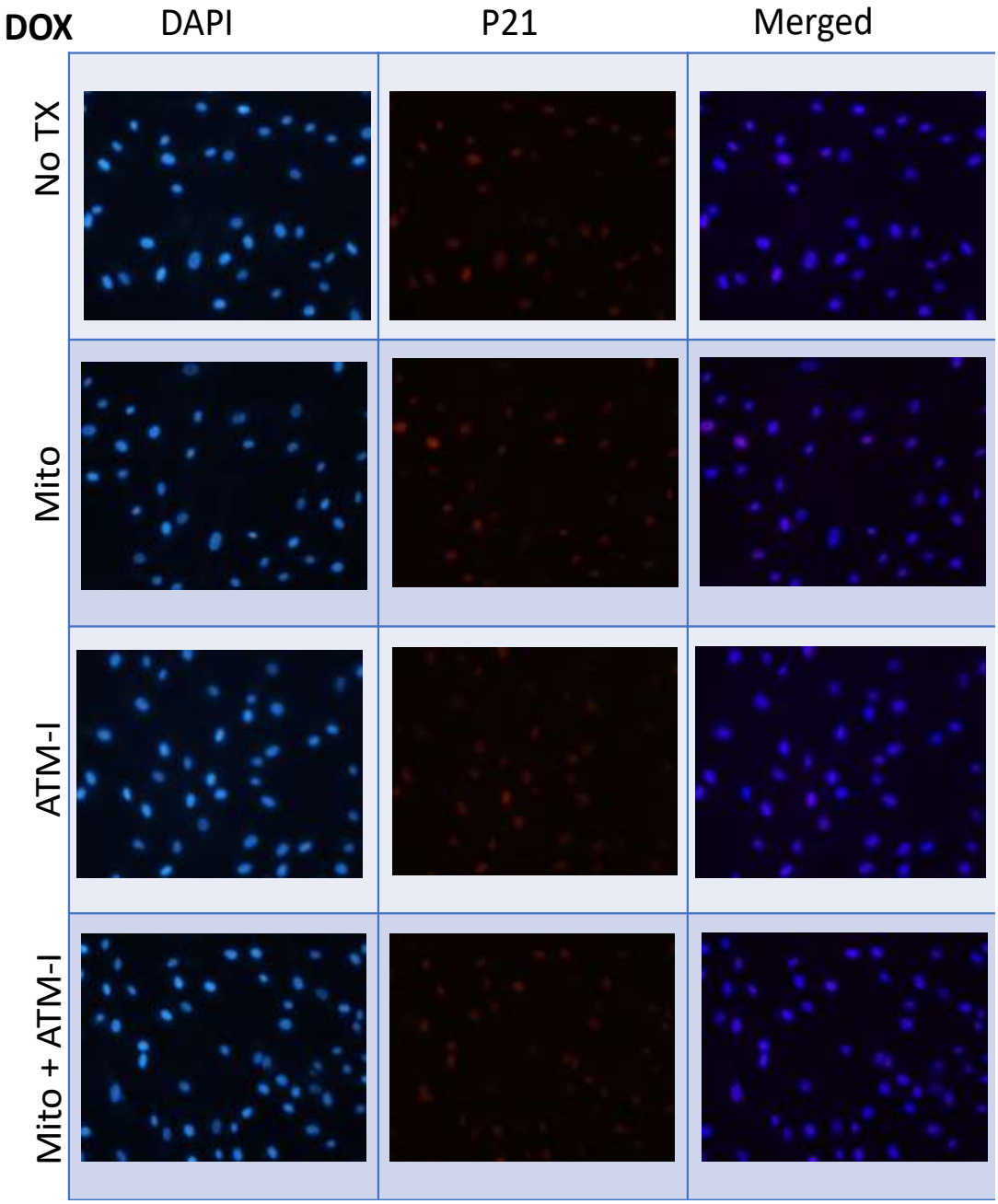

Figure 64: Representative IF images of Doxorubicin treated SMCs p21 expression with different treatment groups

4.3.7 Changes in p21 Expression with radiation and mito-TEMPO

The same experiments as above were repeated using 5 Gy of radiation and mito-TEMPO treatment. As expected, there was a drastic increase in p21 expression 24 h after radiation exposure for both ECs and SMCs that was statistically significant ($p<0.01$, n=9-12 replicates). However, mito-TEMPO treatment only seemed to decrease p21 expression in ECs and not SMCs. This was an interesting finding given that for Doxorubicin, mito-TEMPO treatment did not have an effect. This may implicate mROS generation as an important sequala of radiation damage, that is not as important for Doxorubicin induced senescence.

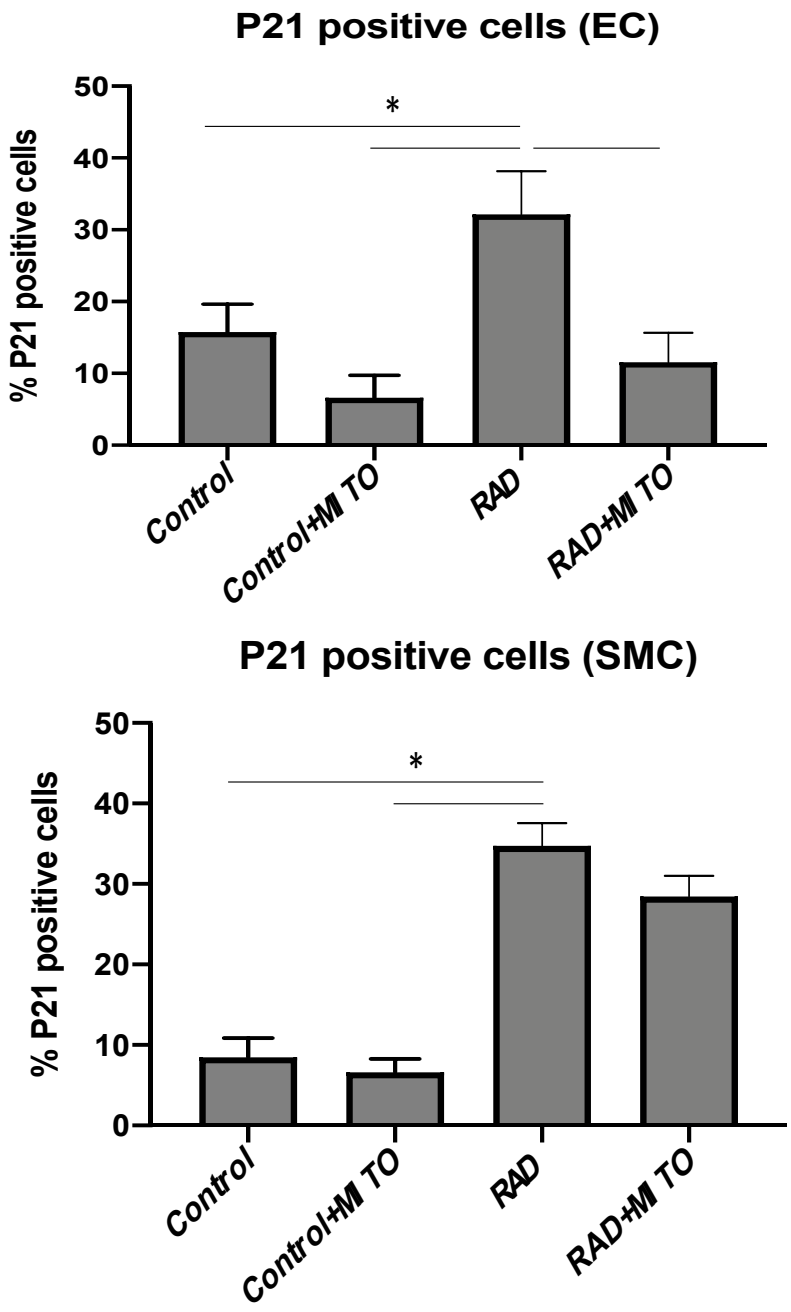

Figure 65: Changes in p21 expression in ECs (top panel) and SMCs (bottom panel) after radiation with mito-TEMPO treatment. Cells were pretreated with mito-TEMPO 24 h prior to x-ray exposure, and were then fixed and stained 24 h after

4.3.8 Changes in p21 Expression with radiation and ATM-Inhibitor

The same set of experiments were then repeated looking at the effect of ATM-inhibitor treatment on p21 expression in ECs and SMCs. Cells were pretreated with ATM-Inhibitor 24 h prior to radiation, and then they were radiated with 5 Gy, and

examined at 24 h after.

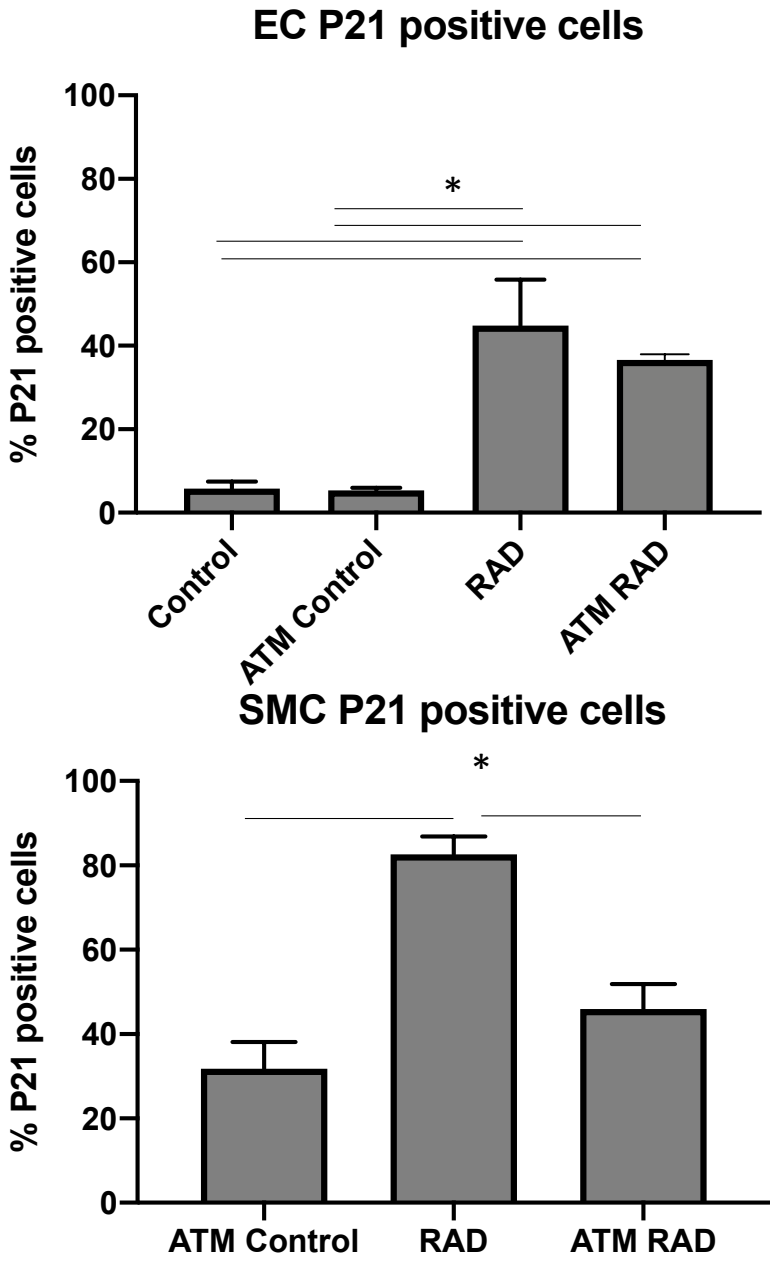

Figure 66: Changes in p21 expression in ECs (top panel) and SMCs (bottom panel) after radiation with ATM-Inhibitor treatment. Cells were pretreated with ATM-Inhibitor 24 h prior to x-ray exposure, and were then fixed and stained 24 h after

With the EC experiment, there was an increase in p21 expression after radiation, however, there was more variability among replicated as can be seen by the wider SEM margin (Figure 66). With ATM-inhibitor treatment, the decrease in p21 expression was not statistically significant. For the SMC experiments however, the use of ATM-inhibitor appeared to have a statistically significant decrease in p21 expression. This is a confirmatory finding of the ability of the inhibitor to block ATM expression after radiation induced DNA damage.

4.3.9 Changes in mitochondrial density with Doxorubicin treatment

Mitochondrial density was measured for SMC after Dox treatment (n=6 for control and n=6 for Dox). This was done by fixing the cells 24 h after Doxorubicin treatment using a mitochondrial antibody (Novus NBP1-92120, 1/1000 dilution). The cells were also stained for DAPI, and the mitochondrial florescence was indexed to the number of nuclei (corrected expression).

As can be seen in Figure 66, there is a statistically significant increase in mitochondrial density, which is a surrogate for mitochondrial biogenesis[48,159,209] after Doxorubicin treatment. This has been a recent topic of interest in the research community as new evidence has emerged to the importance of nuclear-mitochondrial signaling (NM signaling) as an important regulator of cellular health in a number of diseases[210].

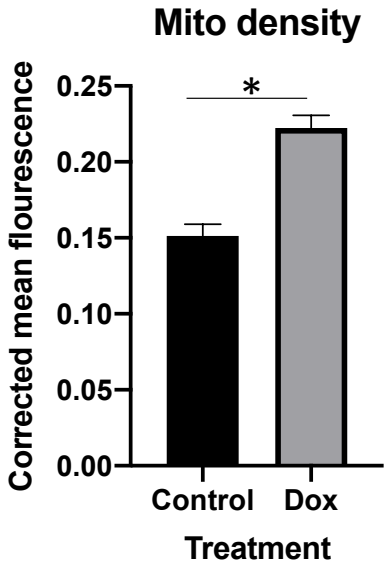

Figure 67: Increase in mitochondrial density after 24 h of Doxorubicin treatment

4.4 Discussion

In this part of the thesis, we performed a number of experiments using human primary coronary artery endothelial cells (ECs) and smooth muscle cells (SMCs) to investigate changes in the DNA damage response to radiation and Doxorubicin treatment. There has been a scarcity in the literature of using these healthy, clinically relevant cell types to studying the early normal vascular response to IR and DNA damage. As expected, both radiation and Doxorubicin lead to important increases in ATM and H2A.X activity in both ECs and SMC. We also demonstrated the effectiveness of our ATM-inhibitor in blocking ATM activity, to levels similar to those of non-irradiated cells. Low levels of both markers were detected for both ECs and SMCs in the control conditions, which is consistent with low level activity during normal cellular processes including mitosis.

Data generated in this part of the dissertation supports the hypothesis that mROS activity serves an important role in vascular cell senescence early after radiation exposure. First, we demonstrate that both IR and Doxorubicin are associated with significant increases in p21 expression early after exposure. The response was much stronger in SMCs, where 80-90% of these cells express this senescence marker. For both cell types, Doxorubicin-induced p21 expression was not affected by mito-TEMPO treatment. This is likely due to the fact that Doxorubicin acts directly on the DNA causing double stranded breaks, followed by ATM mediated P53 activation that

eventually leads to p21 activation , a process that is not dependent on ROS generation to cause secondary DNA breaks[32]. For the irradiated cells however, mito-TEMPO was associated with more than a 50% decrease in p21 activity in the ECs , and a small trend that was not statistically significant for the SMCs. This supports our hypothesis that mROS plays an important role in initiating cellular senescence in healthy endothelial cells after radiation exposure. Future experiments will need to evaluate longer term p21 expression, where the drug can simply be delaying p21 activation, rather than decreasing it. Importantly, recent evidence suggests, at least in tumor cells, that early p21 activity, might not be directly associated with long term cellular senescence. This finding has not been evaluated for normal vascular cells[208].

One curious observation is that for control SMCs that were treated with mito-TEMPO, we saw an almost statistically significant doubling of their p21 expression. This was not an expected finding which might be due to issues related to drug dilutions, SMC response to mito-TEMPO or the drug source. After re-examination of our experimental notes, the same vial of mito-TEMPO was used for the EC and SMC experiments, and therefore the result remains puzzling. It is important to note however, that there has been a large level of variability of the reported mito-TEMPO dosing used by different reports, with variability ranging from 2uM[211] to 200uM[212]. For our experiments, ECs and SMCs were treated with 3 μM. As a follow up, experiments to define safe and effective doses that are specific to ECs and SMCs might be required. It is

important to note, that completely blocking mROS signaling might be harmful to cells, given that it is an important signaling molecules during normal cellular hemostasis[213]. Different cell type therefore, might require unique mito-TEMPO dosing. However, for clinical translatability, a uniform dose must be found, that has the least side effect profile, but still has reasonable efficacy. This is likely achievable as there has been in vivo animal studies showing safety and efficacy of this drug[214].

Inhibiting ATM activity appeared to have a profound effect on H2A.X, P53BP and p21 expression. This was an expected result, given that ATM is an upstream activator of these markers directly, or indirectly.

Future experiments will focus on two lines of investigations as a follow up to these results. First, it will be important to study the link between DNA damage and mROS production in ECs and SMCs. Recently, SIRT6 was shown to be an important regulator of DNA repair following oxidative damage[215], therefore SIRT6 expression levels with vs without mito-TEMPO pretreatment with radiation will be studied. The second area of investigation will be the long-term consequence of these treatment strategies. Cellular senescence after DNA damage plays an important protective role to the organism as a whole in limiting faulty DNA replication and tumor development. Therefore, strategies to decrease cellular senescence despite DNA break formation (ie ATM-inhibition) might actually be harmful in vivo. However, mito-TEMPO based experiment, in essences decrease over production and over activity of mROS, such as

seen in the radiated ECs. Additional analyses of endothelial activation after exposure to IR with or without Mito-TEMPO will be conducted in 3 distinct ways: (1) increased activation of surface markers, (2) increased endothelial permeability (TEER Transwell plate measurement) and adhesion of leukocytes. Increased expression of surface markers (VCAM, ICAM and E-Selectin) will be assessed using flow cytometry. Expression levels will be compared between an escalating XRAY dose (1Gy, 3Gy, and 5 Gy), a negative control (with no radiation exposure) and a positive control (4.5 h incubation of TNF-alpha at a concentration of 100 U/ml for 4.5 h). Importantly this experiment will be repeated with vs without Mito-TEMPO treatment. The p21 expression experiments will be repeated and H_2O_2 will be used as positive control since I have preliminary data (not shown) showing that H_2O_2 exposure increases p21 expression. Finally, new recent assays allow for testing for mitochondrial specific DNA breaks, and these will be performed with the same above conditions[216].

4.5 Conclusions

In this part of the dissertation, we provide evidence to support the hypothesis that IR causes early increases in cellular senescence for healthy ECs and SMCs. While these changes are secondary to direct DNA damage activation of the ATM-P53-P21 pathway, there appears to be a role for mROS activation and release that can be mitigated by decreasing mitochondrial ROS.

5. Future work

Current studies looking at health effects of radiation exposure are limited to (a) epidemiological case controlled cohorts (b) animal studies and (c) cell based studies using cells in a static plate or in a few studies using cells in a 2D flow chamber. Epidemiological studies rely on dose estimation at the time of exposure, are limited by many confounders, and the inability to elucidate mechanisms of disease. Animal studies are limited by the differential response to animals to radiation exposure and the applicability of the findings to humans[217]. Finally, 2D cell-based studies lack the ability to evaluate physiology, and control for important factors such as physiologic flow. This is especially true when studying the endothelium given the vital role sheer stress and flow play in endothelial response[76,148]. Micro-physiological systems (MPS) bridge this translational gap between animal in vivo data and human effect [218,219,220]. A three-dimensional (3D) tissue engineered blood vessel (TEBV) model allows for the evaluation of human biology with its complex interactions between physiological flow, multiple cell types, extracellular matrix and ability to respond to self-produced vasoactive stimuli such as Nitric Oxide (NO).The Truskey lab developed a method to rapidly construct functional TEBV with a confluent endothelial layer and a smooth muscle layer. These TEBVs allow for multiple, regular non-destructive monitoring of effects over time within the same vessel as compared to controls. This is especially important when studying delayed effects of radiation exposure. For instance, endothelial reserve for vasodilation

is an important prognostic predictor of vascular health and future events. In the TEBV model, acetylcholine administration leads to vasodilation that can be measured over time and compared between normal vs dysfunctional endothelium.

Over the last two years we have been modifying the system as can be seen in the figure below (Xu, Bishawi et al. under review). We have also made adjustment to allow it to be used for radiation experiments. The modified system allows for the creation of 4 vessels at a time (A), and the ability to perform multiple layers (EC, SMC, and fibroblasts), (B, C, D, E). The media volume has been signifianctly decreased, allowing for better sampling of released factors such as NO and ROS.

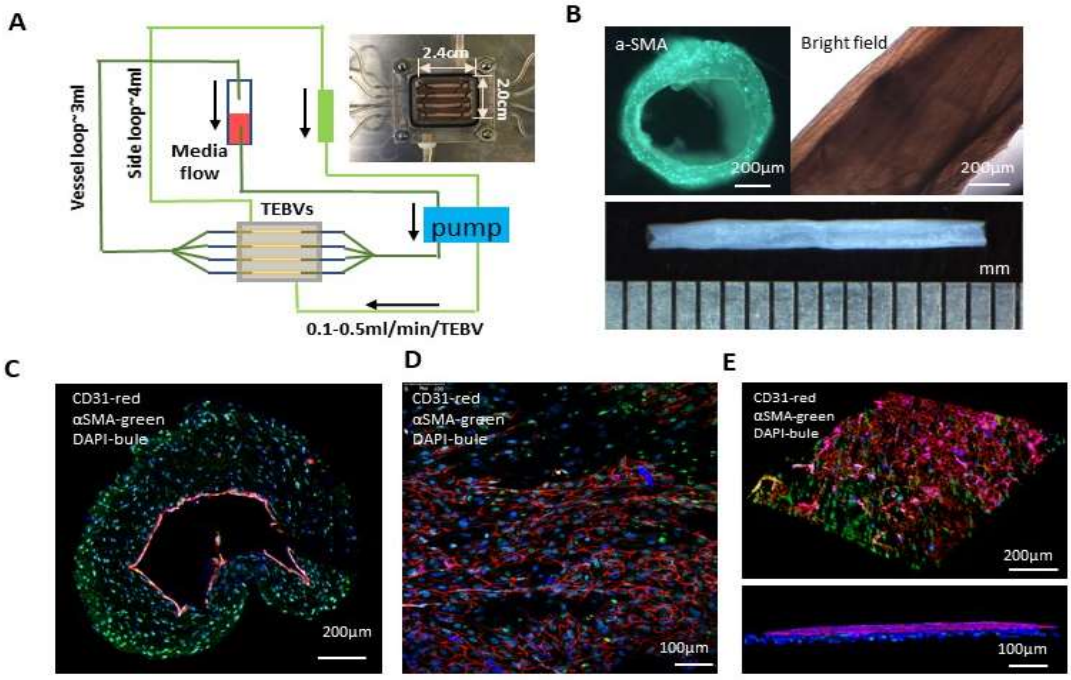

Figure 68: New TEBV system. collagen based tissue engineered blood vessels are fabricated and perfused (A, B). The cells are endothelized and demonstrate good

endothelial cell and smooth muscle cell or fibroblast density starting at 1 week after perfusion (C, D, E)

This system will therefore be used to study the local endothelial response to radiation, and leukocyte adhesion with physiological flow conditions. The endothelium is highly dependent on flow where disturbances in flow alone may cause endothelial activation and damage[221]. Overall, there is a scarcity of data looking at endothelial activation and mononuclear cell adhesion after radiation exposure under physiological flow conditions. There are two important aspects of leukocyte adhesion to the endothelium, (a) overall leukocyte concentration in circulation, and (b) leukocyte recruitment by the local endothelium[222]. The process of adhesion itself is broken down into leukocyte rolling, firm adhesion, and eventual transmigration. All studies related to leukocyte adhesion have been limited to 2D static cultures and a few with 2D flow chambers[173]. These results will further extend the results from aim 2 by combining the effects of ECs with SMCs, and adding the important element of physiological flow which is a more realistic simulation of *in vivo* conditions.

All TEBVs will be fabricated according to the protocol developed in our lab[218]. Collagen gels will be embedded with human coronary artery smooth muscle cells and perfused under physiological conditions. Next, the TEBV lumens will be endothelialized with human coronary artery endothelial cells. Baseline vasoactivity measurements will be done using 1 μM phenylephrine and acetylcholine. Measurements of molecules in the media (NO, LDH, H_2O_2, caspase activity) will be done by removing a sample from the

media in the perfusion chamber (similar to what was done in Aim 2). I have previous preliminary data demonstrating the TEBVs response to radiation in our old system. We will test a dose between 2-6 Gy and use endpoints of 24 h, 3 day, 7 day and 2 weeks. We will also perform RT-PCR to examine changes in the expression of VCAM-1, E-selectin, NOS III, KLF-2, NRF2, NQO1, HO-1, and GRP78. We will use 4 TEBVs per condition. The statistical analysis will be like that performed with the ECs.

The system will then be used to test the theraputic role of mito-TEMO, and ATM-inhibitor similar to the previous chapeter. This will be important, as it will address some of the limitations discussed in that chapter related to the long term effect of these treatments.

6. Conclusion

The overall hypothesis of our studies was that Ionizing Radiation (IR) is associated with early vascular and cardiac damage that has important implications for long term cardiovascular dysfunction. In the first part of this work, we evaluated the effect of low LET and high LET radiation and their role in long term cardiovascular function using an animal model of whole body radiation. We found important changes to both arterial elastance and a number of load dependent and independent measures for mice that were exposed to galactic cosmic rays (GCR).

In an effort to better understand the differential contribution of the cardiac vs vascular system to this phenotype, we carried out a set of experiments in

cardiomyocytes and in relevant vascular cells (ECs and SMCs) to better understand the effect of radiation in those specific cells. Using a cardiac patch system, we demonstrated that radiation cause a trend towards changes in cardiac function early at 24 hr, that was not statistically significant. However, even at doses as low as 0.1 Gy, cardiomyocytes had important changes in their proteome with strong involvement of mitochondrial proteins associated with mitochondrial dysfunction.

Repeating the same experiments in ECs and SMCs, we demonstrate early changes to the cellular senescence pathway after different radiation scenarios that may have important implications to future vascular health. These changes can be somewhat mitigated with mito-TEMPO treatment to block mROS specifically. We identified the DNA damage repair system as a master regulator of these changes, driven primarily by ATM.

Future work will focus on better understanding the long term effect of these changes by using our recently modified TEBV system. This will allow us to test the effect of this early senescence on vascular functional parameters short and long term. It will also allow us to perform these experiments under physiological flow conditions.

While this work has led to more questions than answers, it does highlight that in healthy cardiac and vascular cells, low to medium doses of IR are associate with important cellular derangements with functional consequences. These findings have

important implications for human health given the environment of increasing radiation exposure terrestrially and as part of renewed interest in deep space exploration.

Appendix A

Transthoracic Echocardiograms- TTE

All TTEs were performed at the Duke CVRC. The following is the protocol used.

Restraint:

Awake animals are briefly restrained by hand to (1) remove chest or abdominal hair by either a clipper or depilatory cream and (2) perform an echocardiogram. Total restraint time may last up to 10 minutes. Ultrasonic gel and/or 70% ETOH may be applied at the discretion of the operator on the imaging surface to enhance image quality. If depilatory cream is used it is promptly cleaned off skin within 3 minutes by wet paper towels. It has been our general practice to perform the hair removal at least a day prior to decrease the stress on the animal during the TTE.

Echocardiography:

Echocardiography is performed on conscious mice. Animals are gently restrained by hand while an echo transducer is externally applied to the chest. Images are acquired using an echocardiograph machine. If all required images are not acquired within a 10 minute total time period, the mouse is given a rest period of 20-30 minutes before another attempt is made. If at any time during the experiment the animal exhibits signs pain or distress such as labored breathing, cessation of respiration or twisting physical movements, the session is terminated. If the animal does not fully recover within the 30

minute rest period or shows signs of continued respiratory distress the mouse is euthanized or a veterinarian is called/paged.

Pressure Volume Loop Assessment

Animal preparation: Hair will be removed over the surgical site by clippers or with depilatory cream. The skin is prepped with a single Chlorhexidine or Alcohol scrub (the percentage will be approximately 4%/70% depending on the vendor. Current Vendor is Steris Bactoshield CHG 4% Surgical Scrub).

Anesthesia/Endotracheal intubation:

Adult mice are hand restrained and anesthetized with either: (1) an IP injection of Ketamine/Xylazine (100 mg/kg Ketamine and 2.5 mg/kg Xylazine) or (2) induction with 2-5% Isoflurane gas administered by a nose cone or induction box and then maintenance of anesthesia through a nose cone or endotracheal tube with 0.5%-5.0% (average 3%) Isoflurane. Animals that receive Ketamine/Xylazine may be supplemented with 0.5%-5.0% isoflurane through a nose cone or endotracheal tube if needed to maintain a surgical plane of anesthesia. Animals that receive isoflurane may receive Ketamine/Xylazine as an adjunct anesthetic to improve the quality of the PV loop recordings. The use of Ketamine/Xylazine as an adjunct will be determined by PI preference or by the Core staff in instances where the PI has not specified.

Animals may receive endotracheal intubation via oropharynx intubation with a blunt 20-gauge needle to serve as the tracheal cannula. A mid-line cervical incision is made to expose the trachea and allow for direct visualization of the trachea for accurate placement. After endotracheal intubation, the cannula is connected to a volume cycled rodent ventilator with a tidal volume of 0.2-0.5 ml and respiratory rate of 90-130 breaths /min depending on the respiratory status of the animal. Verification of placement and adequacy of ventilation is determined through visual inspection of chest expansion. The jugular vein and carotid artery is exposed via the mid-line cervical incision and a bilateral vagotomy may be performed.

The policy for "Safe Use of Anesthetic Gases" will be followed. Prior to chest incision, anesthesia is confirmed by pinching the toe and ensuring there is no response. The level of anesthesia is continuously monitored throughout the entire procedure by the operator(s) to ensure the animal is maintained under a surgical plane of anesthesia. This includes monitoring for spontaneous movements or blinking and visual observation of respiratory effort. In addition, heart contractions will be monitored during thoracic procedures. A heating pad (i.e., circulating warm water pad) is applied during the surgery and care is taken to ensure mice do not overheat or experience thermal burns.

Surgical Procedure: Mice may undergo more than one of the non-survival surgical procedures described below. The maximum amount of time a non-survival procedure will not exceed 90 minutes.

At the end of the experiment, animals are euthanized prior to recovery from anesthesia with an anesthetic overdose and exsanguination by removal of vital organs.

Records will be maintained according to the policy "Animal Record Requirements: PI and Veterinary" and guideline "Anesthetic Animal Monitoring Expectations." The materials and methods including anesthesia used will be documented in the surgical record and provided to the PI with the hemodynamic and other physiologic data acquired for the experiment.

Cardiac Contractility and Pressure-Volume Loop analysis.

Animal preparation, anesthesia, and intubation are described above. Then fluid filled PE 10 tubing is inserted into the external jugular vein for volume or drug infusion. A high fidelity Millar electronic catheter or a conductance catheter is inserted into the right carotid and advanced retrograde into the left ventricle (LV). In cases where high quality PV loops cannot be obtained from this approach, an alternative approach is used where the conductance catheter is inserted into the LV apex via a thoracotomy. In these instances, the use of LV apical approach will be documented in the surgical record and provided to the PI with the hemodynamic data for the experiment. Simultaneous LV pressure and LV volume are recorded. At the conclusion of the procedure, volume

measurements are corrected for parallel conductance (Vp). Vp is obtained by injecting IV 10ul of 15% hypertonic saline. In certain instances, cuvette volume calibration is performed by obtaining 100-200ul of whole blood through aspiration after direct puncture of the ventricle at conclusion of the experiment. Data are recorded digitally and stored on a computer for off-line analysis.

Transient Aortic and IVC constriction: To obtain load-independent measures of cardiac contractility and compliance, PV loops are obtained over a range of preload and afterloads. Preload is varied by making a laparotomy incision and briefly manually compressing the IVC to decrease preload. Afterload is varied by gently pulling a suture to transiently constrict the transverse aorta. Both IVC compression or aortic constriction are done for 10-15 beats and then released. The use of either IVC compression or aortic occlusion to alter loading conditions is decided by PI preference or by Core staff in instances where the PI has not specified loading conditions.

Blood Pressure and Pressure Gradient Measurements

Animal preparation, anesthesia, and intubation are described above. PE 10 tubing is inserted into the right carotid artery, left carotid artery or both for pressure measurement. In some instances, an axillary artery is cannulated by extending the midline incision to the left anterior axillary line exposing the axillary artery. Catheters are connected to fluid filled pressure transducers for simultaneous measurement and

recording of pressures across the transverse aorta. Calibration of fluid filled pressure transducers are routinely performed using a pressure manometer. Calibration does not involve use of animal. At the end of the experiment, animals are euthanized under anesthesia, heart is removed and tissues harvested if indicated.

Appendix B

Western Blot Protocol

Modified by Muath Bishawi (September 2018)

Modified from Biorad, TC, CR and SW Protocols

Optimized for small size proteins

Materials

- Lysis Buffer: CellLytic-M (Sigma C2978)+Protease inhibitor cocktail (Sigma P8340)
    - Or RIPA buffer
- Mini Ready Gel
    - In farthest left 4C in 1313, bottom shelf, Mini PROTEAN TGX
- Laemmli's Sample Buffer (Biorad #161-0737)
    - On shelf above western blot bench, 4X used to maximize protein loaded
- Beta-Mercaptoethanol (Biorad 161-0710)
- TBST: Dilute 10x Tris-Buffered Saline (Biorad #170-6435) to 1X with DI water and add 0.1 % Tween 20 (Biorad 170-6531) (i.e. 50mL TBS, 450mL DI water, 0.5mL Tween 20)
- Transfer Buffer: 100 mL 10x Tris Glycine Buffer (Biorad #161-0771), 700mL distilled water, 200mL methanol (if using PVDF membrane, otherwise 900mL distilled water). 20% methanol is important for small proteins
- Running Buffer: 100mL 10x Tris/Glycine/SDS Buffer (Biorad #161-0772), 900mL distilled water
- PVDF membrane 0.2uM pore size
- Fiber pads
- Filter paper
- Kaleidoscope Ladder (Biorad 161-0375)
- SuperSignal West Pico Stable Peroxide Solution
- SuperSignal West Pico Luminal/Enhancer Solution
- RESTORE Stripping Solution (21059)
- Pierce BCA Assay Kit (Pierce 23227)
- Non-Fat Dry Milk Powder
- Primary and Secondary Antibodies

- Methanol
- PBS -/-
- Eppendorf tubes
- Micropipettes
- Pipettes
- 96-well plate for BSA
- 50mL and 15mL conical tubes

DAY 1

Buffer Preparation

1. Mix ingredients together for Transfer and Running Buffers and put into labeled 1L jars. Transfer buffer can be stored in the fridge overnight.
    a. 1 L each
2. Mix ingredients together for TBST. Tween 20 is very viscous. Store in fridge overnight.

DAY 2

Protein Harvest (Can be done as cells are ready and stored in -20C)

1. Prepare Lysis Buffer (KEEP ON ICE)
    - Cell-lytic M (Add 0.5mL protease/phosphatase inhibitor cocktail to every 5mL Cell-lytic M used)
2. Carefully aspirate media from cells. The whole process should be done on ice.
3. Wash once with cold DPBS -/-
4. Add lysis buffer mix to each flask or well (~400uL/well). Keep on ice shaking for 30 minutes
5. Scrape cells with cell scraper. Keep plate tilted at all times in order to keep all the cellular debris in the lysis buffer. Pipette out all liquid and cells. Add suspension to 2.0mL eppendorf tube.
6. Spin down tubes with microcentrifuge at 12K RPMs for 20 min
7. Keep the supernant, Store in -20C.

BSA Protein Concentration Determination Protocol

1. Prepare BSA Standards as described in the manual that comes with the BSA kit, EXCEPT dilute in lysis buffer rather than PBS. (Note: The

standards can be prepared ahead of the time and aliquoted and stored at -20C.)
2. Prepare BCA indicator solution (# samples + # of samples) * (number of replicates) * (volume of indicator solution per sample) = total volume of indicator solution needed. Make the solution with 50 parts Reagent A with 1 part Reagent B (example: 2500uL Reagent A, 50uL Reagent B).
3. Add 100uL of BCA solution to each well of a 96-well plate.
4. Add 2uL of each BSA standard to the wells (do in duplicate in rows A and B of plate).
5. Add 2uL of each unknown sample to wells (do in duplicate, rows C and D).
6. Shake for 30s on plate shaker.
7. Incubate at 37C for 35 minutes.
8. Read using plate reader in 1313

Prepare Proteins

1. Use Excel spreadsheet and BSA results to calculate volume of lysate needed to get desired amount of protein (usually, 10ug-30ug).
    a. Can use anywhere from 5-20 ug.
2. In 1.5mL eppendorf tubes, add amount of DI water calculated on spreadsheet, then add protein lysate (amount specified on spreadsheet).
3. Make Loading Buffer in a separate 1.5mL tube; solution should be 19 parts Laemmli's Sample Buffer 4x, add BME. This should be added 3:1 with the rest of your protein solution (protein+water made in step 2), see spreadsheet for calculation. ADD AND STORE BME in fume hood.
    a. Put samples on heat block set at 100C for 5 minutes. Squirt DI H2O on set to help seal space between tube and set. Make sure tubes are sealed and use forceps to poke holes in top of tube so that the pressure does not build up.

Run Gel

1. During 5 minutes-Add gel to box (used 4-20% gel)
    a. Remove the green film on the bottom of the gel.
    b. Add gel to box with comb facing inward (so that you can read the numbers from the outside) (push all the way down and lock). The shorter plate faces the inside.
    c. Carefully remove comb.
    d. Add running buffer and then add to box (fill to top in inner and near top to outer).

2. Add protein samples and ladder (5-10uL for ladder, usually 30-50uL for protein samples depending on gel lane size).
    a. If you are going to cut the membrane in half for two separate antibody incubations, need to include two ladders on the gel; one for each half.
3. Run the gel at 100-200 volts initially, max current and power for ~30-45 min (until visible bands reach bottom of gel, near wire). Constant voltage.

Transfer

1. While the gel is running, soak the PVDF membrane in 100% methanol.
    a. This only needs to be done for about 5-15 minutes, or until PVDF is saturated.
    b. Cut PVDF to the same size as the fiber pads/filter paper.
    c. Take the blue covering off, and use forceps to transfer the membrane to the methanol.
    d. Be careful to keep the membrane clean.
2. Soak PVDF membrane, 2 fiber pads, 2 pieces of thin transfer/filter paper in transfer buffer right before the gel is done.
    a. Place all in transfer buffer in the clear tub with handles.
3. Take the gel out of the cassette and gently break it open in transfer buffer.
    a. Use the green blade to pry it open.
4. Pour out Running Buffer from the gel box.
5. Cut off top part of gel with green blade – remove the wells.
6. Soak the gel in transfer buffer for 15 minutes.
7. Open up the cassette (black and clear parts) and lay the black part down.
8. Put items in following order on the black part: fiber pad, filter paper, gel, PVDF membrane, filter paper, fiber pad. Roll out air bubbles with pipette after you add membrane, paper, and pad.
    a. Black is negative, red is positive. You want the proteins, which are negatively charged, to travel from the gel to the membrane towards the positive end. So the membrane always needs to be between the gel and the red (positive) side of the box.
9. Cut one corner of the membrane so that you remember which side of the membrane is in contact with the gel. (maybe not necessary)
10. Close and clamp cassette.
11. Place the holder into the trans-blot.
12. Put box in green tub on stir plate with magnetic stirrer set at a 9, add transblot, and BioIce (in freezer). Add stir bar.
13. Fill box to the top with transfer buffer.

14. Add ice to the bin to surround the box. This is to keep the transfer cold. Halfway through transfer, add more ice and switch out ice block.
15. Set transfer based on the size of the proteins of interest.
    a. For small proteins <25kDa, use 75V for 10-20 min
16. After transfer is complete, remove the membrane, and let air dry for 30 second. Can also dip after in methanol to help better bind the small proteins to the PVDF.

Probe with Antibodies

17. While transferring, make 5% milk (2.5g non-fat milk with 50ml TBST) in 50mL conical tube. Add stir bar to flask and stir to mix.
18. Add 5% milk, rock at RT for 1 hour (this can be extended if there is a lot of background).
19. Place the membrane in 5% milk and add the primary antibody (usually about 10mL milk needed) at the proper dilution. Cut membrane in half if needed.
20. Incubate overnight in the cold room using gentle tilting.

DAY 3

21. Pour the primary antibody solution into 15 mL conical tubes to keep and re-use. Can re-use until milk goes bad.
22. Rinse once quickly, then 3X for 10 minutes each in TBST using gentle tilting.
23. Add secondary antibody to the membrane in 5% nonfat dry milk (Try 1:10k-20k dilution).
    a. 20 mL milk + 1 uL anti-mouse secondary + 1 uL anti-rabbit secondary
24. Incubate for 45 minutes at RT using gentle tilting.
25. Rinse 3X, 10 minutes each in TBST using gentle tilting.
26. Make sure the membrane is identifiable with a cut in the corner and take note of which has been probed with which antibody.

Expose Membrane

1. In foil-wrapped 15mL conical tube, mix together 1 mL of SuperSignal West Pico Stable Peroxide Solution and 1 mL of SuperSignal West Pico Luminal/Enhancer Solution (1:1 ratio) (ECL Solution).
    a. Use a new tip for each solution! Do not allow to mix in the bottles!

2. Lay the membrane on Plastic Wrap and put ECL solution on the membrane (~1mL/membrane).
3. Image using the BioRad imaging station upstairs. Try multiple exposures.

Strip Membrane (Only necessary if reprobing)

1. Submerge membrane in RESTORE Stripping Solution (Pierce) and incubate at RT for 15 minutes with occasional agitation.
2. Wash with TBST 3X for 5 minutes each. Repeat steps 1 and 2 of this section.
3. Re-block in 5% milk for 1 hour at RT, then can probe for a different primary antibody.

References

1. Kellerer AM, Nekolla E. Consideration on a limit for lifetime occupational radiation exposure. *Radiat Environ Biophys*. 1998;37(2):81-85. doi:10.1007/s004110050098

2. Schauer DA, Linton OW. National Council on Radiation Protection and Measurements Report Shows Substantial Medical Exposure Increase. *Radiology*. 2009;253(2):293-296. doi:10.1148/radiol.2532090494

3. Alpert JS. Are You Planning to Sign Up for a Trip to Mars? Extreme Environmental Health Consequences of Space Travel. *Am J Med*. 2018;131(2):115-116. doi:10.1016/j.amjmed.2017.10.004

4. Shimura N, Kojima S. The Lowest Radiation Dose Having Molecular Changes in the Living Body. *Dose Response*. 2018;16(2):1559325818777326. doi:10.1177/1559325818777326

5. Linear Energy Transfer - an overview | ScienceDirect Topics. https://www.sciencedirect.com/topics/chemistry/linear-energy-transfer. Accessed May 11, 2020.

6. Kim EH, Kim MS, Lee KH, et al. Effect of low- A nd high-linear energy transfer radiation on in vitro and orthotopic in vivo models of osteosarcoma by activation of caspase-3 and-9. *Int J Oncol*. 2017;51(4):1124-1134. doi:10.3892/ijo.2017.4102

7. Heselich A, Frieß JL, Ritter S, Benz NP, Layer PG, Thielemann C. High LET radiation shows no major cellular and functional effects on primary cardiomyocytes in vitro. *Life Sci Sp Res*. 2018;16:93-100. doi:10.1016/j.lssr.2018.01.001

8. Templin T, Sharma P, Guida P, Grabham P. Short-Term Effects of Low-LET Radiation on the Endothelial Barrier: Uncoupling of PECAM-1 and the Production of Endothelial Microparticles. *Radiat Res*. 2016;186(6):602. doi:10.1667/rr14510.1

9. Borg AN, Ray SG. A unifying framework for understanding heart failure? Response to "Left Ventricular Torsion By Two-Dimensional Speckle Tracking Echocardiography in Patients With Diastolic Dysfunction and Normal Ejection Fraction" by Park SJ et al. *J Am Soc Echocardiogr*. 2009;22(3):312-318.

doi:10.1016/j.echo.2008.11.026

10. Niemantsverdriet M, Van Goethem MJ, Bron R, et al. High and low LET radiation differentially induce normal tissue damage signals. *Int J Radiat Oncol Biol Phys*. 2012;83(4):1291-1297. doi:10.1016/j.ijrobp.2011.09.057

11. Takahashi A, Ikeda H, Yoshida Y. Role of high-linear energy transfer radiobiology in space radiation exposure risks. *Int J Part Ther*. 2019;5(1):151-159. doi:10.14338/IJPT-18-00013.1

12. Norbury JW, Schimmerling W, Slaba TC, et al. Galactic cosmic ray simulation at the NASA Space Radiation Laboratory. *Life Sci Sp Res*. 2016;8:38-51. doi:10.1016/j.lssr.2016.02.001

13. Simpson JA. Elemental and Isotopic Composition of the Galactic Cosmic Rays. *Annu Rev Nucl Part Sci*. 1983;33(1):323-382. doi:10.1146/annurev.ns.33.120183.001543

14. Ahn HS, Allison P, Bagliesi MG, et al. *Energy Spectra of Cosmic-Ray Nuclei at High Energies*.

15. Yan X, Sasi SP, Gee H, et al. Radiation-associated cardiovascular risks for future deep-space missions. *J Radiat Res*. 2014;55(suppl 1):i37-i39. doi:10.1093/jrr/rrt202

16. Hughson RL, Helm A, Durante M. Heart in space: Effect of the extraterrestrial environment on the cardiovascular system. *Nat Rev Cardiol*. 2018;15(3):167-180. doi:10.1038/nrcardio.2017.157

17. Bukowska B, Karwowski BT. The Clustered DNA Lesions - Types, Pathways of Repair and Relevance to Human Health. *Curr Med Chem*. 2018;25(23):2722-2735. doi:10.2174/0929867325666180226110502

18. Lomax ME, Folkes LK, O'Neill P. Biological consequences of radiation-induced DNA damage: Relevance to radiotherapy. *Clin Oncol*. 2013;25(10):578-585. doi:10.1016/j.clon.2013.06.007

19. Goodhead DT. Initial events in the cellular effects of ionizing radiations: Clustered damage in DNA. *Int J Radiat Biol*. 1994;65(1):7-17. doi:10.1080/09553009414550021

20. Magnander K, Elmroth K. Biological consequences of formation and repair of complex DNA damage. *Cancer Lett*. 2012;327(1-2):90-96. doi:10.1016/j.canlet.2012.02.013

21. Rothkamm K, Löbrich M. Evidence for a lack of DNA double-strand break repair in human cells exposed to very low x-ray doses. *Proc Natl Acad Sci U S A*. 2003;100(9):5057-5062. doi:10.1073/pnas.0830918100

22. Claesson K, Magnander K, Kahu H, Lindegren S, Hultborn R, Elmroth K. RBE of α-particles from 211At for complex DNA damage and cell survival in relation to cell cycle position. *Int J Radiat Biol*. 2011;87(4):372-384. doi:10.3109/09553002.2011.538127

23. Zhou BBS, Elledge SJ. The DNA damage response: Putting checkpoints in perspective. *Nature*. 2000;408(6811):433-439. doi:10.1038/35044005

24. Tavana O, Benjamin CL, Puebla-Osorio N, et al. Cell Cycle Absence of p53-dependent apoptosis leads to UV radiation hypersensitivity, enhanced immunosuppression and cellular senescence View supplementary material. *Cell Cycle*. 2010;9:3328-3336. doi:10.4161/cc.9.16.12688

25. Schmid TE, Dollinger G, Beisker W, et al. Differences in the kinetics of γ-H2AX fluorescence decay after exposure to low and high LET radiation. *Int J Radiat Biol*. 2010;86(8):682-691. doi:10.3109/09553001003734543

26. dynamics of Ku70/80 and DNA-PKcs at DSBs induced by ionizing radiation is dependent on the complexity of damage | Nucleic Acids Research | Oxford Academic. https://academic.oup.com/nar/article/40/21/10821/2411928. Accessed May 12, 2020.

27. Yano KI, Morotomi-Yano K, Wang SY, et al. Ku recruits XLF to DNA double-strand breaks. *EMBO Rep*. 2008;9(1):91-96. doi:10.1038/sj.embor.7401137

28. Mari PO, Florea BI, Persengiev SP, et al. Dynamic assembly of end-joining complexes requires interaction between Ku70/80 and XRCC4. *Proc Natl Acad Sci U S A*. 2006;103(49):18597-18602. doi:10.1073/pnas.0609061103

29. Drouet J, Frit P, Delteil C, De Villartay JP, Salles B, Calsou P. Interplay between Ku, artemis, and the DNA-dependent protein kinase catalytic subunit at DNA ends. *J Biol Chem*. 2006;281(38):27784-27793. doi:10.1074/jbc.M603047200

30. Anderson JA, Harper J V., Cucinotta FA, O'Neill P. Participation of DNA-PKcs in DSB Repair after Exposure to High- and Low-LET Radiation. *Radiat Res*. 2010;174(2):195-205. doi:10.1667/rr2071.1

31. Hara MR, Kovacs JJ, Whalen EJ, et al. A stress response pathway regulates DNA damage through b 2-adrenoreceptors and b-arrestin-1. 2011. doi:10.1038/nature10368

32. Riballo E, Kühne M, Rief N, et al. A pathway of double-strand break rejoining dependent upon ATM, Artemis, and proteins locating to γ-H2AX foci. *Mol Cell*. 2004;16(5):715-724. doi:10.1016/j.molcel.2004.10.029

33. Horn S, Barnard S, Rothkamm K. Gamma-H2AX-based dose estimation for whole and partial body radiation exposure. *PLoS One*. 2011;6(9). doi:10.1371/journal.pone.0025113

34. Chen BPC, Uematsu N, Kobayashi J, et al. Ataxia telangiectasia mutated (ATM) is essential for DNA-PKcs phosphorylations at the Thr-2609 cluster upon DNA double strand break. *J Biol Chem*. 2007;282(9):6582-6587. doi:10.1074/jbc.M611605200

35. Kastan MB, Lim DS. The many substrates and functions of ATM. *Nat Rev Mol Cell Biol*. 2000;1(3):179-186. doi:10.1038/35043058

36. McLarty AJ, Bishawi M, Yelika SB, Shroyer AL, Romeiser J. Surveillance of moderate-size aneurysms of the thoracic aorta. *J Cardiothorac Surg*. 2015;10(1). doi:10.1186/s13019-015-0220-2

37. Tukenova M, Guibout C, Oberlin O, et al. Role of cancer treatment in long-term overall and cardiovascular mortality after childhood cancer. *J Clin Oncol*. 2010;28(8):1308-1315. doi:10.1200/JCO.2008.20.2267

38. Bouillon K, Haddy N, Delaloge S, et al. Long-term cardiovascular mortality after radiotherapy for breast cancer. *J Am Coll Cardiol*. 2011;57(4):445-452. doi:10.1016/j.jacc.2010.08.638

39. Sardar P, Kundu A, Chatterjee S, et al. Long-term cardiovascular mortality after radiotherapy for breast cancer: A systematic review and meta-analysis. *Clin Cardiol*. 2017;40(2):73-81. doi:10.1002/clc.22631

40. Adams H, Martin W, Wilson A, Palmer S. Radiation Therapy Induced Cardiovascular Disease. *Hear Vessel Transplant*. 2017;0(Ahead of Print). doi:10.24969/hvt.2017.25

41. Martinez BK, White CM. The Emerging Role of Inflammation in Cardiovascular Disease. *Ann Pharmacother*. 2018;52(8):801-809. doi:10.1177/1060028018765939

42. Grivennikov SI, Greten FR, Karin M. Immunity, Inflammation, and Cancer. *Cell*. 2010;140(6):883. doi:10.1016/J.CELL.2010.01.025

43. Lopez-Candales A, Hernández Burgos PM, Hernandez-Suarez DF, Harris D. Linking Chronic Inflammation with Cardiovascular Disease: From Normal Aging to the Metabolic Syndrome. *J Nat Sci*. 2017;3(4). http://www.ncbi.nlm.nih.gov/pubmed/28670620. Accessed May 19, 2020.

44. Delp MD, Charvat JM, Limoli CL, Globus RK, Ghosh P. Apollo lunar astronauts show higher cardiovascular disease mortality: Possible deep space radiation effects on the vascular endothelium. *Sci Rep*. 2016;6. doi:10.1038/srep29901

45. Chancellor JC, Blue RS, Cengel KA, et al. *Limitations in Predicting the Space Radiation Health Risk for Exploration Astronauts*.

46. Elgart SR, Little MP, Chappell LJ, et al. Radiation Exposure and Mortality from Cardiovascular Disease and Cancer in Early NASA Astronauts. *Sci Rep*. 2018;8(1):8480. doi:10.1038/s41598-018-25467-9

47. Seawright JW, Sridharan V, Landes RD, et al. Effects of low-dose oxygen ions and protons on cardiac function and structure in male C57BL/6J mice. *Life Sci Sp Res*. 2019;20:72-84. doi:10.1016/j.lssr.2019.01.003

48. He J, Liu X, Su C, et al. Inhibition of Mitochondrial Oxidative Damage Improves Reendothelialization Capacity of Endothelial Progenitor Cells via SIRT3 (Sirtuin 3)-Enhanced SOD2 (Superoxide Dismutase 2) Deacetylation in Hypertension. *Arterioscler Thromb Vasc Biol*. 2019;39(8):1682-1698. doi:10.1161/ATVBAHA.119.312613

49. Shimura T, Kobayashi J, Komatsu K, Kunugita N. Severe mitochondrial damage associated with low-dose radiation sensitivity in ATM- and NBS1-deficient cells. *Cell Cycle*. 2016;15(8):1099-1107. doi:10.1080/15384101.2016.1156276

50. López-Acosta O, de Los Angeles Fortis-Barrera M, Barrios-Maya MA, Ramírez AR, Aguilar FJA, El-Hafidi M. Reactive Oxygen Species from NADPH Oxidase and Mitochondria Participate in the Proliferation of Aortic Smooth Muscle Cells from a Model of Metabolic Syndrome. *Oxid Med Cell Longev*. 2018;2018:5835072. doi:10.1155/2018/5835072

51. Puhm F, Afonyushkin T, Resch U, et al. Mitochondria Are a Subset of Extracellular Vesicles Released by Activated Monocytes and Induce Type I IFN and TNF Responses in Endothelial Cells. *Circ Res*. 2019. doi:10.1161/circresaha.118.314601

52. Shimi T, Goldman RD. Nuclear lamins and oxidative stress in cell proliferation and longevity. *Adv Exp Med Biol*. 2014;773:415-430. doi:10.1007/978-1-4899-8032-8_19

53. Guachalla LM, Rudolph KL. ROS induced DNA damage and checkpoint responses: Influences on aging? *Cell Cycle*. 2010;9(20):4058-4060. doi:10.4161/cc.9.20.13577

54. Hatoum OA, Otterson MF, Kopelman D, et al. Radiation Induces Endothelial Dysfunction in Murine Intestinal Arterioles via Enhanced Production of Reactive Oxygen Species. 2006. doi:10.1161/01.ATV.0000198399.40584.8c

55. Kawamura K, Qi F, Kobayashi J. Potential relationship between the biological effects of low-dose irradiation and mitochondrial ROS production. *J Radiat Res*. 2018;59:ii91-ii97. doi:10.1093/jrr/rrx091

56. Yu H, Yamashita S. Radical scavenging and chemical repair of rutin observed by pulse radiolysis: as a basis for radiation protection. *Free Radic Res*. 2019;53(9-10):1005-1013. doi:10.1080/10715762.2019.1667991

57. Chaurasia M, Bhatt AN, Das A, Dwarakanath BS, Sharma K. Radiation-induced autophagy: Mechanisms and consequences. *Free Radic Res*. 2016;50(3):273-290. doi:10.3109/10715762.2015.1129534

58. Shimura T, Sasatani M, Kawai H, et al. ATM-mediated mitochondrial damage response triggered by nuclear DNA damage in normal human lung fibroblasts. *Cell Cycle*. 2017;16(24):2345-2354. doi:10.1080/15384101.2017.1387697

59. Yamamori T, Yasui H, Yamazumi M, et al. Ionizing radiation induces mitochondrial reactive oxygen species production accompanied by upregulation of mitochondrial electron transport chain function and mitochondrial content under control of the cell cycle checkpoint. *Free Radic Biol Med*. 2012;53(2):260-270. doi:10.1016/j.freeradbiomed.2012.04.033

60. Murphy MP. How mitochondria produce reactive oxygen species. *Biochem J*. 2009;417(1):1-13. doi:10.1042/BJ20081386

61. Zorov DB, Juhaszova M, Sollott SJ. Mitochondrial reactive oxygen species (ROS) and ROS-induced ROS release. *Physiol Rev*. 2014;94(3):909-950. doi:10.1152/physrev.00026.2013

62. Kobashigawa S, Kashino G, Suzuki K, Yamashita S, Mori H. Ionizing Radiation-Induced Cell Death Is Partly Caused by Increase of Mitochondrial Reactive Oxygen Species in Normal Human Fibroblast Cells. *Radiat Res*. 2015;183(4):455. doi:10.1667/rr13772.1

63. Zorov DB, Filburn CR, Klotz LO, Zweier JL, Sollott SJ. Reactive oxygen species (ROS)-induced ROS release: A new phenomenon accompanying induction of the mitochondrial permeability transition in cardiac myocytes. *J Exp Med*. 2000;192(7):1001-1014. doi:10.1084/jem.192.7.1001

64. Kim, Lee, Seo, et al. Cellular Stress Responses in Radiotherapy. *Cells*. 2019;8(9):1105. doi:10.3390/cells8091105

65. Yu TW, Anderson D. Reactive oxygen species-induced DNA damage and its modification: A chemical investigation. *Mutat Res - Fundam Mol Mech Mutagen*. 1997;379(2):201-210. doi:10.1016/S0027-5107(97)00141-3

66. Bertram C, Hass R. Cellular responses to reactive oxygen species-induced DNA damage and aging. *Biol Chem*. 2008;389(3):211-220. doi:10.1515/BC.2008.031

67. Lee J, Kim Y, Lim S, Jo K. Single-molecule visualization of ROS-induced DNA damage in large DNA molecules. *Analyst*. 2016;141(3):847-852. doi:10.1039/c5an01875g

68. Kaarniranta K, Pawlowska E, Szczepanska J, Jablkowska A, Blasiak J. Role of mitochondrial dna damage in ros-mediated pathogenesis of age-related macular degeneration (Amd). *Int J Mol Sci*. 2019;20(10):2374. doi:10.3390/ijms20102374

69. Palmer JC, Tayler HM, Love S. Endothelin-Converting Enzyme-1 Activity, Endothelin-1 Production, and Free Radical-Dependent Vasoconstriction in Alzheimer's Disease. *J Alzheimer's Dis*. 2013;36(3):577-587. doi:10.3233/JAD-130383

70. Raghunathan D, Khilji MI, Hassan SA, Yusuf SW. Radiation-Induced Cardiovascular Disease. *Curr Atheroscler Rep*. 2017;19(5):1-8. doi:10.1007/s11883-017-0658-x

71. Dikalova AE, Itani HA, Nazarewicz RR, et al. Sirt3 Impairment and SOD2 Hyperacetylation in Vascular Oxidative Stress and Hypertension. *Circ Res*. 2017;121(5):564-574. doi:10.1161/CIRCRESAHA.117.310933

72. Miura S, Saitoh S-I, Kokubun T, et al. Mitochondrial-Targeted Antioxidant Maintains Blood Flow, Mitochondrial Function, and Redox Balance in Old Mice Following Prolonged Limb Ischemia. *Int J Mol Sci*. 2017;18(9). doi:10.3390/ijms18091897

73. Paravicini TM, Touyz RM. NADPH Oxidases, Reactive Oxygen Species, and Hypertension. *Diabetes Care*. 2008;31(Suppl 2):S170-S180. doi:10.2337/dc08-s247

74. Paris F, Fuks Z, Kang A, et al. Endothelial apoptosis as the primary lesion initiating intestinal radiation damage in mice. *Science (80-)*. 2001. doi:10.1126/science.1060191

75. Lafargue A, Degorre C, Corre I, et al. Ionizing radiation induces long-term senescence in endothelial cells through mitochondrial respiratory complex II dysfunction and superoxide generation. *Free Radic Biol Med*. 2017;108:750-759. doi:10.1016/j.freeradbiomed.2017.04.019

76. Baeyens N, Bandyopadhyay C, Coon BG, Yun S, Schwartz MA. Endothelial fluid shear stress sensing in vascular health and disease. *J Clin Invest*. 2016;126(3):821-828. doi:10.1172/JCI83083

77. Himburg HA, Sasine J, Yan X, Kan J, Dressman H, Chute JP. A Molecular Profile of the Endothelial Cell Response to Ionizing Radiation. *Radiat Res*. 2016;186(2):141. doi:10.1667/rr14444.1

78. Incalza MA, D'Oria R, Natalicchio A, Perrini S, Laviola L, Giorgino F. Oxidative stress and reactive oxygen species in endothelial dysfunction associated with

cardiovascular and metabolic diseases. *Vascul Pharmacol*. 2018;100:1-19. doi:10.1016/j.vph.2017.05.005

79. Lu X, Guo X, Wassall CD, Kemple MD, Unthank JL, Kassab GS. Reactive oxygen species cause endothelial dysfunction in chronic flow overload. *J Appl Physiol*. 2011;110(2):520-527. doi:10.1152/japplphysiol.00786.2009

80. Schulz E, Gori T, Münzel T. Oxidative stress and endothelial dysfunction in hypertension. *Hypertens Res*. 2011;34(6):665-673. doi:10.1038/hr.2011.39

81. Cho Y-E, Basu A, Dai A, Heldak M, Makino A. Coronary endothelial dysfunction and mitochondrial reactive oxygen species in type 2 diabetic mice. *Am J Physiol Physiol*. 2013;305(10):C1033-C1040. doi:10.1152/ajpcell.00234.2013

82. Venkatesulu BP, Mahadevan LS, Aliru ML, et al. Radiation-Induced Endothelial Vascular Injury: A Review of Possible Mechanisms. *JACC Basic to Transl Sci*. 2018;3(4):563-572. doi:10.1016/j.jacbts.2018.01.014

83. Soloviev AI, Tishkin SM, Parshikov A V, Ivanova I V, Goncharov E V, Gurney AM. Mechanisms of endothelial dysfunction after ionized radiation: selective impairment of the nitric oxide component of endothelium-dependent vasodilation. *Br J Pharmacol*. 2003;138(5):837-844. doi:10.1038/sj.bjp.0705079

84. Yamamori T, Yasui H, Yamazumi M, et al. Ionizing radiation induces mitochondrial reactive oxygen species production accompanied by upregulation of mitochondrial electron transport chain function and mitochondrial content under control of the cell cycle checkpoint. *Free Radic Biol Med*. 2012;53(2):260-270. doi:10.1016/j.freeradbiomed.2012.04.033

85. Wang Y, Boerma M, Zhou D. Ionizing Radiation-Induced Endothelial Cell Senescence and Cardiovascular Diseases. *Radiat Res*. 2016;186(2):153-161. doi:10.1667/rr14445.1

86. Gao S, Ho D, Vatner DE, Vatner SF. Echocardiography in Mice. *Curr Protoc Mouse Biol*. 2011;1:71-83. doi:10.1002/9780470942390.mo100130

87. Sasi SP, Yan X, Zuriaga-Herrero M, et al. Different Sequences of Fractionated Low-Dose Proton and Single Iron-Radiation-Induced Divergent Biological Responses in the Heart. *Radiat Res*. 2017;188(2):191-203. doi:10.1667/RR14667.1

88. Hoit BD. Echocardiographic Assessment of the Mouse Heart and Aorta. In: ; 2001:177-190. doi:10.1007/978-1-4615-1653-8_12

89. Vatner SF, Braunwald E. Cardiovascular control mechanisms in the conscious state. *N Engl J Med*. 1975;293(19):970-976. doi:10.1056/NEJM197511062931906

90. Hughson RL, Helm A, Durante M. Heart in space: effect of the extraterrestrial environment on the cardiovascular system. *Nat Rev Cardiol*. 2018;15(3):167-180. doi:10.1038/nrcardio.2017.157

91. Garrett-Bakelman FE, Darshi M, Green SJ, et al. The NASA twins study: A multidimensional analysis of a year-long human spaceflight. *Science (80-)*. 2019;364(6436). doi:10.1126/science.aau8650

92. Abraham DM, Lee TE, Watson LJ, et al. The two-pore domain potassium channel TREK-1 mediates cardiac fibrosis and diastolic dysfunction. *J Clin Invest*. 2018;128(11):4843-4855. doi:10.1172/JCI95945

93. Abraham DM, Davis RT, Warren CM, et al. β-Arrestin mediates the Frank–Starling mechanism of cardiac contractility. *Proc Natl Acad Sci*. 2016;113(50):14426-14431. doi:10.1073/PNAS.1609308113

94. Yoo BS, Lemaire A, Mangmool S, et al. β1-Adrenergic receptors stimulate cardiac contractility and CaMKII activation in vivo and enhance cardiac dysfunction following myocardial infarction. *Am J Physiol - Hear Circ Physiol*. 2009;297(4). doi:10.1152/ajpheart.00504.2009

95. Abraham D, Mao L. Cardiac pressure-volume loop analysis using conductance catheters in mice. *J Vis Exp*. 2015;2015(103). doi:10.3791/52942

96. Azizova T, Briks K, Bannikova M, Grigoryeva E. Hypertension Incidence Risk in a Cohort of Russian Workers Exposed to Radiation at the Mayak Production Association Over Prolonged Periods. *Hypertens (Dallas, Tex 1979)*. 2019;73(6):1174-1184. doi:10.1161/HYPERTENSIONAHA.118.11719

97. Gardner BI, Bingham SE, Allen MR, Blatter DD, Anderson JL. Cardiac magnetic resonance versus transthoracic echocardiography for the assessment of cardiac volumes and regional function after myocardial infarction: An intrasubject comparison using simultaneous intrasubject recordings. *Cardiovasc Ultrasound*. 2009;7(1):38. doi:10.1186/1476-7120-7-38

98. Matthiä D, Hassler DM, de Wet W, et al. The radiation environment on the surface of Mars - Summary of model calculations and comparison to RAD data. *Life Sci Sp Res*. 2017;14:18-28. doi:10.1016/j.lssr.2017.06.003

99. Gujral DM, Shah BN, Chahal NS, et al. Arterial Stiffness as a Biomarker of Radiation-Induced Carotid Atherosclerosis. *Angiology*. 2016;67(3):266-271. doi:10.1177/0003319715589520

100. Yanagisawa H, Wagenseil J. Elastic fibers and biomechanics of the aorta: Insights from mouse studies. *Matrix Biol*. 2019. doi:10.1016/j.matbio.2019.03.001

101. Fhayli W, Boëté Q, Kihal N, et al. Dill extract induces elastic fiber neosynthesis and functional improvement in the ascending aorta of aged mice with reversal of age-dependent cardiac hypertrophy and involvement of lysyl oxidase-like-1. *Biomolecules*. 2020;10(2). doi:10.3390/biom10020173

102. Belz GG. Elastic properties and Windkessel function of the human aorta. *Cardiovasc Drugs Ther*. 1995;9(1):73-83. doi:10.1007/BF00877747

103. Torres ERS, Hall R, Bobe G, et al. Integrated Metabolomics-DNA Methylation Analysis Reveals Significant Long-Term Tissue-Dependent Directional Alterations in Aminoacyl-tRNA Biosynthesis in the Left Ventricle of the Heart and Hippocampus Following Proton Irradiation. *Front Mol Biosci*. 2019;6. doi:10.3389/fmolb.2019.00077

104. Mettler FA, Bhargavan M, Faulkner K, et al. Radiologic and nuclear medicine studies in the United States and worldwide: Frequency, radiation dose, and comparison with other radiation sources - 1950-2007. *Radiology*. 2009;253(2):520-531. doi:10.1148/radiol.2532082010

105. Tjessem KH, Johansen S, Malinen E, et al. Long-term cardiac mortality after hypofractionated radiation therapy in breast cancer. *Int J Radiat Oncol Biol Phys*. 2013;87(2):337-343. doi:10.1016/j.ijrobp.2013.05.038

106. Cuzick J, Stewart H, Peto R, et al. Overview of randomized trials of postoperative adjuvant radiotherapy in breast cancer. *Cancer Treat Rep*. 1987;71(1):15-29. doi:10.1007/978-3-642-83419-6_15

107. Schaue D, Micewicz ED, Ratikan JA, Xie MW, Cheng G, McBride WH. Radiation

and Inflammation. *Semin Radiat Oncol*. 2015;25(1):4-10. doi:10.1016/j.semradonc.2014.07.007

108. Puukila S, Lemon JA, Lees SJ, Tai TC, Boreham DR, Khaper N. Impact of Ionizing Radiation on the Cardiovascular System: A Review. *Radiat Res*. 2017;188(4.2):539-546. doi:10.1667/rr14864.1

109. Bakshi M V., Barjaktarovic Z, Azimzadeh O, et al. Long-term effects of acute low-dose ionizing radiation on the neonatal mouse heart: A proteomic study. *Radiat Environ Biophys*. 2013;52(4):451-461. doi:10.1007/s00411-013-0483-8

110. Feger BJ, Thompson JW, Dubois LG, et al. Microgravity induces proteomics changes involved in endoplasmic reticulum stress and mitochondrial protection. *Sci Rep*. 2016;6. doi:10.1038/srep34091

111. Jackman CP, Ganapathi AM, Asfour H, et al. Engineered cardiac tissue patch maintains structural and electrical properties after epicardial implantation. *Biomaterials*. 2018;159:48-58. doi:10.1016/j.biomaterials.2018.01.002

112. Bian W, Jackman CP, Bursac N. Controlling the structural and functional anisotropy of engineered cardiac tissues. *Biofabrication*. 2014;6(2):024109-24109. doi:10.1088/1758-5082/6/2/024109

113. Hinds S, Bian W, Dennis RG, Bursac N. The role of extracellular matrix composition in structure and function of bioengineered skeletal muscle. *Biomaterials*. 2011;32(14):3575-3583. doi:10.1016/j.biomaterials.2011.01.062

114. Shadrin IY, Allen BW, Qian Y, et al. Cardiopatch platform enables maturation and scale-up of human pluripotent stem cell-derived engineered heart tissues. *Nat Commun*. 2017;8(1):1825. doi:10.1038/s41467-017-01946-x

115. Jackman CP, Carlson AL, Bursac N. Dynamic culture yields engineered myocardium with near-adult functional output. *Biomaterials*. 2016;111:66-79. doi:10.1016/j.biomaterials.2016.09.024

116. Bian W, Juhas M, Pfeiler TW, Bursac N. Local tissue geometry determines contractile force generation of engineered muscle networks. *Tissue Eng - Part A*. 2012;18(9-10):957-967. doi:10.1089/ten.tea.2011.0313

117. Liang X, Gu J, Yu D, et al. Low-dose radiation induces cell proliferation in human

embryonic lung fibroblasts but not in lung cancer cells: Importance of ERK1/2 and AKT signaling pathways. *Dose-Response*. 2016;14(1):1-10. doi:10.1177/1559325815622174

118. Maes E, Valkenborg D, Baggerman G, et al. Determination of variation parameters as a crucial step in designing TMT-based clinical proteomics experiments. *PLoS One*. 2015;10(3). doi:10.1371/journal.pone.0120115

119. Supek F, Bošnjak M, Škunca N, Šmuc T. REVIGO Summarizes and Visualizes Long Lists of Gene Ontology Terms. Gibas C, ed. *PLoS One*. 2011;6(7):e21800. doi:10.1371/journal.pone.0021800

120. Ashburner M, Ball CA, Blake JA, et al. Gene ontology: Tool for the unification of biology. *Nat Genet*. 2000;25(1):25-29. doi:10.1038/75556

121. Hu W, Zhang P, Gu J, Yu Q, Zhang D. NEDD4-1 protects against ischaemia/reperfusion-induced cardiomyocyte apoptosis via the PI3K/Akt pathway. *Apoptosis*. 2017;22(3):437-448. doi:10.1007/s10495-016-1326-2

122. Luo L, Ning F, Du Y, et al. Calcium-dependent Nedd4-2 upregulation mediates degradation of the cardiac sodium channel Nav1.5: implications for heart failure. *Acta Physiol*. 2017;221(1):44-58. doi:10.1111/apha.12872

123. Slater JP, Rose EA, Levin HR, et al. Low thromboembolic risk without anticoagulation using advanced-design left ventricular assist devices. *Ann Thorac Surg*. 1996;62(5):1321-1327; discussion 1328. doi:10.1016/0003-4975(96)00750-3

124. Abriel H, Kamynina E, Horisberger JD, Staub O. Regulation of the cardiac voltage-gated Na+ channel (H1) by the ubiquitin-protein ligase Nedd4. *FEBS Lett*. 2000;466(2-3):377-380. doi:10.1016/S0014-5793(00)01098-X

125. Fouladkou F, Lu C, Jiang C, et al. The ubiquitin ligase Nedd4-1 is required for heart development and is a suppressor of thrombospondin-1. *J Biol Chem*. 2010;285(9):6770-6780. doi:10.1074/jbc.M109.082347

126. Sevrioukova IF. Apoptosis-inducing factor: Structure, function, and redox regulation. *Antioxidants Redox Signal*. 2011;14(12):2545-2579. doi:10.1089/ars.2010.3445

127. Bano D, Prehn JHM. Apoptosis-Inducing Factor (AIF) in Physiology and Disease:

The Tale of a Repented Natural Born Killer. *EBioMedicine*. 2018;30:29-37. doi:10.1016/j.ebiom.2018.03.016

128. Dikalov SI, Ungvari Z. Role of mitochondrial oxidative stress in hypertension. *Am J Physiol - Hear Circ Physiol*. 2013;305(10). doi:10.1152/ajpheart.00089.2013

129. Vendrov AE, Vendrov KC, Smith A, et al. NOX4 NADPH Oxidase-Dependent Mitochondrial Oxidative Stress in Aging-Associated Cardiovascular Disease. *Antioxid Redox Signal*. 2015;23(18):1389-1409. doi:10.1089/ars.2014.6221

130. McCarthy C, Kenny LC. Therapeutically targeting mitochondrial redox signalling alleviates endothelial dysfunction in preeclampsia. *Sci Rep*. 2016;6(1):1-11. doi:10.1038/srep32683

131. Basic Principles of Radiation Biology - Adverse Reproductive Outcomes in Families of Atomic Veterans: The Feasibility of Epidemiologic Studies - NCBI Bookshelf. https://www.ncbi.nlm.nih.gov/books/NBK232435/. Accessed May 7, 2020.

132. R7.2: Radiosensitivity of Different Cell Populations - OzRadOnc. http://ozradonc.wikidot.com/rb:radiosensitivity-parenchymal. Accessed May 7, 2020.

133. Boerma M, Sridharan V, Mao XW, et al. Effects of ionizing radiation on the heart. *Mutat Res - Rev Mutat Res*. 2016;770(Pt B):319-327. doi:10.1016/j.mrrev.2016.07.003

134. Jackman CP, Ganapathi AM, Asfour H, et al. Engineered cardiac tissue patch maintains structural and electrical properties after epicardial implantation. *Biomaterials*. 2018;159:48-58. doi:10.1016/j.biomaterials.2018.01.002

135. Pomeroy JE, Helfer A, Bursac N. Biomaterializing the promise of cardiac tissue engineering. *Biotechnol Adv*. February 2019. doi:10.1016/j.biotechadv.2019.02.009

136. Zhang D, Shadrin IY, Lam J, Xian H-Q, Snodgrass HR, Bursac N. Tissue-engineered cardiac patch for advanced functional maturation of human ESC-derived cardiomyocytes. *Biomaterials*. 2013;34(23):5813-5820. doi:10.1016/j.biomaterials.2013.04.026

137. Sridharan V, Tripathi P, Sharma SK, et al. Cardiac inflammation after local irradiation is influenced by the kallikrein-kinin system. *Cancer Res*.

2012;72(19):4984-4992. doi:10.1158/0008-5472.CAN-12-1831

138. Li Y, Asfour H, Bursac N. Age-dependent functional crosstalk between cardiac fibroblasts and cardiomyocytes in a 3D engineered cardiac tissue. *Acta Biomater*. 2017;55:120-130. doi:10.1016/j.actbio.2017.04.027

139. Yusuf SW, Venkatesulu BP, Mahadevan LS, Krishnan S. Radiation-Induced Cardiovascular Disease: A Clinical Perspective. *Front Cardiovasc Med*. 2017;4. doi:10.3389/fcvm.2017.00066

140. Owen JB, Allan Butterfiel D. Measurement of oxidized/reduced glutathione ratio. In: *Methods in Molecular Biology*. Vol 648. Humana Press Inc.; 2010:269-277. doi:10.1007/978-1-60761-756-3_18

141. Navarro J, Obrador E, Pellicer JA, Asensi M, Viña J, Estrela JM. Blood glutathione as an index of radiation-induced oxidative stress in mice and humans. *Free Radic Biol Med*. 1997;22(7):1203-1209. doi:10.1016/S0891-5849(96)00554-0

142. Piquereau J, Caffin F, Novotova M, et al. Mitochondrial dynamics in the adult cardiomyocytes: which roles for a highly specialized cell? *Front Physiol*. 2013;4. doi:10.3389/fphys.2013.00102

143. Vendrov AE, Vendrov KC, Smith A, et al. NOX4 NADPH oxidase-dependent mitochondrial oxidative stress in aging-associated cardiovascular disease. *Antioxidants Redox Signal*. 2015;23(18):1389-1409. doi:10.1089/ars.2014.6221

144. Eoh JH, Shen N, Burke JA, et al. Enhanced elastin synthesis and maturation in human vascular smooth muscle tissue derived from induced-pluripotent stem cells. *Acta Biomater*. 2017;52:49-59. doi:10.1016/j.actbio.2017.01.083

145. Haase N, Herse F, Spallek B, et al. Amyloid-β Peptides Activate α_1-Adrenergic Cardiovascular Receptors. *Hypertension*. 2013;62(5):966-972. doi:10.1161/HYPERTENSIONAHA.113.01348

146. Wallace CS, Truskey GA. Direct-contact co-culture between smooth muscle and endothelial cells inhibits TNF-α-mediated endothelial cell activation. *Am J Physiol - Hear Circ Physiol*. 2010;299(2). doi:10.1152/ajpheart.01029.2009

147. Li M, Qian M, Kyler K, Xu J. Endothelial–Vascular Smooth Muscle Cells Interactions in Atherosclerosis. *Front Cardiovasc Med*. 2018;5:151.

doi:10.3389/fcvm.2018.00151

148. Deverse JS, Sandhu AS, Mendoza N, et al. Shear stress modulates VCAM-1 expression in response to TNF-α and dietary lipids via interferon regulatory factor-1 in cultured endothelium. *Am J Physiol - Hear Circ Physiol*. 2013;305(8). doi:10.1152/ajpheart.00311.2013

149. Vascular Endothelium - an overview | ScienceDirect Topics. https://www.sciencedirect.com/topics/agricultural-and-biological-sciences/vascular-endothelium. Accessed May 15, 2020.

150. Rajendran P, Rengarajan T, Thangavel J, et al. The vascular endothelium and human diseases. *Int J Biol Sci*. 2013;9(10):1057-1069. doi:10.7150/ijbs.7502

151. Krüger-Genge A, Blocki A, Franke RP, Jung F. Vascular endothelial cell biology: An update. *Int J Mol Sci*. 2019;20(18). doi:10.3390/ijms20184411

152. Cahill PA, Redmond EM. Vascular endothelium - Gatekeeper of vessel health. *Atherosclerosis*. 2016;248:97-109. doi:10.1016/j.atherosclerosis.2016.03.007

153. Pi X, Xie L, Patterson C. Emerging roles of vascular endothelium in metabolic homeostasis. *Circ Res*. 2018;123(4):477-494. doi:10.1161/CIRCRESAHA.118.313237

154. Epstein FH, Vane JR, Änggård EE, Botting RM. Regulatory functions of the vascular endothelium. *N Engl J Med*. 1990;323(1):27-36. doi:10.1056/NEJM199007053230106

155. Kelleher RJ, Soiza RL. Evidence of endothelial dysfunction in the development of Alzheimer's disease: Is Alzheimer's a vascular disorder? *Am J Cardiovasc Dis*. 2013;3(4):197-226. http://www.ncbi.nlm.nih.gov/pubmed/24224133. Accessed July 25, 2019.

156. Chisari M, Merlo S, Sortino MA, Salomone S. Long-term incubation with β-amyloid peptides impairs endothelium-dependent vasodilatation in isolated rat basilar artery. *Pharmacol Res*. 2010;61(2):157-161. doi:10.1016/j.phrs.2009.09.004

157. Multiple Functions of the Endothelial Cells - The Endothelium - NCBI Bookshelf. https://www.ncbi.nlm.nih.gov/books/NBK57148/. Accessed May 15, 2020.

158. Livingston K, Schlaak RA, Puckett LL, Bergom C. The Role of Mitochondrial

Dysfunction in Radiation-Induced Heart Disease: From Bench to Bedside. *Front Cardiovasc Med*. 2020;7:20. doi:10.3389/fcvm.2020.00020

159. Baselet B, Sonveaux P, Baatout S, Aerts A. Pathological effects of ionizing radiation: endothelial activation and dysfunction. *Cell Mol Life Sci*. 2019;76(4):699-728. doi:10.1007/s00018-018-2956-z

160. Esplugas R, Bellés M, Serra N, et al. Effect of radiation on the expression of CVD-related miRNAs, inflammation and endothelial dysfunction of HUVECs. *Anticancer Res*. 2019;39(2):771-780. doi:10.21873/anticanres.13174

161. Ramadan R, Vromans E, Anang DC, et al. Single and fractionated ionizing radiation induce alterations in endothelial connexin expression and channel function. *Sci Rep*. 2019;9(1). doi:10.1038/s41598-019-39317-9

162. Kang J-H, Woo JK, Jang Y-S, Oh SH. Radiation Potentiates Monocyte Infiltration into Tumors by Ninjurin1 Expression in Endothelial Cells. *Cells*. doi:10.3390/cells9051086

163. Bennett MR, Sinha S, Owens GK. Vascular Smooth Muscle Cells in Atherosclerosis. *Circ Res*. 2016;118(4):692-702. doi:10.1161/CIRCRESAHA.115.306361

164. Preston DL, Shimizu Y, Pierce DA, Suyama A, Mabuchi K. Studies of Mortality of Atomic Bomb Survivors. Report 13: Solid Cancer and Noncancer Disease Mortality: 1950–1997. *Radiat Res*. 2003;160(4):381-407. doi:10.1667/rr3049

165. McGale P, Darby SC. Low Doses of Ionizing Radiation and Circulatory Diseases: A Systematic Review of the Published Epidemiological Evidence. *Radiat Res*. 2005;163(3):247-257. doi:10.1667/rr3314

166. Aird WC. Endothelial cell heterogeneity. *Cold Spring Harb Perspect Med*. 2012;2(1). doi:10.1101/cshperspect.a006429

167. Jamiolkowski RM, Kang S Do, Rodriguez AK, et al. Increased yield of endothelial cells from peripheral blood for cell therapies and tissue engineering. *Regen Med*. 2015;10(4):447-460. doi:10.2217/rme.15.2

168. Fernandez CE, Obi-Onuoha IC, Wallace CS, Satterwhite LL, Truskey GA, Reichert WM. Late-outgrowth endothelial progenitors from patients with coronary artery

disease: Endothelialization of confluent stromal cell layers. *Acta Biomater*. 2014;10(2):893-900. doi:10.1016/j.actbio.2013.10.004

169. Fernandez CE, Achneck HE, Reichert WM, Truskey GA. Biological and engineering design considerations for vascular tissue engineered blood vessels (TEBVs). *Curr Opin Chem Eng*. 2014;3:83-90. doi:10.1016/j.coche.2013.12.001

170. Cheung TM, Ganatra MP, Fu JJ, Truskey GA. The Effect of Stress-Induced Senescence on Aging Human Cord Blood-Derived Endothelial Cells. *Cardiovasc Eng Technol*. 2013;4(2):220-230. doi:10.1007/s13239-013-0128-8

171. Cheung TM, Ganatra MP, Peters EB, Truskey GA. Effect of cellular senescence on the albumin permeability of blood-derived endothelial cells. *Am J Physiol - Hear Circ Physiol*. 2012;303(11). doi:10.1152/ajpheart.00182.2012

172. Bevilacqua, M.D., Ph.D MP, Nelson, Ph.D RM, Mannori, M.D., Ph.D G, Cecconi, M.D O. ENDOTHELIAL-LEUKOCYTE ADHESION MOLECULES IN HUMAN DISEASE. *Annu Rev Med*. 1994;45(1):361-378. doi:10.1146/annurev.med.45.1.361

173. Quarmby S, Kumar P, Kumar S. Radiation-induced normal tissue injury: role of adhesion molecules in leukocyte-endothelial cell interactions. *Int J cancer*. 1999;82(3):385-395. doi:10.1002/(sici)1097-0215(19990730)82:3<385::aid-ijc12>3.0.co;2-5

174. Iwaki T, Urano T, Umemura K. PAI-1, progress in understanding the clinical problem and its aetiology. *Br J Haematol*. 2012;157(3):291-298. doi:10.1111/j.1365-2141.2012.09074.x

175. Vaughan DE. PAI-1 and atherothrombosis. In: *Journal of Thrombosis and Haemostasis*. Vol 3. ; 2005:1879-1883. doi:10.1111/j.1538-7836.2005.01420.x

176. Liu Y, Cheng J, Guo X, et al. The roles of PAI-1 gene polymorphisms in atherosclerotic diseases: A systematic review and meta-analysis involving 149,908 subjects. *Gene*. 2018;673:167-173. doi:10.1016/j.gene.2018.06.040

177. Borges HL, Chao C, Xu Y, Linden R, Wang JYJ. Radiation-induced apoptosis in developing mouse retina exhibits dose-dependent requirement for ATM phosphorylation of p53. *Cell Death Differ*. 2004;11(5):494-502. doi:10.1038/sj.cdd.4401366

178. Zhang XP, Liu F, Cheng Z, Wang W. Cell fate decision mediated by p53 pulses. *Proc Natl Acad Sci U S A*. 2009;106(30):12245-12250. doi:10.1073/pnas.0813088106

179. Demarchi F, Cataldo F, Bertoli C, Schneider C. Cell Cycle DNA damage response links calpain to cellular senescence. 2010. doi:10.4161/cc.9.4.10637

180. Wan Y-Z, Gao P, Zhou S, et al. SIRT1-mediated epigenetic downregulation of plasminogen activator inhibitor-1 prevents vascular endothelial replicative senescence. *Aging Cell*. 2014;13(5):890-899. doi:10.1111/acel.12247

181. Paula Piñera BM, Díaz Valdez YN, Puentes YH, et al. Impact of high blood pressure on atherosclerotic process of coronary arteries: Pathomorphomertry. *Rev Cuba Investig Biomed*. 2009;28(3):37-43.

182. Rossman MJ, Kaplon RE, Hill SD, et al. Endothelial cell senescence with aging in healthy humans: Prevention by habitual exercise and relation to vascular endothelial function. *Am J Physiol - Hear Circ Physiol*. 2017;313(5):H890-H895. doi:10.1152/ajpheart.00416.2017

183. Carracedo J, Ramírez-Carracedo R, Alique M, Ramírez-Chamond R. Endothelial Cell Senescence in the Pathogenesis of Endothelial Dysfunction. In: *Endothelial Dysfunction - Old Concepts and New Challenges*. InTech; 2018. doi:10.5772/intechopen.73024

184. Erusalimsky JD. Vascular endothelial senescence: From mechanisms to pathophysiology. *J Appl Physiol*. 2009;106(1):326-332. doi:10.1152/japplphysiol.91353.2008

185. Samarakoon R, Higgins SP, Higgins CE, Higgins PJ. The TGF-β1/p53/PAI-1 signaling axis in vascular senescence: Role of Caveolin-1. *Biomolecules*. 2019;9(8). doi:10.3390/biom9080341

186. Golding SE, Rosenberg E, Valerie N, et al. Improved ATM kinase inhibitor KU-60019 radiosensitizes glioma cells, compromises insulin, AKT and ERK prosurvival signaling, and inhibits migration and invasion. *Mol Cancer Ther*. 2009;8(10):2894-2902. doi:10.1158/1535-7163.MCT-09-0519

187. Ward IM, Minn K, van Deursen J, Chen J. p53 Binding Protein 53BP1 Is Required for DNA Damage Responses and Tumor Suppression in Mice. *Mol Cell Biol*. 2003;23(7):2556-2563. doi:10.1128/mcb.23.7.2556-2563.2003

188. Horn S, Barnard S, Rothkamm K. Gamma-H2AX-based dose estimation for whole and partial body radiation exposure. *PLoS One*. 2011. doi:10.1371/journal.pone.0025113

189. Hoorelbeke D, Decrock E, De Smet M, et al. Cx43 channels and signaling via IP3/Ca2+, ATP, and ROS/NO propagate radiation-induced DNA damage to non-irradiated brain microvascular endothelial cells. *Cell Death Dis*. 2020;11(3):1-17. doi:10.1038/s41419-020-2392-5

190. Yahyapour R, Shabeeb D, Cheki M, et al. Radiation Protection and Mitigation by Natural Antioxidants and Flavonoids: Implications to Radiotherapy and Radiation Disasters. *Curr Mol Pharmacol*. 2018;11(4):285-304. doi:10.2174/1874467211666180619125653

191. Zaremba-Czogalla M, Hryniewicz-Jankowska A, Tabola R, et al. A novel regulatory function of CDKN1A/p21 in TNFα-induced matrix metalloproteinase 9-dependent migration and invasion of triple-negative breast cancer cells. *Cell Signal*. 2018;47:27-36. doi:10.1016/j.cellsig.2018.03.010

192. Webster M, Wikin KL, Cohen-Fix O. Sizing up the nucleus: Nuclear shape, size and nuclear-envelope assembly. *J Cell Sci*. 2009;122(10):1477-1486. doi:10.1242/jcs.037333

193. Perovanovic J, Dell'Orso S, Gnochi VF, et al. Laminopathies disrupt epigenomic developmental programs and cell fate. *Sci Transl Med*. 2016;8(335):335ra58-335ra58. doi:10.1126/scitranslmed.aad4991

194. Worman HJ, Bonne G. "Laminopathies": A wide spectrum of human diseases. *Exp Cell Res*. 2007;313(10):2121-2133. doi:10.1016/j.yexcr.2007.03.028

195. Chang W, Wang Y, Gant Luxton GW, Östlund C, Worman HJ, Gundersen GG. Imbalanced nucleocytoskeletal connections create common polarity defects in progeria and physiological aging. *Proc Natl Acad Sci U S A*. 2019;116(9):3578-3583. doi:10.1073/pnas.1809683116

196. Atchison L, Zhang H, Cao K, Truskey GA. A Tissue Engineered Blood Vessel Model of Hutchinson-Gilford Progeria Syndrome Using Human iPSC-derived Smooth Muscle Cells. *Sci Rep*. 2017;7(1):8168. doi:10.1038/s41598-017-08632-4

197. Paradisi M, McClintock D, Boguslavsky RL, Pedicelli C, Worman HJ, Djabali K. Dermal fibroblasts in Hutchinson-Gilford progeria syndrome with the lamin A G608G mutation have dysmorphic nuclei and are hypersensitive to heat stress. *BMC Cell Biol*. 2005;6. doi:10.1186/1471-2121-6-27

198. Atchison L, Zhang H, Cao K, Truskey GA. A Tissue Engineered Blood Vessel Model of Hutchinson-Gilford Progeria Syndrome Using Human iPSC-derived Smooth Muscle Cells. *Sci Rep*. 2017;7(1). doi:10.1038/s41598-017-08632-4

199. Capparelli C, Chiavarina B, Whitaker-Menezes D, et al. CDK inhibitors (p16/p19/p21) induce senescence and autophagy in cancer-associated fibroblasts, "fueling" tumor growth via paracrine interactions, without an increase in neo-angiogenesis. *Cell Cycle*. 2012;11(19):3599-3610. doi:10.4161/cc.21884

200. Szekely JG, Copps TP, Morash BD. Radiation-Induced Invagination of the Nuclear Envelope. *Radiat Res*. 1980;83(3):621. doi:10.2307/3575342

201. Stiff T, O'Driscoll M, Rief N, Iwabuchi K, Löbrich M, Jeggo PA. ATM and DNA-PK Function Redundantly to Phosphorylate H2AX after Exposure to Ionizing Radiation. *Cancer Res*. 2004;64(7):2390-2396. doi:10.1158/0008-5472.CAN-03-3207

202. Halim VA, García-Santisteban I, Warmerdam DO, et al. Doxorubicin-induced DNA damage causes extensive ubiquitination of ribosomal proteins associated with a decrease in protein translation. *Mol Cell Proteomics*. 2018;17(12):2297-2308. doi:10.1074/mcp.RA118.000652

203. Yang F, Teves SS, Kemp CJ, Henikoff S. Doxorubicin, DNA torsion, and chromatin dynamics. *Biochim Biophys Acta - Rev Cancer*. 2014;1845(1):84-89. doi:10.1016/j.bbcan.2013.12.002

204. Capolongo L, Belvedere G, D'Incalci M. DNA damage and cytotoxicity of mitoxantrone and doxorubicin in doxorubicin-sensitive and-resistant human colon carcinoma cells. *Cancer Chemother Pharmacol*. 1990;25(6):430-434. doi:10.1007/BF00686054

205. Taymaz-Nikerel H, Karabekmez ME, Eraslan S, Kırdar B. Doxorubicin induces an extensive transcriptional and metabolic rewiring in yeast cells. *Sci Rep*. 2018;8(1):1-14. doi:10.1038/s41598-018-31939-9

206. Asnani A, Zheng B, Liu Y, et al. Highly potent visnagin derivatives inhibit Cyp1

and prevent doxorubicin cardiotoxicity. *JCI insight*. 2018;3(1). doi:10.1172/jci.insight.96753

207. Maillet A, Tan K, Chai X, et al. Modeling Doxorubicin-Induced Cardiotoxicity in Human Pluripotent Stem Cell Derived-Cardiomyocytes. *Sci Rep*. 2016;6(1):1-13. doi:10.1038/srep25333

208. Hsu C-H, Altschuler SJ, Wu LF. Patterns of Early p21 Dynamics Determine Proliferation-Senescence Cell Fate after Chemotherapy. *Cell*. 2019;178(2):361-373.e12. doi:10.1016/j.cell.2019.05.041

209. Shutt TE, McBride HM. Staying cool in difficult times: Mitochondrial dynamics, quality control and the stress response. *Biochim Biophys Acta - Mol Cell Res*. 2013;1833(2):417-424. doi:10.1016/j.bbamcr.2012.05.024

210. Fang EF, Scheibye-Knudsen M, Chua KF, Mattson MP, Croteau DL, Bohr VA. Nuclear DNA damage signalling to mitochondria in ageing. *Nat Rev Mol Cell Biol*. 2016;17(5):308-321. doi:10.1038/nrm.2016.14

211. Schomberg J, Wang Z, Farhat A, et al. Luteolin inhibits melanoma growth in vitro and in vivo via regulating ECM and oncogenic pathways but not ROS. *Biochem Pharmacol*. May 2020:114025. doi:10.1016/j.bcp.2020.114025

212. Gao Y, Wang Y, Liu H, Liu Z, Zhao J. Mitochondrial DNA from hepatocytes induces upregulation of interleukin-33 expression of macrophages in nonalcoholic steatohepatitis. *Dig Liver Dis*. 2020. doi:10.1016/j.dld.2020.03.021

213. Palikaras K, Tavernarakis N. Mitochondrial homeostasis: The interplay between mitophagy and mitochondrial biogenesis. *Exp Gerontol*. 2014;56:182-188. doi:10.1016/j.exger.2014.01.021

214. Noh MR, Kong MJ, Han SJ, Kim JI, Park KM. Isocitrate dehydrogenase 2 deficiency aggravates prolonged high-fat diet intake-induced hypertension. *Redox Biol*. 2020;34. doi:10.1016/j.redox.2020.101548

215. Van Meter M, Simon M, Tombline G, et al. JNK Phosphorylates SIRT6 to Stimulate DNA Double-Strand Break Repair in Response to Oxidative Stress by Recruiting PARP1 to DNA Breaks. *Cell Rep*. 2016;16(10):2641-2650. doi:10.1016/j.celrep.2016.08.006

216. Hanna R, Crowther JM, Bulsara PA, Wang X, Moore DJ, Birch-Machin MA. Optimised detection of mitochondrial DNA strand breaks. *Mitochondrion*. 2019;46:172-178. doi:10.1016/j.mito.2018.04.009

217. Moran CJ, Ramesh A, Brama PAJ, O'Byrne JM, O'Brien FJ, Levingstone TJ. The benefits and limitations of animal models for translational research in cartilage repair. *J Exp Orthop*. 2016;3(1):1-12. doi:10.1186/s40634-015-0037-x

218. Fernandez CE, Yen RW, Perez SM, et al. Human Vascular Microphysiological System for in vitro Drug Screening. *Sci Rep*. 2016;6(1):21579. doi:10.1038/srep21579

219. Chen Z, Tang M, Huang D, et al. Real-time observation of leukocyte-endothelium interactions in tissue-engineered blood vessel. *Lab Chip*. 2018;18(14):2047-2054. doi:10.1039/c8lc00202a

220. Truskey GA. Human Microphysiological Systems and Organoids as in Vitro Models for Toxicological Studies. *Front Public Heal*. 2018;6. doi:10.3389/fpubh.2018.00185

221. Chien S. Effects of disturbed flow on endothelial cells. *Ann Biomed Eng*. 2008;36(4):554-562. doi:10.1007/s10439-007-9426-3

222. Langer HF, Chavakis T. Leukocyte - Endothelial interactions in inflammation. *J Cell Mol Med*. 2009;13(7):1211-1220. doi:10.1111/j.1582-4934.2009.00811.x

Biography

Muath Bishawi completed a BS in Biochemistry and Cell Biology, MPH in Evaluative Sciences, and a Medical Doctorate (MD) all at Stony Brook University, NY. He matriculated at Duke for his cardiothoracic surgical residency in 2014. After completing two clinical years, he took protected time away from the operating room to pursue a PhD in Biomedical Engineering, in Professor Truskey's lab. His long time career goal is to become a surgeon scientist and an innovator with a clinical and research focus on heart disease, and heart failure treatments. During his PhD lab years, Muath was an awardee of the NIH-R38 program through the NHLBI aimed at physician scientist development.